University of Alberta

Physics

Thesis

STM Downmixed Readout of Nanomechanical Motion

by

MENG KAN

Acknowledgment

I would like to express my deepest appreciation to my supervisors Dr. Wayne Hiebert and Professor Mark Freeman who grant me the opportunity and introduce me to the amazing world of NEMS. As mentors, they provided great help, support and enthusiasm which make a pretty educational journey. Their vast knowledge of numerous science disciplines, coupled with an unmatched enthusiasm for nanoelectromechanical system will always be remembered.

Thanks to David C. Fortin and Eric Finley whose help to set up STM system and make the system work. Thanks to all members in Mark group, I very enjoy learning and discussing with them.

Last but not least, I would like to thank my family for their support and encouragement, and am especially grateful to my wife, for always been with me through the ups and downs. My progress would never have been possible with their dedication.

The work was supported by the National Research Council of Canada, iCORE and University of Alberta.

STM Downmixed Readout of Nanomechanical Motion

MENG KAN

University of Alberta, Department of Physics, 2010

Supervisors: Dr. Wayne Hiebert, National Institute for Nanotechnology

Professor Mark Freeman, Department of Physics, University of Alberta

ABSTRACT

For all the nanotechnology applications of NEMS devices, a key challenge is figuring out a fast, low-noise technique for translating small mechanical motion into reasonable electronic signals to measure. The scanning tunneling microscope (STM) based on quantum tunneling between a sharp tip and conducting sample is a promising method to measure the small displacements. For quantum tunneling, the tunneling current is sensitive to the change in distance between the sharp tip and conducting sample, usually less than 1nm. However a limitation in scanning tunneling microscopy is the low temporal resolution because stray capacitance of readout circuitry between the amplifier and tunneling junction will cutoff the high frequency, usually at a few kHz. This limitation is far less than the fundamental limit of STM, $I_T/e \sim$ GHz. In this thesis, an STM-downmixed readout technique, which directly mixes high frequency signals in tunneling junctions, is introduced and explored in order to overcome the bandwidth limitation of STM. With this technology we measure the high frequency vibrational modes (~ 1 MHz) of MEMS doubly-clamped beams, well above the RC rolloff or our circuitry, and explore the impact coming from driving force, measuring position and STM parameters, such as DC tunneling current, DC bias voltage, for sensitivity of STM downmixed readout technique and resonance frequencies of MEMS device. We anticipate that, with this technique, the GHz, - even higher frequency -, information can be detected.

Contents

Chapter 1 Introduction **1**

1.1 Overview of nanoelectromechanical system 1

1.2 Mathematical description of resonator motion 3

1.3 Fabrication of nanoelectromechanical devices 7

1.4 Displacement detection of NEMS 11

1.5 Motivation of this thesis 17

REFERENCES 20

Chapter 2 Experimental Instrument **24**

2.1. Scanning Tunneling Microscopy (STM) system 24

2.2. The adaptations of the STM system 27

2.2.1 Modification of Mechanical Part of STM 27

2.2.2 The Accessories of STM System 31

2.3. The operation of STM 34

REFERENCES 37

Chapter 3 Electron Tunneling Transducer Using Signal Downmixing Readout **38**

3.1 The introduction of electron tunneling transducer 38

3.2 Device actuation 42

3.3 Mathematical description of STM Junction downmixing 45

3.4 Configurations of tunneling junction frequency downmixing 47

REFERENCES 52

Chapter 4 Downmixing Data with STM as Electron Tunneling Transducer

4.1 The MEMS sample setup 53

4.2 The prove of STM tunneling junction downmixing 55

4.3 The result of STM downmixing readout 58

4.4 Impact parameters of results with STM downmixing method 71

4.4.1 Forces between STM tip and MEMS device 71

4.4.2 The effect of change DC tunneling current 74

4.4.3 The effect of change DC bias voltage 77

4.4.4 The effect of change piezo disk actuating power 81

4.4.5 The effect of measured point 87

4.5 The displacement sensitivity of the STM downmixing readout method 91

4.6 Conclusion 94

REFERENCES 95

Chapter 5 Future directions 97

5.1 How to measure the nanoscale device 97

5.2 Phase Locked Loop (PLL) with STM downmixing readout 98

5.3 Integrate the whole system into a chip 99

REFERENCE 101

Appendix A Labview Program Operation 102

Appendix B STM Downmixing Analysis with Normal Mixer 104

APPENDIX C: The Beam Higher Mode Information 107

APPENDIX D: Detail Information about the Different Point 112

List of Figure

Figure 1.1 Doubly-clamped beam with length ℓ, width w and thickness h suspended a distance d above the Si substrate.……...3

Figure 1.2 Schematic drawing illustrating contact exposures.…….9

Figure 1.3 The process steps to fabricate suspended doubly clamped beam with photolithography. (a) SOI wafer. (b) The wafer is coated with metal (Au and Cr). (c) The wafer is coated with metal and photoresist. (d) Metal layer is patterned with photolithography and etched. (e) Alloyed layer and Silicon layer are etched away. (f) Silicon dioxide layer is etched through…….....10

Figure 1.4 Optical displacement detection (a) In Fabry-Perot interferometry, the reflected light from NEMS structure is collimated through the same lens and is directed onto a photodiode. (b) Michelson interferometry, the light from the device interferes with a reference beam created using a beam-splitter and a reference mirror……12

Figure 1.5 Magnetomotive displacement detection…….....13

Figure 1.6 Capacitive displacement detection (a) Diagram of capacitive detection for a doubly clamped NEMS beam (b) The circuit of capacitive detection…….....15

Figure 1.7 Electron tunneling transducer for displacement detection……17

Figure 2.1 Schematic diagram of a scanning tunneling microscope (This graph comes from the Wikimedia Commons)…….....25

Figure 2.2 The schematic of two operation mode in STM (a) Constant-current mode and (b) Constant –height mode……...26

Figure 2.3 The schematic of STM mechanical part and STM sample approaching system (Inset)……...28

Figure 2.4 The schematic of new adjustment stop…….29

Figure 2.5 The image of MEMS device and tip in the mirror ……..29

Figure 2.6 The scheme of sample holder (a) The older sample holder (b) The Schematic of new sample holder and (c) The new sample holder with attocube System which can move along X and Y Plane……..30

Figure 2.7 Pt-Ir STM Tip with 200μm scale bar. (a) Two tips on the top close each other (b) Two tip on the top with big gap…….32

Figure 2.8 The spectrum of noise in STM system (a) The ion pump noise spectrum (b) Other noise spectrum……...34

Figure 2.9 The image of STM system on vibration isolation table……34

Figure 2.10 Basic element of a Scanning Tunneling Microscopy……...35

Figure 3.1 Scheme for the detection of displacement through an electron tunneling transducer. The static separation between the NEMS device and the tip is d and the displacement of the NEMS device is (d-x)…….....39

Figure 3.2 Motion of Piezoelectric Material……..43

Figure 3.3 Piezoelectric Material Frequency Responses……...43

Figure 3.4 Scheme of downmixing which integrates electron tunneling transducer and piezoelectric actuator……...46

Figure 3.5 Information of Tunneling Current in Frequency Domain……47

Figure 3.6 STM frequency downmixing readout scheme……..49

Figure 4.1 Schematic of the doubly-clamped beam……...53

Figure 4.2 The sample of STM downmixing readout. Here MEMS device and the piezo disc which is used to actuating MEMS device are mounted on the PCB together…….54

Figure 4.3 The Downmixing Tunneling Current Information from spectrum analyzer. (a) Frequency far from resonance frequency. (b) (c) and (d) Frequency close to the resonance frequency. ……..56

Figure 4.4 The downmixed tunneling current sideband information. Inset graph (a) Electrical and mechanical noise current FFT (b) Reference frequency with sideband current FFT……...57

Figure 4.5 COMSOL simulation of beam mode shapes (Color indicates displacement from equilibrium position with minimum displacement at the ends of the beam)……59

Figure 4.6 Schematic optical interferometry technique…….60

Figure 4.7 Optical interferometry measured response amplitude (black line) and phase (cyan line) as a function of drive frequency. The red line shows the Lorentz fitting for the amplitude of MEMS device…….61

Figure 4.8 The readout Result of STM downmixing (a) Downmixed tunneling response prediction with simulation (b) The real measure result with phase change from 0 to 180 degree (c) The real measure result with phase change from -90 degree to 90 degree…….65

Figure 4.9 The result of STM downmixed Readout (a) Fundamental flexural mode vibration frequency (b) The first torsion mode vibration frequency (c) The third flexural mode vibration frequency (d) The second torsion mode vibration frequency and (e) The forth flexural mode vibration frequency…….68

Figure 4.10 Comparison of van der Waals force, Electrostatic force and Casimir force …….73

Figure 4.11 The impact of change DC tunneling current (a) The results and fitting of downmixed tunneling current for different DC tunneling current (b) Downmixed tunneling current peak impacted by DC tunneling current (c) Resonance Frequencies impacted by DC tunneling current……..76

Figure 4.12 Effect of DC Bias Voltage in STM Downmixing Method (a)The results and fitting of downmixed tunneling current for different DC bias voltage (b) Downmixed tunneling peaks change with DC bias

voltage (c) Resonance frequencies are modified by DC bias voltage……...80

Figure 4.13 The piezo disk frequency response. Inset graph (a) shows the piezo disk frequency response from 400 KHz to 500 KHz (b) shows the piezo disk frequency response from 500 KHz to 600 KHz and (c) shows the piezo disk frequency response from 900 KHz to 1 MHz ……82

Figure 4.14 The impact of change actuating power. (a) The results and fitting of downmixed tunneling current for different actuating power (b) The solid line show the vibration amplitude for different points of the forth flexural mode and the red dots show the resonance frequency responding point...……...84

Figure 4.15 Resonance frequency change with the actuating power using optical interferometry method (a) The results and fitting of response (b) Resonance frequency are modified by actuating power……..86

Figure 4.16 Effect of Resonance Frequencies for the Measured Point along the length direction of the MEMS Beam. (a) The results and fitting of different measuring points (b) The change of resonance frequencies and vibration amplitude for different points of the forth flexural mode…… ……88

Figure 4.17 Effect of resonance frequency for different measured points along the length direction of the MEMS beam (small resonance frequency shift)…….90

Figure 4.18 Effect of resonance frequency and phase for different points along the width direction of the MEMS beam (a) the resonance frequency and phase information at 1415 of 1700 of the beam (b) the resonance frequency and phase information at the center of the beam…….91

Figure 4.19 The current noise of the STM downmixing method for two different points……93

Figure5.1 The Scheme of Phase-locked Loop with STM Downmixing Method…….98

Figure A.1. STM downmixing readout circuit control panel…….102

Figure A.2. STM downmixing readout Labview Program……....103

FigureB.1 Schematic of STM downmixing with normal mixer……....104

Figure C.1. The measured results for higher modes of the MEMS device vibration……..107

Figure D.1. The detail resonance frequency and phase information of the forth flexural mode for different measuring points ……112

List of Table

Table 1.1 Numerical solutions for a doubly clamped beam……

Table 4.1 COMSOL Simulation Result for a long 500 μm, wide 100μm and thick 5μm Silicon Doubly-clamped Beam with Au and Cr Metal Layers…56

Table 4.2 Optical Interferometry Measurement Results for a long 500 μm, wide 100μm and thick 5μm Silicon Doubly-clamped Beam with Au and Cr Metal Layers……58

Table 4.3 STM Downmixing Measurement Result for a long 500 μm, wide 100μm and thick 5μm Silicon Doubly-clamped Beam with Au and Cr Metal Layers……..66

1.1. Chapter 1 Introduction

1.1 Overview of nanoelectromechanical system

Micro or nano-electromechanical systems (MEMS or NEMS) are a small integrated system which incorporates nano- or micro-scale mechanical elements, sensors, actuators, and electronics on a substrate through microfabrication or nanofabrication [1, 2]. They have a host of exciting attributes including ultrahigh frequency operation, ultrasensitivity, ultralow power, high responsivity, and small size scale making them potentially useful in a wide range of application. They have played and will continue to play a very important role for a fundamental study of mechanical motion in the quantum limit [3] [4] [5]. MEMS and NEMS have been a tool in the research in physics, biology and engineering. Many scientists share a great interest in miniaturization technologies and in studying the behavior of materials and structures in the micro- and nanometer range. The investigation of the small world of matter is crucial to understanding how things work and this knowledge can be used to create novel microstructures and devices, thus offering the necessary tools and components to realize applications of great societal importance.

Micro and Nano-electromechanical systems are a fascinating field. Here one mechanical resonator owns a simple geometry, such as a cantilever (a beam clamped at one end) or a bridge (a beam clamped at both ends), and is fabricated based on the material such as silicon using similar techniques employed for semiconductor chip manufacturing. In the submicron size regime, these mechanical resonators can vibrate at frequencies up to and beyond a gigahertz and preserve very high mechanical responsively (small force constant). This powerful combination of attributes translates directly into high force sensitivity, and operability with quite modest control force.

The minuscule mass and high quality factor of MEMS and NEMS show promise for foundationally different forms of mass sensing, where the mass of a small

particle attaching itself to a nanomechanical resonator can be determined from the resulting vibrational frequency-shift of the resonator. For example, extraordinary mass sensitivity levels in the zeptogram ($1zg = 10^{-21}g$) range have been exhibited [6]. With the use of suitably-engineered high frequency NEMS, a new paradigm of mass spectrometry is now conceivable in which the detection of individual molecules should be possible at single-Dalton sensitivities ($1\ Dalton = 1.66\times10^{-27}kg$, 1/12 the mass of a C^{12} atom) [7] [8]. This extreme sensitivity to mass combined with selective binding sites is enabling next generation detection methods of hazardous chemicals and biological agents [9].

Another application is force microscopy, where a cantilever tip is scanned over a surface and the cantilever displacement measured as the tip interacts with the surface used to build up a force topography map. Of particular interest is the magnetic resonance force microscope (MRFM) which employs a ferromagnetic cantilever tip, enabling the mapping of unpaired electron and nuclear spin densities at and below the surface [10]. Recently, single electron spin detection sensitivities were achieved [11] [12] [13]; the potential applications of being able to determine chemical identity at the single molecular or atom level are numerous. And with the use of smaller, suitably-engineering NEMS MRFM devices, the higher mechanical frequencies might result in faster read-out times at equivalent or better sensitivities.

MEMS and NEMS also have the potential impact on the field of information and communications technology in chip-level signal processing, for instance, MEMS and NEMS could replace filters, antennas, and oscillator clocks in mobile phone [14]. Otherwise, in life science MEMS and NEMS play an important role through ultrasensitive devices for chip-level bio-sensing and gas detection.

For all the nanotechnology applications of NEMS and MEMS devices, a key challenge is to figure out a fast, low-noise technique for translating small mechanical motion into reasonable electric signals to measure. Solving this problem will one day make it possible to build electric signal processing devices

that are much more compact than their purely electric counterparts. In this paper we will simply discuss the resonator motion and motion detection, and then we will focus on the displacement detection method of STM downmixing readout of nanomechanical motion.

1.2 Mathematical Description of Resonator Motion

Various geometric NEMS devices have been fabricated and investigated, such as doubly-clamped beams, paddles, cantilevers and nanowire. In this paper, we will focus specifically on doubly-clamped beams whose geometry is given in Fig. 1.1.

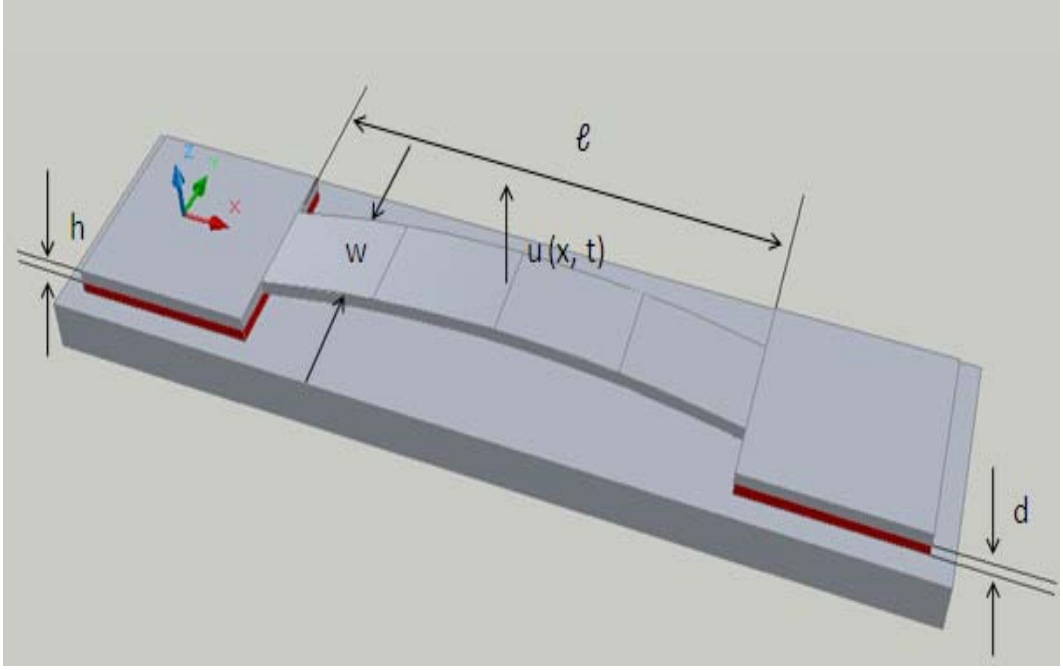

Figure 1.1 Doubly-clamped beam with length ℓ, width w and thickness h suspended a distance d above the Si substrate.

The equation of motion for this device geometry with force f(x, t) can be derived from Euler-Bernoulli beam theory [2] and can be written as:

$$EI\frac{\partial^4}{\partial x^4}u(x,t)+\rho A\frac{\partial^2 u(x,t)}{\partial t^2}=f(x,t) \qquad (1.1)$$

where E is Young's modulus, I is the moment of inertia ($I = h\omega^3/12$), ρ is the mass density per unit length, and A is the cross sectional area ($A = \omega h$). The time varying displacement $u(x, t)$ varies along the length of the resonator and will have a maximum displacement at the midpoint. To estimate the resonant frequencies of this structure, we must consider free vibration and let $f(x, t) = 0$. Eqn. 1.1 can be solved by the separation of variables method where the real displacement $u(x)$ is expressed as a product of space and time, namely

$$u(x,t) = \mathrm{Re}[u(x)e^{iwt}] = \hat{u}(x)\cos(\omega t) \tag{1.2}$$

For a natural mode of vibration ($\omega=\omega_0$), we can obtain a modal solution where ϕ_n corresponds to the *nth* mode vector.

$$u(x,t) = \phi_n(x)\cos(\omega t) \tag{1.3}$$

All structures fabricated for this study had cross sections and material properties that did not vary along the length of the beam. Incorporating that the products

EI and pA are constant; the derivatives of Eqn. 1.3 are substituted into Eqn. 1.1 to provide a homogeneous ordinary differential equation

$$\frac{d^4\phi_n(x)}{dx^4} - K_n^4\phi_n(x) = 0 \tag{1.4}$$

$$K_n = \left(\frac{\rho A}{EI}\right)^{1/4}\omega_n^{1/2} \tag{1.5}$$

Here K_n is the wavenumber and is a constant for each mode with resonant frequency ω_n. From Eqn. 1.4, we see that the spatial dependence depends on a fourth order equation and therefore four boundary conditions are required for an exact solution. For a beam clamped at both ends, the displacements $\phi(x)$ and

slopes *dø/dx* must be zero at both ends of the beam (e.g., at $x = 0$ and at $x = \ell$).The solution to Eqn. 1.4 provides the beam deformation shape for each mode and can be expressed in terms of real functions.

$$\phi_n(x) = C_{1n}(\cos(K_n x) - \cosh(K_n x)) + C_{2n}(\sin(K_n x) - \sinh(K_n x)) \tag{1.6}$$

with eigenvectors K_n meeting the condition:

$$\cos(K_n l)\cosh(K_n l) - 1 = 0 \tag{1.7}$$

where the zeroes of this equation are found numerically to be $K_n\ell$ = 0, 4.73004, 7.8532, 10.9956, 14.1372 . . . The corresponding resonant frequencies can be found by rearranging Eqn. 1.5

$$\omega_n = (\frac{EI}{\rho A})^{1/2} K_n^2 \tag{1.8}$$

The fundamental resonance for a doubly clamped beam can then be expressed as [2]

$$f_0 = 3.56\sqrt{\frac{EI}{\rho A}}\frac{1}{l^2} \tag{1.9}$$

or alternatively by substituting $I = \frac{h\omega^3}{12}$ and $A = \omega h$ as

$$f_0 = 1.028\sqrt{\frac{E}{\rho}}\frac{h}{l^2} \tag{1.10}$$

And the higher modes are f_n/f_0 = 2.756, 5.404, and 8.933 for n=2, 3, and 4.

The eigenfunction $\phi(x)$ in equation (1.4) are mutually orthogonal, and we normalize them to the beam length, so that

$$\int_0^{\ell} \phi_n(x)\phi_m(x)dx = \ell^3\delta_{mn} \qquad (1.11)$$

The corresponding coefficient C1n and C2n are listed in Table 1.1[15]. An arbitrary solution u(x, t) to undriven and driven motion can be written as:

$$u(x,t) = \sum_{n=1}^{\infty} a_n(t)u_n(x) \qquad (1.12)$$

where the amplitudes a_n are dimensionless.

Table 1.1 Numerical solutions for a doubly clamped beam

	n=1	2	3	4
$K_n\ell$	4.73004	7.8532	10.9956	14.1372
υ_n/υ_1	1	2.756	5.404	8.933
C_{1n}/ℓ	-1.0000	-1.0000	-0.9988	-1.0000
C_{2n}/ℓ	0.9825	1.008	0.9988	1.0000

Now let us go back to equation (1.1) and add a harmonic driving force with the expression, $f(t) = f\exp(i\omega_c t)$, where f is the position-independent force per unit length. The force is uniform across the beam cross section and directed along Z, and the carrier frequency ω_c is close to ω_0. The equation of motion can be written as:

$$EI\frac{\partial^4}{\partial x^4}u(x,t)+\rho A\frac{\partial^2 u(x,t)}{\partial t^2}=fe^{i\omega_c t} \tag{1.13}$$

The solution of this equation has the form $u(x, t) = u(x)$ exp ($i\omega_c t$). The amplitude $u(x)$ may be complex, so that the motion is not necessary in phase with the force f. Expanding the displacement in terms of the eigenfunction u_n,

$$-\omega_c^2\rho A\sum_{n=1}^{\infty}a_n u_n(x)+EI\sum_{n=1}^{\infty}a_n\frac{\partial^4 u(x)}{\partial x^4}=f \tag{1.14}$$

From this equation we can express the amplitude as:

$$a_n=\frac{1}{\rho A\ell^3}\frac{1}{\omega_n^2-\omega_c^2+i\omega_n^2/Q}\int_0^{\ell}u_n(x)f dx \tag{1.15}$$

Equation (1.15) gives the correlation between the driving force and the vibration amplitude of mechanical element.

1.3 Fabrication of micro- and nano-electromechanical devices

The fabrication processes of MEMS and NEMS devices can be classified into two approaches. Top-down approaches, which developed from the semiconductor fabrication technology, utilize micro or nano fabrication techniques, such as electron-beam lithography, thin-film growth techniques and etching techniques to fabricate structures from bulk material, either membranes or bulk substrate. Bottom-up approaches fabricate the nanoscale devices by sequential assembly of atoms and molecules as building blocks, and then connect them to the outside world.

The devices which are used in this project are fabricated on silicon-on-insulator (SOI) wafers, as showed in Figure 1.3 (a), with top-down approaches. SOI is a sandwich structure with one silicon dioxide layer located in the middle between the structural silicon layer and the substrate silicon. In our experiment, we choose

the SOI wafers whose thickness of the structural Si is 5μm and sacrificial SiO_2 layer is 4μm. The wafers are fabricated with a bonding and etch-back technique, which can get very smooth interfaces.

Before the fabrication, the SOI wafer is required to be cleaned. The process is that the SOI wafer is etched with BOE for 30 seconds to avoid thin silicon dioxide at the surface. Then the DI water is used to rinse the wafer and make sure no BOE is the surface. After that the wafer is put into piranha solution (H_2SO_4 : H_2O_2=3:1) to clean organic residues off the substrate for 20 minutes because piranha solution is a strong oxidizer and it will remove most organic matter. Thus after rinsing and drying, the cleaned wafer can be used for MEMS fabrication.

The first fabrication process of MEMS devices is sputtering which will deposit a layer to the surface of the wafer. This layer will act as the bonding pad and the tunneling surface. Since tunneling takes place between the atoms on the surfaces of the tunneling electrode, it is critically important that electrode material would be conductive to tunneling such as a metallic. Au film is a nearly ideal metal layer for this purpose because it does not undergo chemical reactions to form insulating surface layers when exposed to air. Based on our experimental requirement, the layer is chosen to be the double layers, gold and chromium. Chromium is selected due to its ideal adhesion properties to Si surface and Au. Au has a good tunneling surface for STM and bonding wire. Thus a thickness of 20nm chromium will be deposited at the surface of silicon and a thickness of 200nm gold is coated on the chromium layer, as shown in Figure 1.3 (b).

After sputtering, photolithography process is used to define MEMS device patterns. Photolithography process is an important step to decide the future size of devices. In the photolithography process, one starts the fabrication by spin-coating photosensitive organic film, namely the photoresist, upon the wafer where the structures will be fabricated, shown in Figure 1.3 (c). The coated wafer is soft-baked for a few minutes to dry out the solvent, hardening the coating layer. The photoresist is then exposed to ultraviolet (UV) light through the patterned photo-

mask, thereby transferring the pattern on the mask onto the photoresist. The common exposure process is contact exposure and is shown as Figure 1.2. Because the MEMS are fabricated in our experiment, we choose contact exposure. The exposed wafer is put into developing solution to remove the part out of the devices. Thus the patterns are defined.

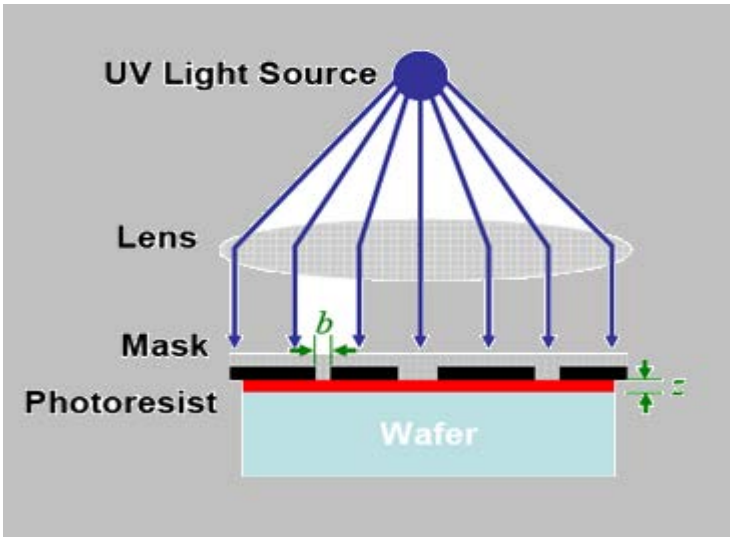

Figure 1.2 Schematic drawing illustrating contact exposures

Right now the wafer with device patterns is required to etch away the extra alloyed layer and silicon. The wet etch is used to remove the alloyed layer, Au and Cr. After that, photoresist of wafer surface is lifted with acetone and the metal shown in Figure 1.3(d) can be served as a robust mask protecting the thin Si which will become the device. The unprotected silicon area is etched through into the SiO_2 layer with reactive ion etching (RIE), as shown in Figure 1.3(e). Based on big selective ration between Si and Silicon dioxide, during the RIE over-etching is required and this can avoid leaving a thin silicon layer at the surface which will block to remove the sacrificial SiO_2 layer.

The last step of fabrication is to etch the sacrificial layer of SOI and release the devices. The wafer is put into the BOE solvent and the silicon dioxide is etched. The time is controlled in order to get the suspended NEMS structures as shown in Figure 1.3(f). After the wafer is taken out of the BOE etchant, it is rinsed in

multiple DI water baths to make sure no BOE solvent is left. Thus the devices are done. We will dice the wafer into single device die for measurement.

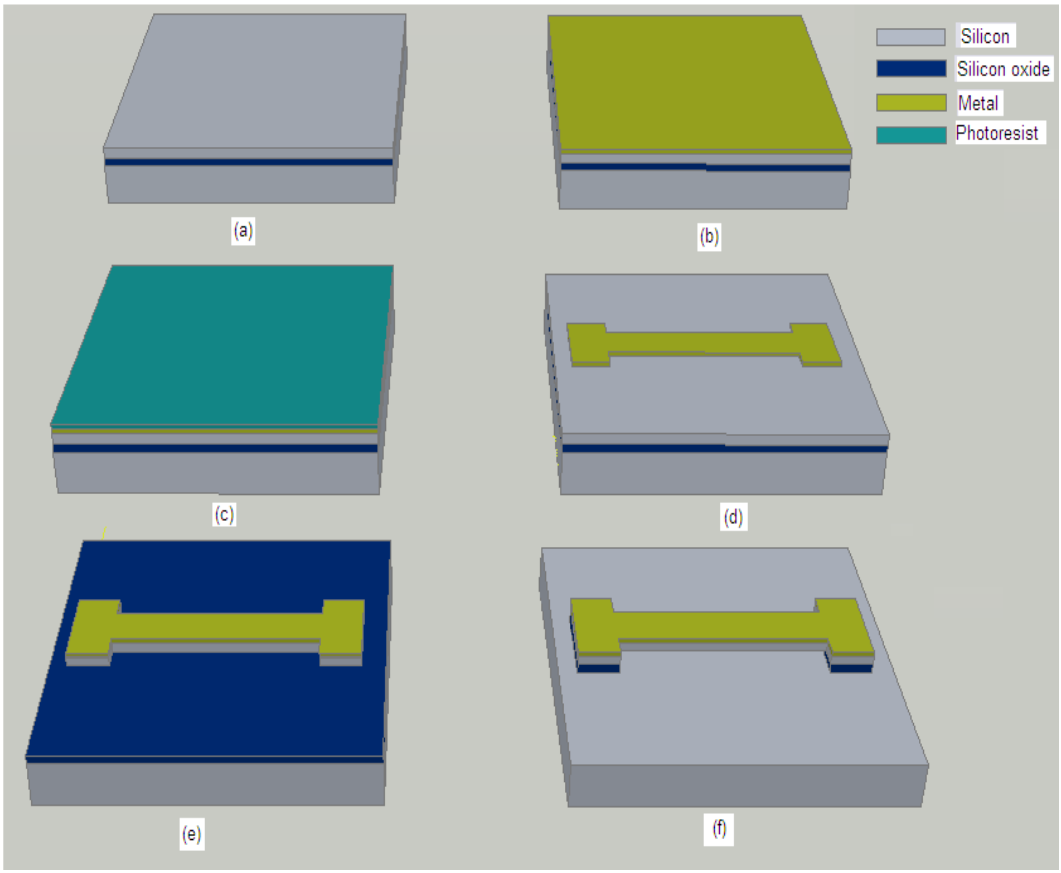

Figure 1.3 The process steps to fabricate suspended doubly clamped beam with photolithography. (a) SOI wafer. (b) The wafer is coated with metal (Au and Cr). (c) The wafer is coated with metal and photoresist. (d) Metal layer is patterned with photolithography and etched. (e) Alloyed layer and Silicon layer are etched away. (f) Silicon dioxide layer is etched through.

One important problem for the devices using this fabrication process is stiction. When the devices are removed from solution, the surface tension in the liquid pulls the suspended structures down to the surface. Once this occurs, the structures remain stuck and are effectively damaged (unusable). Though careful

fabrication is done, these problems can't always be avoided and this impacts the yield. The doubly-clamped and stiffer nature of the devices is chosen to help to avoid this issue to a degree while at the same time helping to allay snap-to-contact issues with the STM tip.

1.4 Displacement detection of NEMS

The miniscule MEMS and NEMS own high sensitivities and tiny displacement when they are driven. Thus the detection of tiny displacement for MEMS and NEMS is an important problem. Before we introduce our project and technique, I will simply introduce some techniques which are available for displacement detection.

1.4.1 Optical Technique

Optical interferometry which combines two or more light waves in an optical instrument in such a way that interference occurs between them has been used in the NEMS domain [16] [17] [18] to detect the motion of NEMS. There are two popular methods: path-stabilized Michelson interferometry and Fabry-Perot interferometry. In the case of Fabry-Perot interferometry, the optical cavity which is formed between the NEMS device and the silicon substrate can modulate the optical signal on a photodetector as the NEMS device moves along with the optical beam direction. Figure 1.4(a) displays schematic diagrams of Fabry-Perot interferometry. In path-stabilized Michelson interferometry, a focused laser beam reflects from the surface of a vibrating NEMS device and interferes with a stable reference beam, as shown in Figure 1.4(b).

Optical methods provide a non-contact means for displacement detection and are desirable because of their demonstrated sensitivity and broadband operation. However, in both of the above-described techniques, strong diffraction effects emerge as the NEMS dimensions are reduced beyond the optical wavelength used. The light collected by the probing lens is reduced to a small fraction of the incoming light due to strong scattering. This strong scattering, accompanied with

the requirement that low optical power levels must be used for probing NEMS due to the heating effect, make optical displacement detection difficult for the smaller devices.

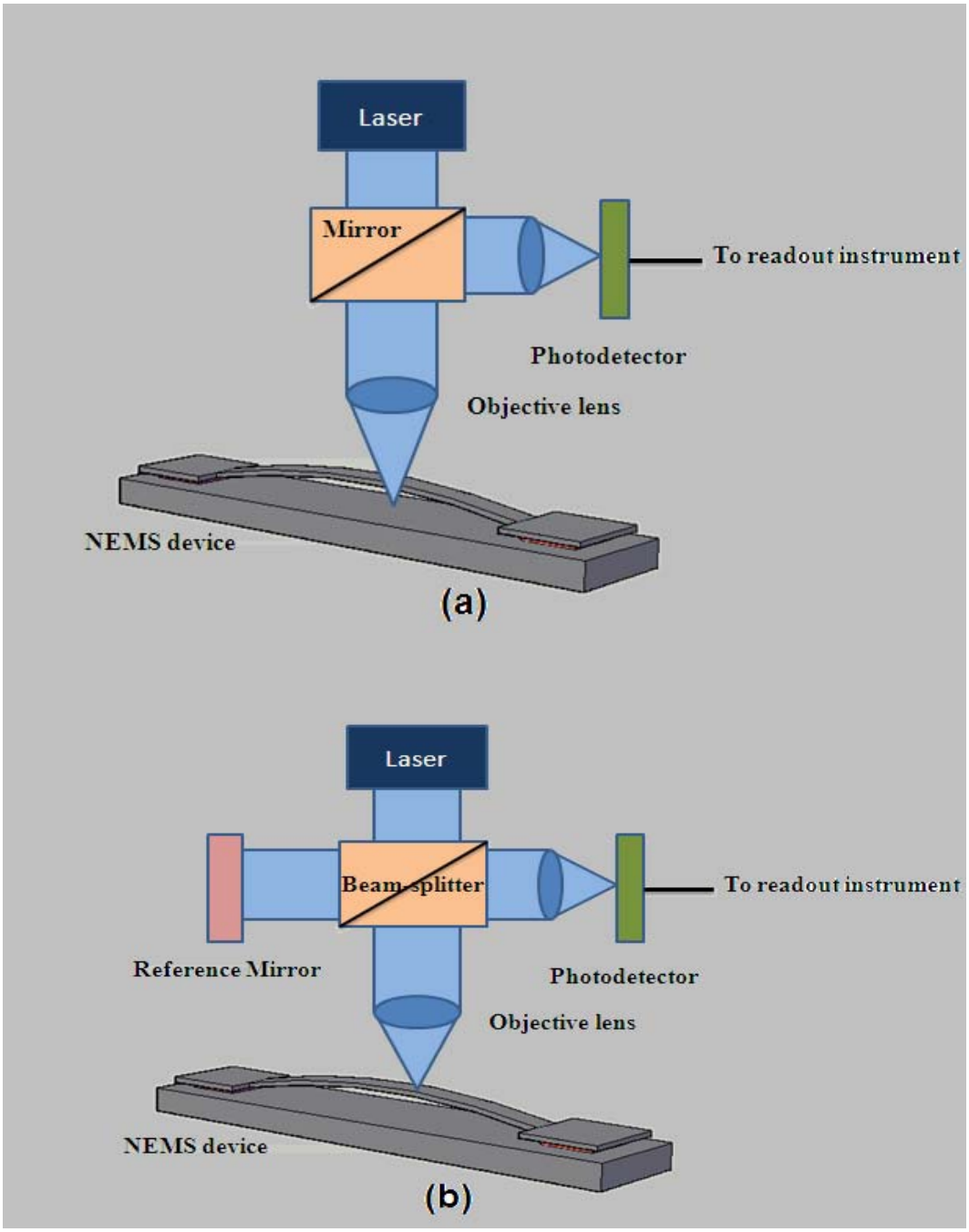

Figure 1.4 Optical displacement detection in NEMS (a) Fabry-Perot interferometry (b) Michelson interferometry

1.4.2 Magnetomotive Techniques

Magnetomotive displacement detection technique is employed into the NEMS domain by Cleland and Roukes in 1996 [19]. A uniform magnetic field is applied to a conducting nanomechanical element. When the nanomechanical element is moving, the time-varying flux generates an induced electromotive force (emf) in the loop, which, in turn, can be picked up by the detection circuit. For a doubly clamped beam, the Magnetomotive technique generates an emf voltage given by

$$V_{emf}(t) = \xi l B \dot{u}(t) \tag{1.11}$$

Here B is the magnetic field strength, ℓ is the length of the beam, ξ is a geometric factor (ξ≈0.885 for a doubly clamped beam) [20], u (t) is the displacement of the midpoint of the beam and the beam is assumed to exhibit constant amplitude harmonic oscillations at a frequency ω. For the extremely small displacement, the emf which is generated due to the motion of NEMS should be small. Thus a low-noise amplifier is required to amplify the signal. The Figure 1.5 shows the magnetomotive displacement detection. This method has been efficient for VHF and ultrahigh frequency (UHF) NEMS [21] [22].

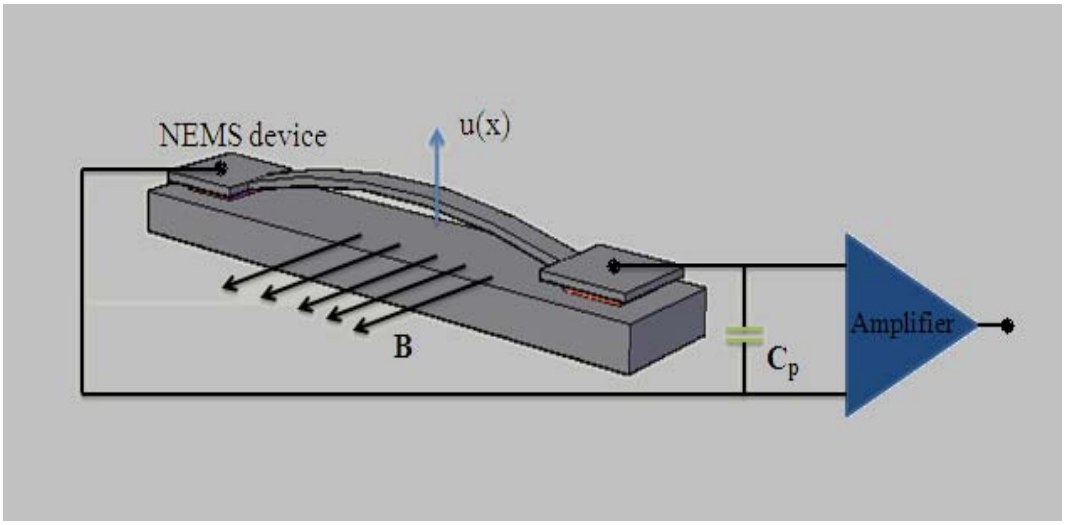

Figure 1.5 Magnetomotive displacement detection

Due to the parasitic capacitances in the detection circuit, the detection bandwidth of the magnetomotive technique is limited. In order to detect high frequency NEMS motion small parasitic capacitance and resistance are required and these limit the development of this technique. Also there are difficulties associated with implementing the magnetomotive detection scheme when the device is being actuated by electrical or magnetomotive actuation. Because the degree of orthogonality of the actuation and detection is reduced by the parasitic capacitance between the input and the output, this makes the implementing of magnetomotive detection difficult [23]. Some methods are investigated to solve this problem, such as a reflection measurement scheme.

1.4.3 Capacitive Displacement Detection

In capacitive displacement detection, the electrical capacitance between the mechanical device and a fixed gate is varied with the motion of mechanical device and the basic configuration is shown in Figure 1.6(a). A DC bias voltage is applied on the capacitor and a change in the voltage (current flow) across the capacitor is detected. It can be understood from the definition of capacitance, $Q=CV$ and $dQ = VdC + CdV$. Consequently, a capacitance change at constant current (voltage) will generate a voltage (current flow) across the capacitor. Here, Q is the charge on the capacitor and V is the voltage across capacitor. Figure 1.6(b) shows an implementation along with a conceptual detection circuit. The parasitic capacitance in this measurement scheme will be extremely important. The parasitic capacitance determines the detection bandwidth and the limits of capacitive detection of motion.

Some ways can be used to eliminate the effect of the parasitic impedance. Balanced bridge techniques may help readout the small dynamic capacitance changes efficiently by negating the capacitive background. Impedance matching technique by using an LC impedance transformation network is developed to measure the small motion of NEMS [24]. One could also use the mixing techniques to measure the mixing signal [25]. Otherwise, a single-electron

transistor has been used to measure a NEMS resonator with the NEMS electrode serving a dual function as both the motion sensor for the NEMS, and as the gate electrode of the SET readout [26] [3].

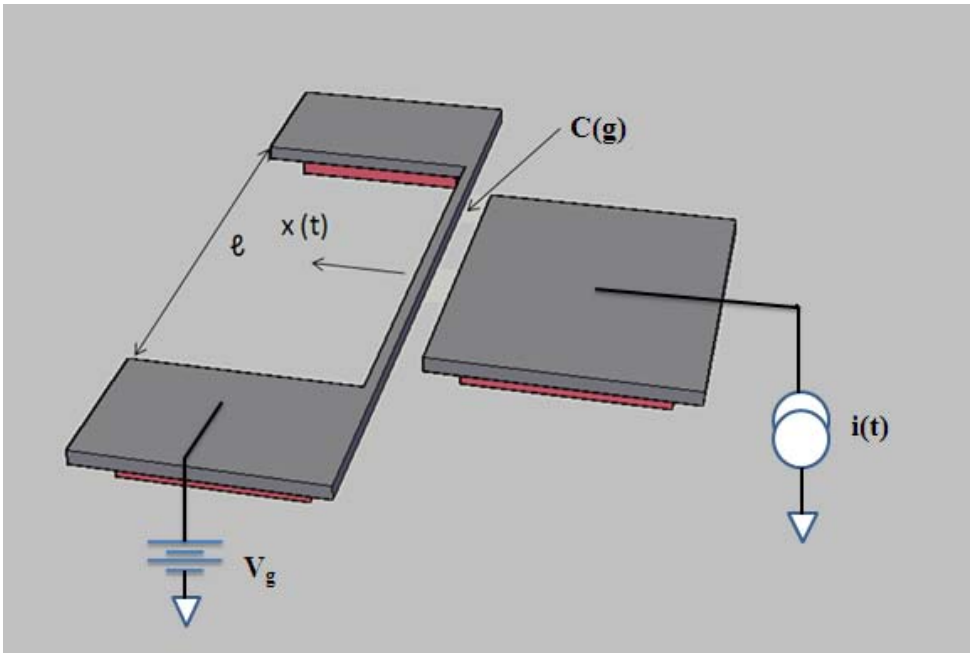

(a)

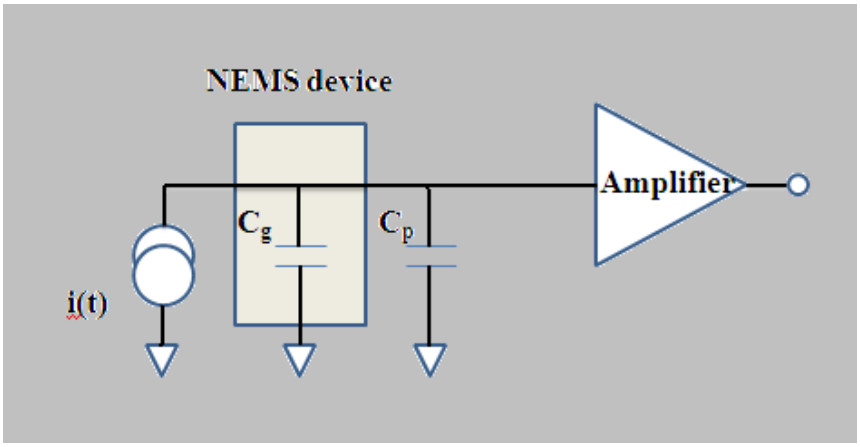

(b)

Figure 1.6 Capacitive displacement detection (a) The diagram of capacitive detection in a doubly clamped NEMS beam (b) The circuit of capacitive detection

1.4.4 Piezoresistive and Piezoelectric Detection

A piezoresistive material is one that exhibits a changing electrical resistance due to applied mechanical stress. Similarly, a piezoelectric material can generate an electrical polarization change in response to applied mechanical stress. Both the effects are sensitive to the stress generated inside a material during the motion. One can use it to do displacement detection.

Piezoresistive sensing can be realized by detecting the resistance changes through a piezoresistive NEMS device as it is actuated. Compared with other detection methods, piezoresistive NEMS have the advantages of being easily integrated sensors that can operate from room temperature down to at least 4 K and do not require magnetic field. The shortcoming of this sensing technique, however, is the intrinsically high resonances (5-500 kΩ) of these devices which lead to frequency-dependent signal attenuation at MHz frequency if direct-current (dc) biasing is used. In order to use this method for the high frequency, one investigates some ways, such as piezoresistive signal downmixing [27].

In the piezoelectric method, one exploits the polarization fields created by the stress field within the piezoelectric nanomechanical element as it moves. This method also has problems at high frequency. Some people have intended piezoelectric detection in NEMS using a single-electron transistor [28] to improve this method.

1.4.5 Electron Tunneling Detection

Displacement transducers based on electron tunneling have been proposed for a variety of physical sensors, because of the high position sensitivity of electron tunneling. Advantages of electron tunneling displacement transducers include high sensitivity, small transducer size, and compatibility with silicon micromachining technology. The tunneling transducer is generally realized in the form of a sharp tip placed within a fraction of a nanometer of the moving mechanical element. The tip can convert the motion of the mechanical element

into an electron signal by the change of tunneling current. The tunneling current is very sensitive to the distance change between the tip and the surface of the sample due to the exponential correlation with the distance. An electron tunneling transducer followed by an amplifier (current-to-voltage converter) is displayed in Figure 1.7.

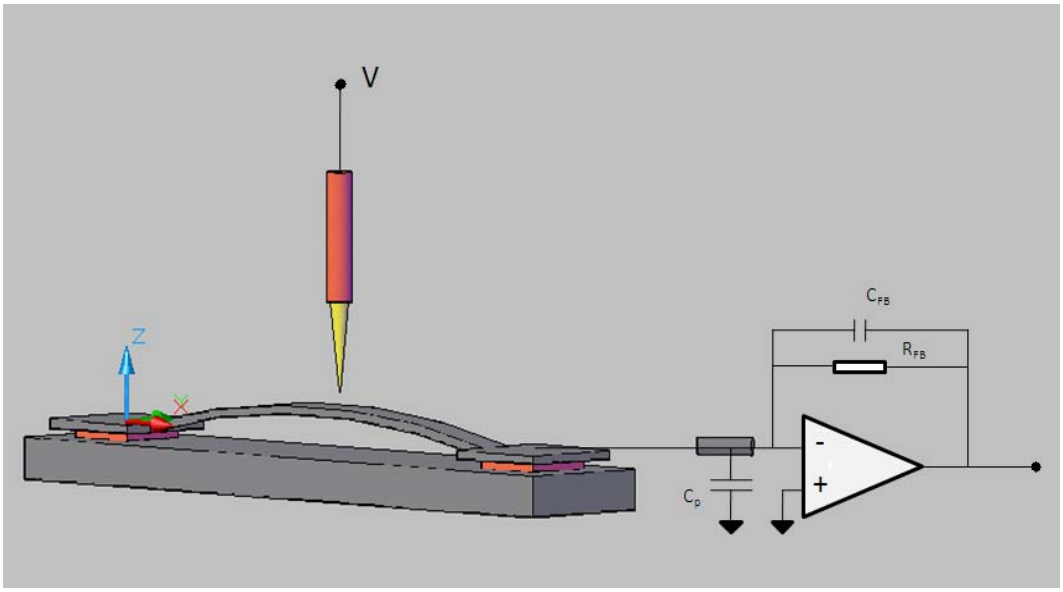

Figure 1.7 Electron tunneling transducer for displacement detection

Electron tunneling transduction as shown in Figure 1.7 has a limit for high frequency application due to the parasitic capacitance C_p and high impedance of the tunneling junction resistance. Usually the limit of frequency is about 10 KHz and this obstructs the development of electron tunneling transducers at high frequency. In our thesis we will focus on the improvement of electron tunneling transducer as displacement detection, particularly for frequencies above the traditional STM bandwidth.

1.5 Motivation of This Thesis

The capabilities of the scanning tunneling microscope (STM) as an imaging tool are well known and appreciated. Also the capabilities of the tunneling probe of the scanning tunneling microscope as a displacement sensor attract attention.

Tunneling of electrons through the space separating two electrical conductors is a special event of the quantum nature of matter. One observes that the tunneling current between two conductors separated by vacuum is exponentially dependent on the gap with a scale of a few angstroms, so the small displacement of NEMS can be captured with the electron tunneling sensor.

Although electron tunneling detection has its advantages, some factors limit its development. As we know, in normal STM operation, there is a constant resistance R_T from 1MΩ to 1GΩ which is located between the tip and the sample. This resistance will form a RC circuit with the stray capacitance C_p coming from macroscopic wiring to limit the bandwidth to $1/2\pi R_T C_p \sim 10kHz$, as shown in Figure 1.8. This frequency limit is far from the fundamental limit of electron tunneling, I_T / e, which is the tunneling rate of a single electron determined by its tunneling current and elementary charge e. For a STM system, the tunneling current I_T is around 1nA and this mean the available bandwidth of STM is around 1GHz.

Until now, some methods are demonstrated to achieving higher frequency resolution with the STM. Direct RF measurements on the tunneling current have shown signatures of electron spin resonance (ESR) at high frequencies [29] [30]. Employing several amplifier stages instead of a single trans-impedance amplifier [31] [32] improves the time resolution, but with an undesirable problem in the signal-to-noise ratio. By inserting a LC impedance transformation network [33] one can transfer the impedance of the tunneling junction resistance R_T down to 50-ohm, but this way is difficult if the impedance mismatch ratio is greater than 100 and impractical if the same detection setup is to be used with many devices of different frequencies.

In our project, we will use AC biasing and the intrinsic properties of the NEMS to perform heterodyne downmixing of the signal to a lower frequency, which retains the high frequency motion information and can be detected by standard STM circuits without significant signal loss due to this output frequency is lower the

cut-off frequency of the whole detection loop. With this method we can improve the detecting frequency to GHz and improve the sensitivity of motion.

REFERENCE

1. Roukes, M. L., Nanomechanical system face the future*, Phys. World* 14, 25, (2001).

2. Cleland, A. N., *Foundations of Nanomechanics* (Heidelberg: Springer), (2002).

3. Naik, A., Buu, O., LaHaye, M. D., and Schwab, K. C., Cooling a nanomechanical resonator with quantum back-action, *Nature*, 443, 193, (2006)

4. O'Connell, A. D., Hofheinz, M., Ansmann, M, Bialczak, R. C., Lenander, M., Lucero, E., Neely, M., Sank, D., Wang, H., Weides, M., Wenner, J., Matinis, J. M., Quantum ground state and single-phonon control of a mechanical resonator, *Nature*, 464, 697, (2010)

5. Rocheleau, T., Ndukum, T., Maclin, C., Hertzberg, J. B., Clerk, A. A., Schwab, K. C., Preparation and detection of a mechanical resonator near the ground state of motion, *Nature*, 463, 72, (2010)

6. Yang Y. T., Callegar C., and Ekinci K. L., Zeptogram-Scale Nanomechanical Mass Sensing, *Nano Letters,* 6, 583, (2006).

7. Ekinci, K. L., Yang, Y. T., and Roukes, M. L., Ultimate limits to inertial mass sensing based upon nanoelectromechanical systems, *J. Appl. Phys.*, 95, 2682, (2004).

8. Naik, A. K., Hanay, M. S., Hiebert, W. K., Feng, X. L., and Roukes, M. L., Towards single-molecule nanomechanical mass spectrometry, *Nature Technology*, 4, 445, (2009)

9. Chiu, H. Y., Hung, P., Postma, H. W. C., and Bockrath, M., Atomic-scale mass sensing using carbon nanotube resonators, *Nano Lett.*, 8, 4342, (2008)

10. Sidles, J. A., Garbini, J. L., Bruland, K. J., Rugar, D., Z¨uger, O., Hoen, S., and Yannoni, C. S., Magnetic resonance force microscopy, *Rev. Mod. Phys.,* 67, 249, (1995)

11. Rugar, D., Budakian, R., Mamin, H. J., and Chui, B. W., Single spin detection by magnetic resonance force microscopy, *Nature*, 430, 329, (2004).

12. Hammel, P. C., Seeing single spins, *Nature*, 430, 300, (2004).

13. Degen, C. L., Poggio, M., Mamin, H. J., and Rugar, D., Nanoscale magnetic resonance imaging, *PNAS*, 106, 1313, (2009)

14. Nguyen, C. T.-C., MEMS technology for timing and frequency control, *IEEE Trans. Ultrason. Ferroelectr. Freq. Control*, 54, 251, (2007)

15. Cleland, A. N., Roukes, M. L., Noise process in nanomechanical resonator, *J. Appl. Phys.*, 92, 2758, (2002)

16. Carr, D. W., Sekaric, L., and Craighead, H.G., Measurement of nanomechanical resonant structures in single-crystal silicon, *J. Vac. Sci. Technol. B,* 16, 3821, (1998)

17. Meyer, C., Lorenz, H., and Karrai, K. Optical detection of quasi-static actuation of nanoelectromechanical system, *Appl. Phys. Lett.*, 83, 2420, (2003)

18. Kouh, T., Karabacak, D., Kim, D. H., and Ekinci, K. L., Diffraction effects in optical interferometric displacement detection in nanoelectromechanical systems, *Appl. Phys. Lett.,* 86, 13106, (2005)

19. Cleland, A. N., and Roukes, M. L., Fabrication of high frequency nanometer scale mechanical resonators from bulk Si crystals, *Appl. Phys. Lett.,* 69,2653, (1996)

20. Cleland, A. N., and Roukes, M. L., External control of dissipation in a nanometer-scale radiofrequency mechanical resonator, *Sensors and Actuators*, 72, 256, (1999)

21. Feng, X. L., White, C. J., Hajimiri, A., and Roukes, M. L., A self-sustaining ultrahigh-frequency nanoelectromechanical oscillator, *Nature Nanotech.*, 3 342, (2008)

22. Karabalin, R. B., Feng, X. L. and Roukes, M. L., Parametric Nanomechanical Amplification at very high frequency, *Nano Lett.*, 9, 3116, (2009)

23. Ekinci, K. L., Electromechanical transducers at the nanoscale: actuation and sensing of motion in nanoelectromechanical systems (NEMS), Small, 1, 786, (2005)

24. Truitt, P. A., Hertzberg, J. B., Huang, C. C., Ekinci, K. L. and Schwab, K. C., Efficient and sensitive capacitive readout of nanomechanical resonator arrays, *Nano Lett.*, 7, 120, (2007)

25. Sazonova, V., Yaish, Y., Ustunel, H., Roundy, D., Arias, T. A., and McEuen, P. L., A tunable carbon nanotube electromechanical oscillator, *Nature*, 431, 284, (2004)

26. Blencowe, P. M., Wybourne, N. M., Sensitivity of a micromechanical displacement detector based on the radio-frequency single-electron transistor, *Appl. Phys. Lett.,* 77, 3845, (2000)

27. Bargatin, I., Myers, E. B., and Roukes, M. L., Sensitive detection of nanomechanical motion using piezoresistive signal downmixing *Appl. Phys. Lett.,* 86, 133109, (2005)

28. Knobel, R., Cleland, A. N., Piezoelectric displacement sensing with a single-electron transistor, *Appl. Phys. Lett.,* 81, 2258, (2002)

29. Manassen, Y., Hamers, R. J., and Castellano, Jr., Direct Observation of the Precession of Individual Paramagnetic Spins on Oxidized Silicon Surfaces, *Phys. Rev. Lett.,* 62, 2531, (1989)

30. Durkan, C., and Welland, C. E., Electronic spin detection in molecules using scanning-tunneling-microscopy-assisted electron-spin resonance, *Phys. Rev. Lett.,* 80, 458, (2002)

31. Mamin, H. J., Birk, H., and Rugar, D., High-speed scanning tunneling microscopy: principles and applications, *J. Appl. Phys.,* 75, 161, (1994)

32. Rost, M. J., Crama, L., and Han, H. et al., Scanning probe microscopes go video rate and beyond, *Rev. Sci. Instrum,.* 76, 053710, (2005)

33. Kemiktarak, U., Ndukum, T., Schwab, K. C., and Ekinci, K. L., Radio-frequency scanning tunneling microscopy, *Nature*, 450, 85, (2007)

Chapter 2 Experimental Instrument

We first present the experimental instrument Scanning Tunneling Microscope (STM) [1] which will be used in downmixing readout of nanomechanical motion. The basic STM system is simply introduced and two operation modes of STM are described. We will talk about some modifications which are done in our system in order to adapt to our project and the general set-up. Simple operation of STM is described in the last section.

2.1 Scanning Tunneling Microscopy (STM) system

As a tool to investigate the surface of conductive sample Scanning Tunneling microscopy (STM) is a type of electron microscope and was invented by Bining and Rohrer in 1981. It is only one year later when the same group achieved an atomically resolved real space image of Si (111)-7x7 structure using STM [2]. Because STM work theory which is based on the concept of quantum tunneling and is sensitive to the small distance change, STM become a powerful instrument that can obtain atomic resolution on a metal, semiconductor or other conductive sample surface. When a conducting tip is brought very near, approximately 1nm, to a metallic or semiconducting surface, a bias between the two electrodes can allow electrons to tunnel through the gap between them because the electron wave functions of the tip and the sample slightly overlap in this distance. Both this overlap and the current exponentially decrease with the distance between the tip and the sample [3]. The schematic diagram of a scanning tunneling microscope is shown in Figure 2.1.

Usually, for STM system it can be operated in two modes which are called constant height mode and constant current mode respectively. For constant current mode, a feedback network changes the height of the tip at z direction to keep the current constant. The displacement of the tip given by the voltage applied to the piezoelectric driver then yields a topographic map of the surface. Figure 2.2(a) show a typical current mode operation and the change of current and position

during scanning. Alternatively, in constant height mode, the voltage applied to the piezoelectric driver and the height are both held constant while the current change to keep the voltage from change; this leads to an image made of current changes over the surface, which can be related to charge density, as displaced in Figure 2.2(b). This mode is not practical for rough surfaces. Compared two modes, constant height mode is faster, because the piezoelectric movements require more time to response the change in constant current mode than the current response in constant height mode. When STM is used to as displacement transducer, it can be operated in either mode depended the vibration amplitude of devices. But for constant height mode, we should carefully use to avoid damaging the devices and tip.

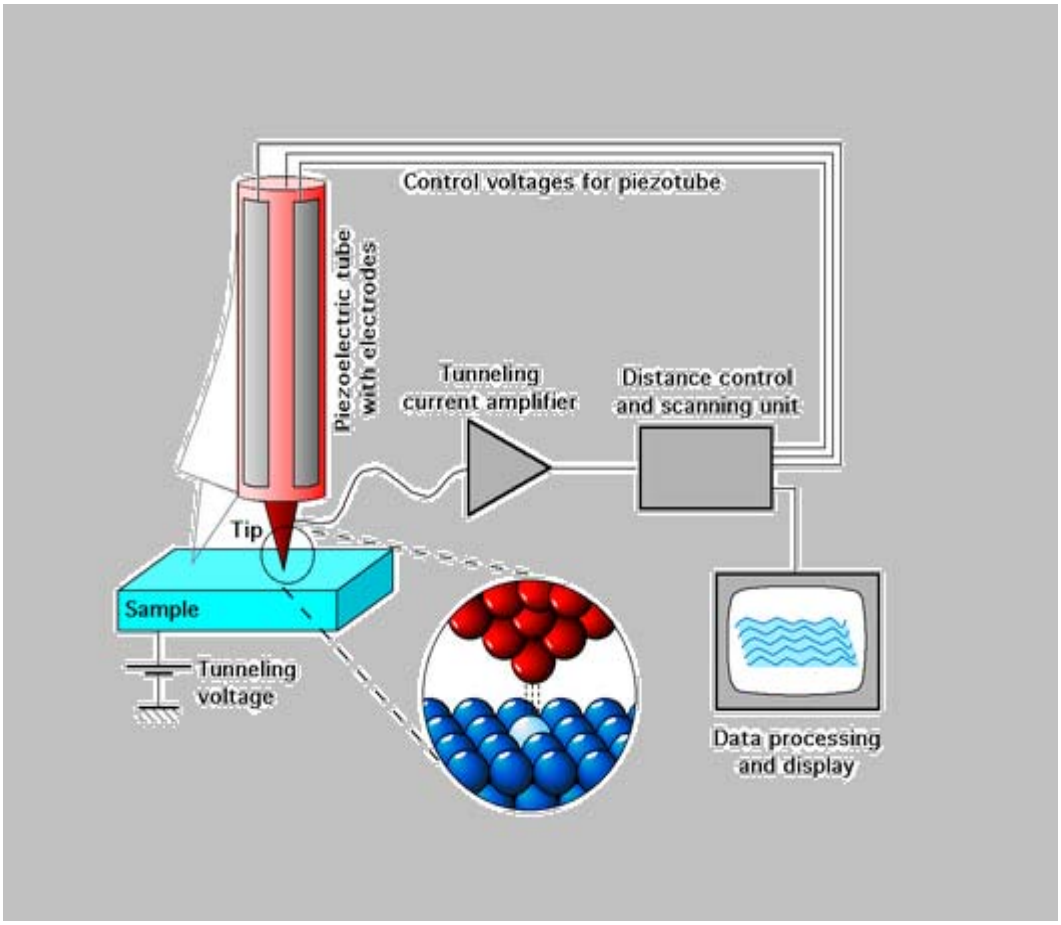

Figure 2.1 Schematic diagram of a scanning tunneling microscope (This graph comes from the Wikimedia Commons)

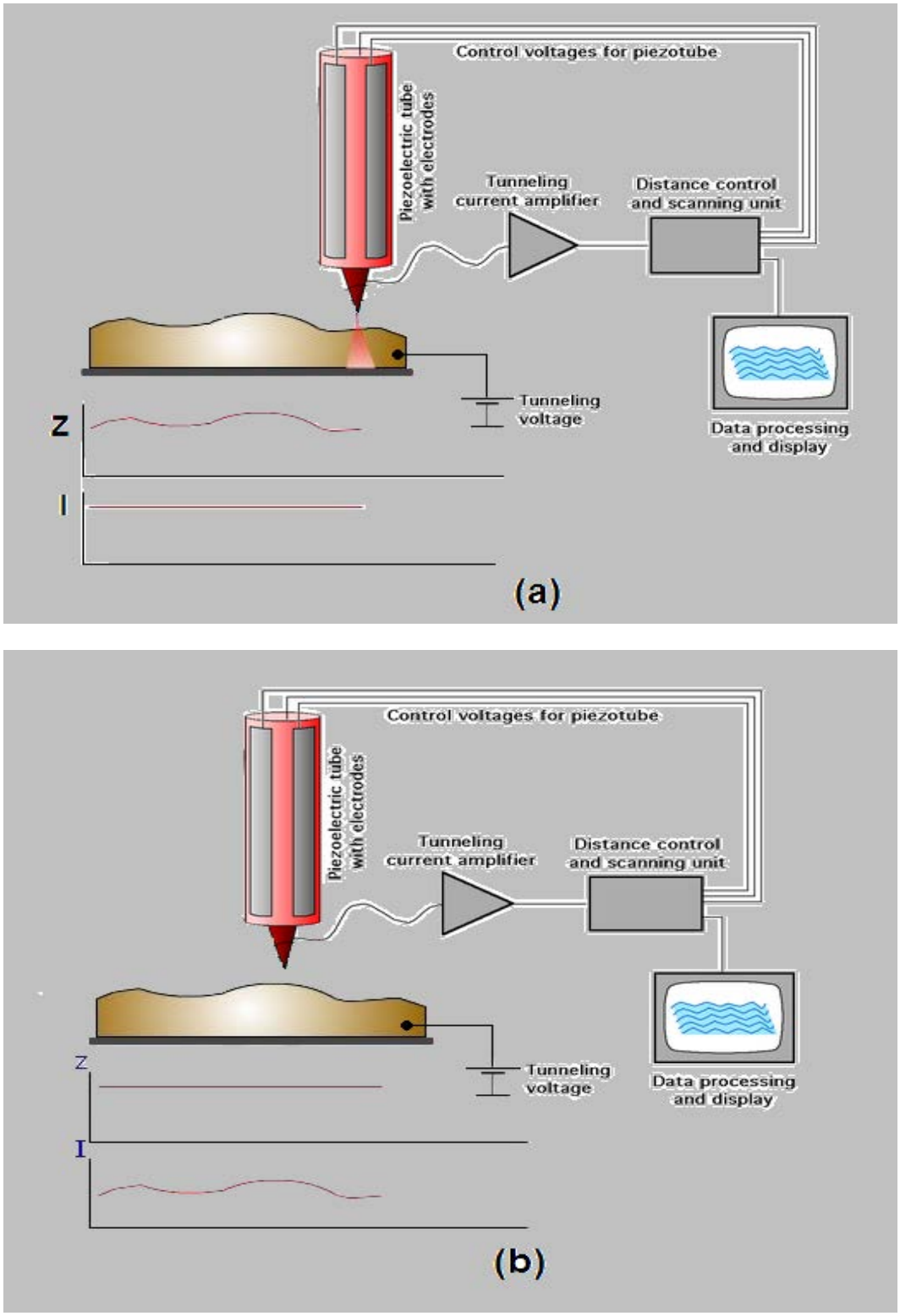

Figure 2.2 The schematic of two operation mode in STM (a) Constant-current mode and (b) Constant –height mode

2.2 The adaptations of the STM system

In our experiment, the STM system is the 1988 IBM model shown in the Figure 2.3. In order to make this STM an electron tunneling transducer for frequency downmixing readout, some updates and modifications were required. The approach system mechanical lever advantage was moved to either side to avoid direct contact with the device under test. The sample holder was correspondingly changes as well as updated for large range X and Y motion. A vacuum chamber was built around the STM system with multiple optical and electrical entry port options. An optical telescope for sample visual positioning while in vacuum was added. Finally, the electrical control system and software was updated

2.2.1 Modification of Mechanical Part of STM

For the STM mechanical parts, some adaptations are required to meet the measurement requirement of STM downmixing readout. These mainly include the approaching system and the sample holder.

For the approaching system of STM, the adjustment stop is redesigned. The old adjustment stop is too close to the tip as shown in Figure 2.3 inset which leave very little room for the sample to fit in. This will cause some problems. Firstly, the sample will be damaged due to the crash by the adjustment stop if the sample can’t fit in the small space. It is not convenient for moving the sample large distance over X and Y with response to the tip, it also makes aligning the tip on top of the sample difficult. Secondly, it is tedious to align the adjustment stop to the tip. Based on these problems, a new adjustment stop is designed and shown in Figure 2.4. These new support arms can avoid the above problems, but they require that the arms must be level in order to avoid the shift of chip due to unbalanced force in the two arms. This approaching system has the disadvantage that it is difficult to set the length of arms in order to ensure the sample is vertical to the tip.

The second problem is how to align the probe tip on the top of NEMS device. The optical telescope is about 10cm from the sample (see Figure 2.9) and thus limited to a numerical aperture around 0.2. Combined with a glancing viewing angle, NEMS devices are too small to be accurately landed on with aid of the telescope. With a mirror in improving the view angle rough alignment of NEMS devices with the probe tip become possible, however, fine alignment will still be necessary to successfully land the tip on a NEMS. For the fine alignment, some new techniques will be required. Electron field emission from the tip, as one example, may be a good method to find the NEMS devices. Our initial attempts to implement field emission fine alignment were unsuccessful due to dull and double tip shapes (see Figure 2.7). Based on this reason, in our experiment we measure MEMS-sized-devices. With this mirror, the MEMS devices can be aligned well, this is, the tip can be reliably placed onto the MEMS beams. The image of sample and tip is shown in Figure 2.5.

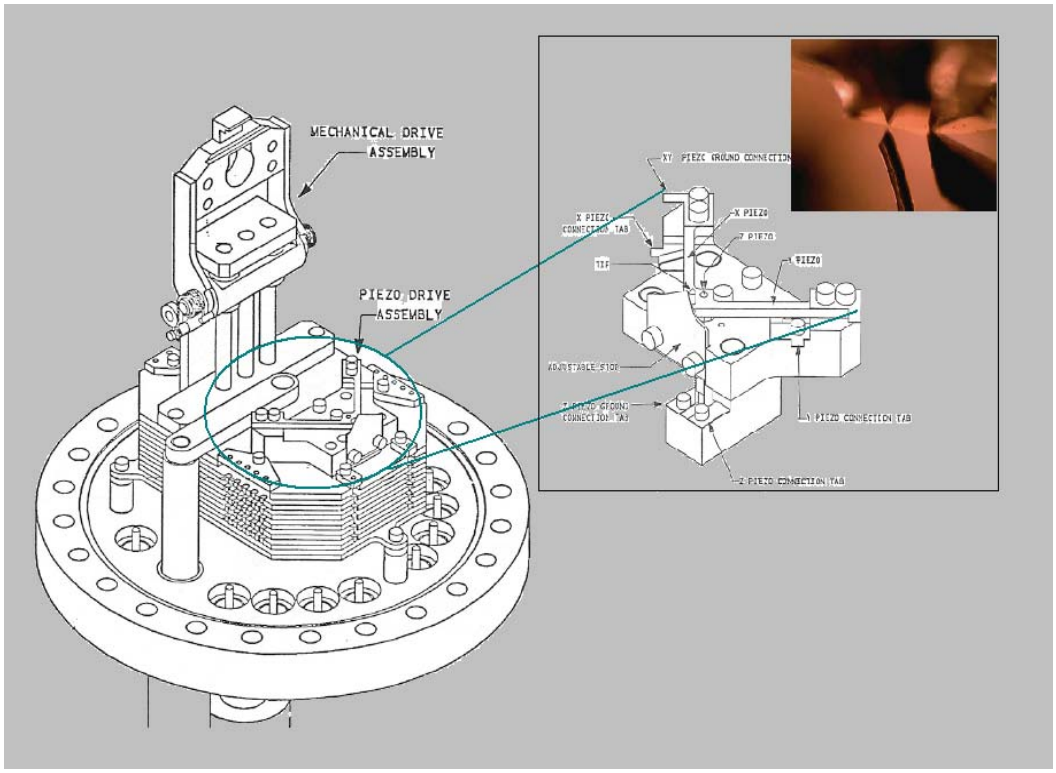

Figure 2.3 The schematic of STM mechanical part and STM sample approaching system (Inset)

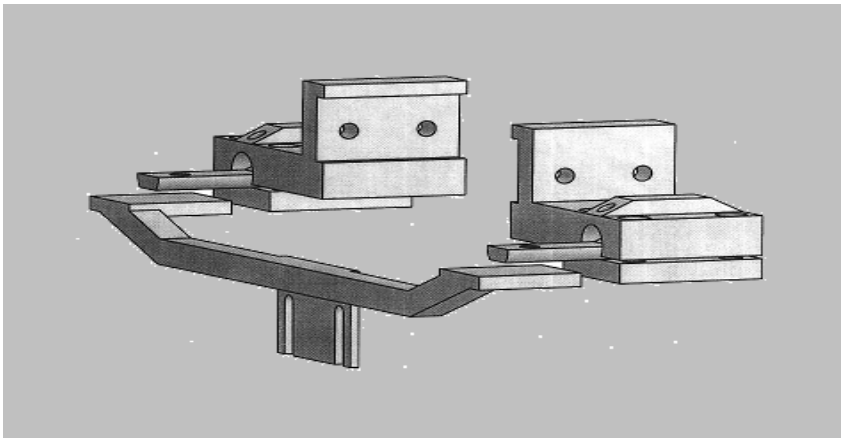

Figure 2.4 The schematic of new adjustment stop

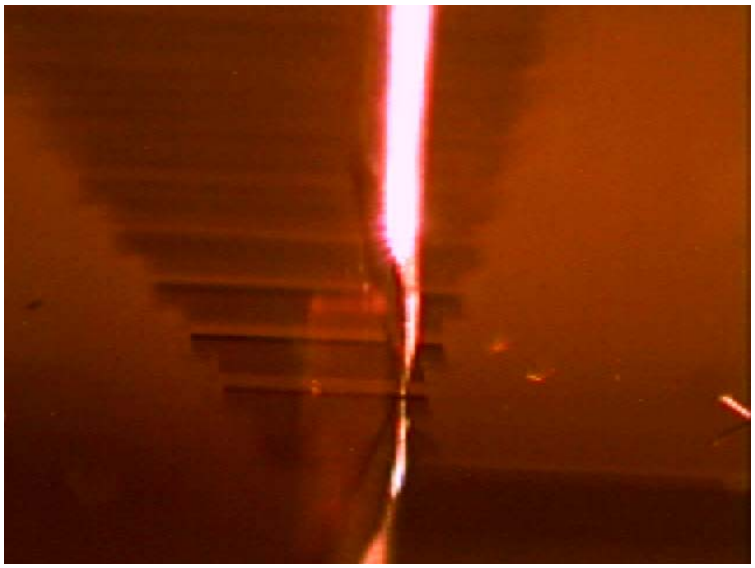

Figure 2.5 The image of MEMS device and tip in the mirror

One problem introduced by the alignment mirror, which is attached to the new mechanical advantage holder, is that is seems to cause significant additional mechanical noise of the measurement system and negatively impacts the sensitivity of the STM system. Additional job is needed in the future in order to overcome this mechanical noise. Similarly, field emission fine alignment will require future work in improved tip profiles.

We need to have a sample holder which can move along the XY plane in order to align on-chip features under the STM. The older sample holder is shown in Figure

2.6 (a) and it cannot move. This is not convenient to the alignment of sample and probe tip. In order to overcome this problem, a new sample holder is made like Figure 2.6(b). This new sample holder integrates an attocube system, as shown in Figure 2.6 (c). The new sample holder allows the sample to move large distance along X and Y directions with nm step resolution and it is convenient to align the probe tip on the top of MEMS devices.

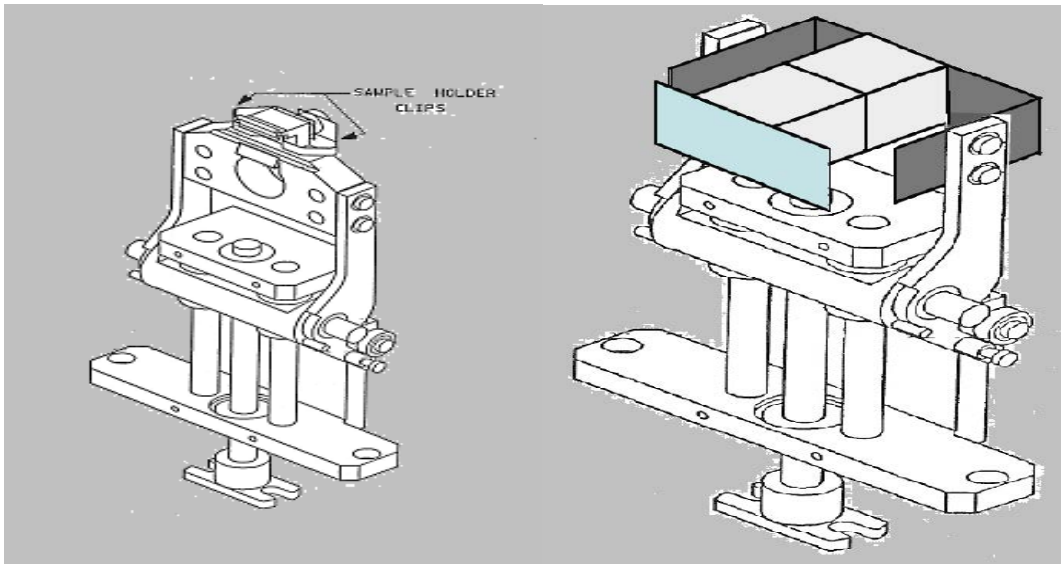

(a) (b)

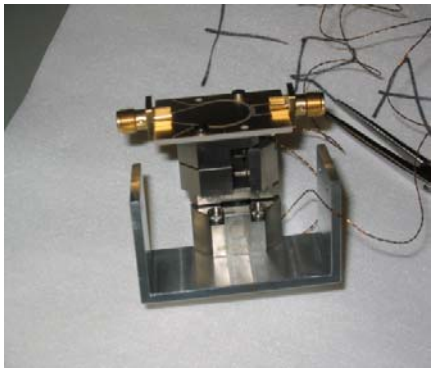

(c)

Figure 2.6 (a) The older sample holder (b) The Schematic of new sample holder and (c) The new sample holder with attocube System which can move along X and Y Plane

These adaptations make our STM mechanical part convenient for our measurement, although this system still has some problem which will require to improvement for finer feature measurement. Now it basically meets our measurement requirement for MEMS.

2.2.2 The Accessories of STM System

The accessories of STM system include an electrical control box, software, optical telescope, tip, vibration isolation table and vacuum chamber. We will simply present them here.

The electrical control system is commercial SPM 100 control system and control software XPM 2.0. Both of them are from RHK Technology Company. For this system, we choose high sensitive IVP-300 I/V Pre-amplifier which has $1*10^9$ gain, 5 KHz bandwidth, RMS noise 0.65 pA at 1.5 KHz and 100pF input capacitance and the minimum tunneling current 1pA [4]. This system is controlled by the RHK software XPM 2.0 and is connected to the chamber of STM.

For the STM tip the noble metals are chosen. A very common tip material is Pt-Ir, which is used in all of the experiments described in this thesis. Pt is a noble metal so it does not oxide when it exposed to oxygen/air and Ir is added to Pt to increase the stiffness of the tip and create a more stable tip. For most application, a Pt-Ir wire is cut with a wire cutter to form a tip. The tip which is cut with a wire cutter often has two tips on the top, as shown in Figure 2.7 (a). The Pt-Ir wire could also be etched to form a sharp tip or cut by focused ion beam (FIB), but we have not yet implemented these strategies for this experiment. Another metal which is usually used as STM tip is W which can be created as a sharp tip with an etch process. However, W oxidizes in air, so it is require complex in situ to remove the oxide layer in vacuum chamber. In our experiment, we use wire cutters to cut Pt-Ir wire to form a STM tip and carefully choose, via SEM inspection, in order to avoid double tips which can greatly complicate the measurement data. Figure 2.7(b) shows the tip which is used in our measurement.

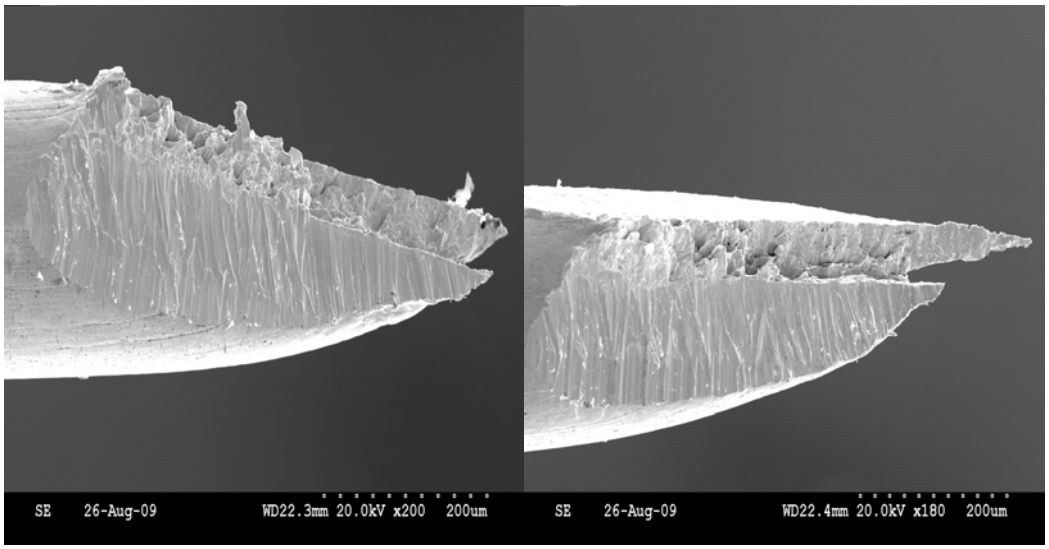

Figure 2.7 Pt-Ir STM Tip with 200μm scale bar. (a) Two tips close each other (b) Two tips with a big gap (preferred)

In order to avoid the air damping for MEMS device motion, the measurement is done in a high vacuum chamber whose pressure is lower than 10^{-6} torr. For this STM vacuum chamber, the turbopump and ion pump are used together in order to decrease the mechanical vibration noise. The turbo pump is used to pump roughly the chamber for high vacuum to about 10^{-5} torr, where the ion pump can start to work, and then ion pump is turned on to pump higher vacuum and to sustain the vacuum for measurement. A gate valve can then be closed and the turbo pump turned off, even removing the turbo pump connection to best mechanically isolate the chamber from the outside world. As we know the ion pump works quietly and does not make mechanical vibration noise like turbopump does. But the principle of the ion pump is that an ion pump ionizes gases and employs a strong electrical potential, typically 3 kV to 7 kV, to accelerate them into a solid electrode. Thus when the ion pump is working, unfortunately, it creates electrical noise. In our STM system, the ion pump makes a 70 KHz electrical noise in the tunneling current and this noise can be found from FFT current information of RHK system spectrum analyzer, as shown in Figure 2.8 (a). This noise can impact the sensitivity of the measurements.

Actually, in our measurement it has a small impact, because there are other noises, as shown in Figure 2.8 (b), which are dominant and will have the main impact on the sensitivity of the measurement

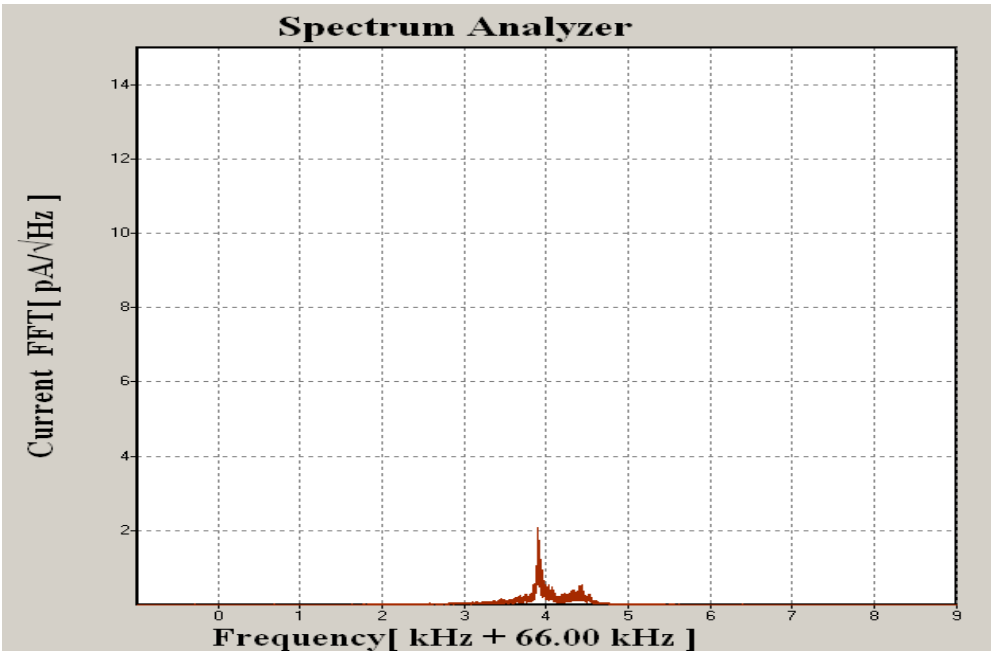

(a)

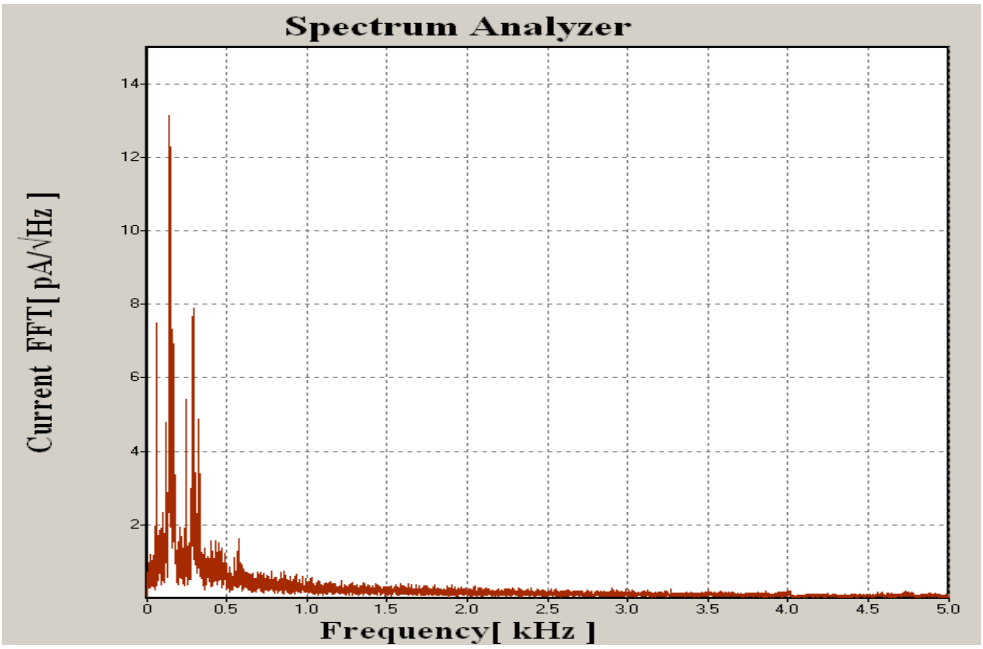

(b)

Figure 2.8 The spectrum of noise in STM system (a) The ion pump noise spectrum (b) Other noise spectrum

The mechanical noise will badly impact the sensitivity of STM system, because electron tunneling is sensitive to small distance changes. In order to further reduce the noise in the STM system, the STM vacuum chamber is put on a vibration isolation table (see Figure 2.10). This table will decrease the mechanical vibration effect from building, air flow and so on.

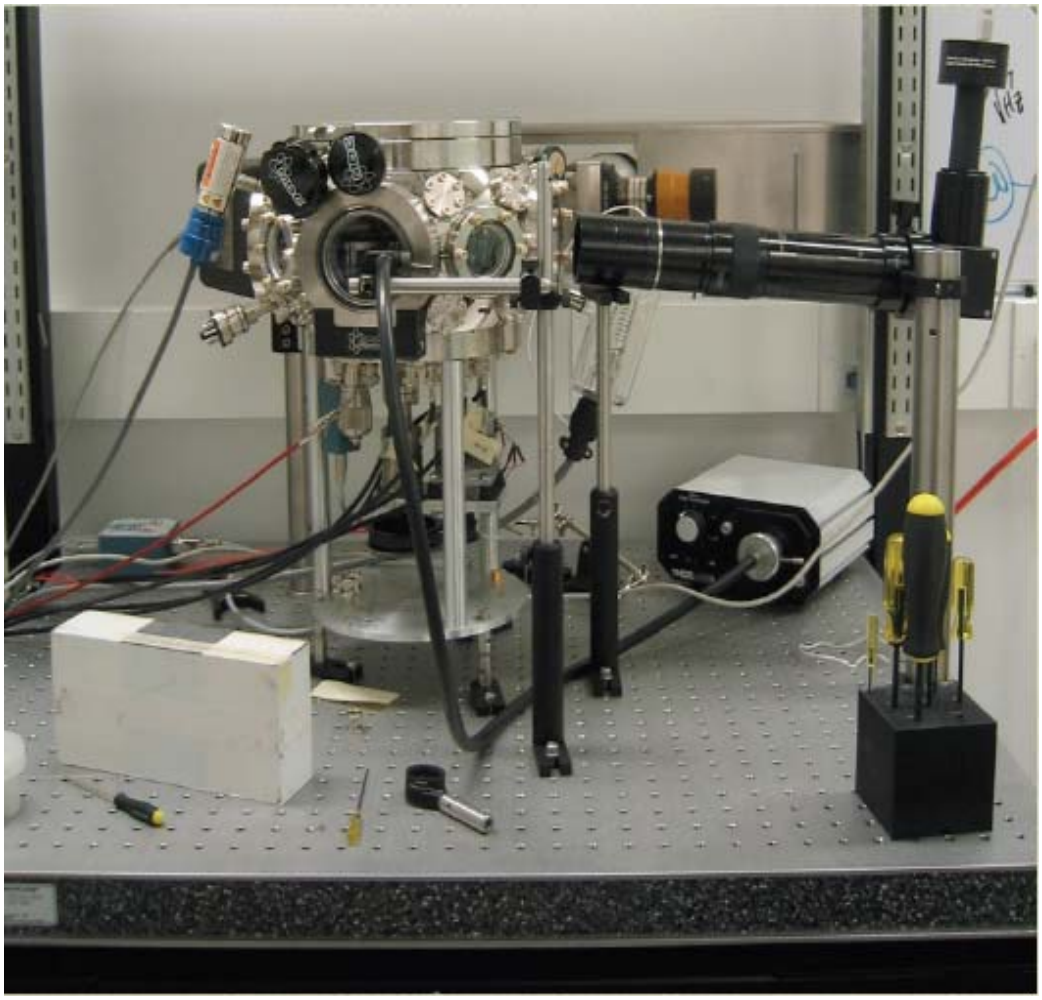

Figure 2.9 The image of STM system on vibration isolation

2.3 The Operation of STM

The electron tunneling only occurs when the tip is nearly 10 Å from the counterelectrode, so the gap between the electrodes must be controlled during the operation. This is usually accomplished by STM electronics, the control box SPM

100, which consist of three parts: the preamplifier, the feedback controller and the triple high voltage amplifier, as shown in Figure 2.10.

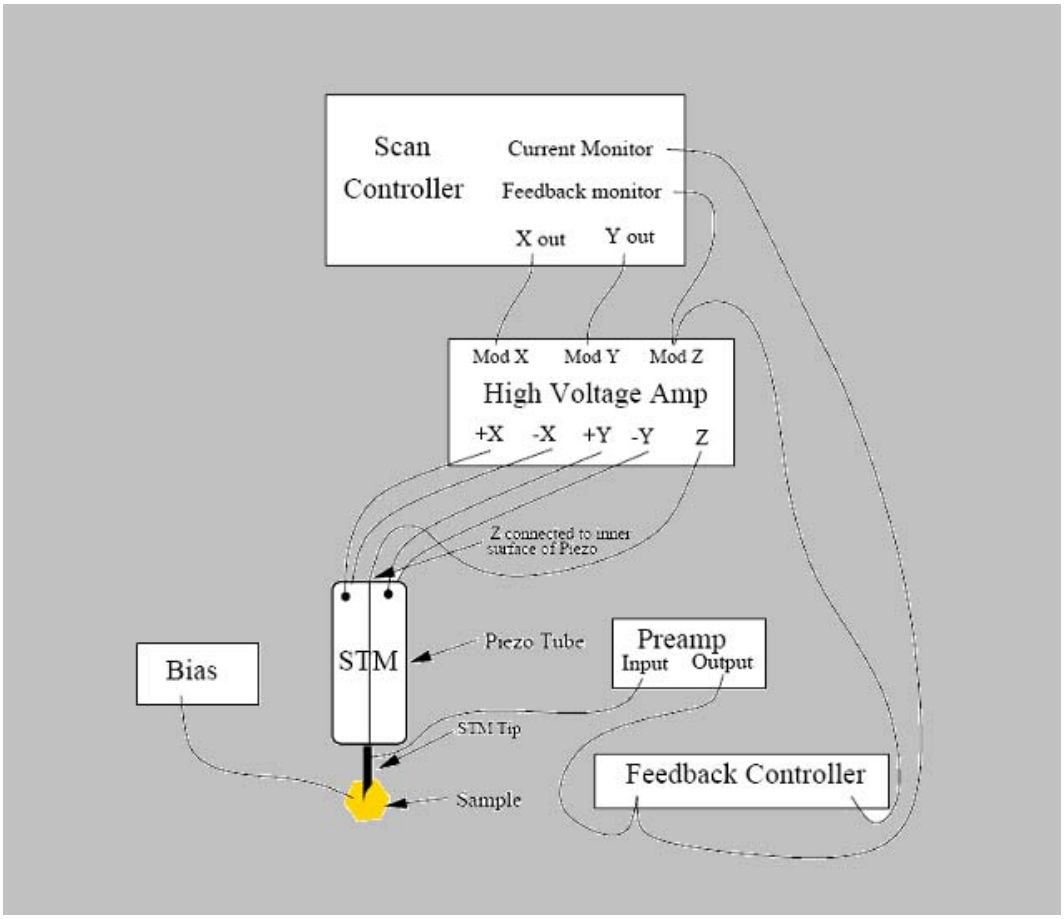

Figure 2.10 Basic element of a Scanning Tunneling Microscopy

Converting the tunneling current into a voltage to drive the feedback controller is the function of the preamplifier. The feedback loop compares the tunneling current to a setpoint and produces an error voltage proportional to the difference between these two signals. This error signal is amplified by the high voltage amplifier to drive the Z axis piezo to keep a constant average current. Thus the tip will stay a constant height over the sample. This error voltage also provides the topography information.

There are four adjustments on the feedback controller. These are the gain, time constant, DC tunneling current setpoint and DC bias voltage. The GAIN control

adjusts the gain of the feedback loop and should be set as high as possible without causing oscillation in the system. The time constant adjust changes the cutoff point of one pole lowpass filter that serves as the dominant pole of the feedback loop. DC tunneling current setpoint dial is used to set the compared tunneling current value. And DC bias voltage of the feedback controller provides the bias for the tunneling junction.

The triple amplifier is a high voltage (+/- 130V) amplifier used to amplify the signals from the STM electronics to a level that can drive the piezo assembly to move. The X Y and Z outputs drive the X Y and Z piezo of STM respectively. For the X and Y channel, the gain can be set in software according to the size scan desired. Also the X and Y offset dials on RHK control panel allow repositioning the scan area. For the Z channel the gain setting affects the feedback loop gain and should be set in conjugation with the feedback control gain and time constant to provide the maximum gain while maintaining loop stability.

Thus when STM is used as electron tunneling transducer for downmixing readout, these parameters, DC tunneling current, bias voltage, gain and time constant, should be carefully chosen to make the STM work stably. We will exploit the impact of these parameters on STM downmixing readout in detail.

REFERENCE

1. G. Binning, H. Rohrer, C. Gerber, and E. Weiber, Surface studies by scanning tunneling microscopy, *Phys. Rev. Lett.* 49, 57, (1982)

2. G. Binning, H. Rohrer, C. Gerber, and E. Weiber, 7x7 Reconstruction on Si(111) resolved in real space, *Phys. Rev. Lett.* 50, 120, (1983)

3. Bardeen, J., Tunneling from a many-particle point of view, *Phys. Rev. Lett.,* 1961, 6, 57

4. Technical brief published at http://www.rhk-tech.com

Chapter 3 Electron Tunneling Transducer Using Signal Downmixing Readout

In this chapter, we will present the configuration which we will use to measure the motion of NEMS. First, we will introduce the transducer based on electron tunneling. Secondly, the piezoelectric actuation which we will use in our experiment will be simply explained. Then we focus on the mathematical description of tunneling junction downmixing and the details of the downmixing scheme.

3.1 The introduction of electron tunneling transducer

The investigation of the ultimate quantum limits for the detection of weak forces has been stimulated by the development of nanoelectromechanical systems (NEMS). But for all the nanotechnology applications of NEMS devices, a significant challenge is figuring out a fast, low-noise technique for transferring small mechanical motion into reasonable electronic signals to measure. Electron tunneling is a promising method to measure the minute motion of NEMS, because the tunneling current is so sensitive to the change in distance and the fundamental limit, I_T/e, can reach the GHz. Also the transducer using electron tunneling is a nonreciprocity electromechanical transducer which has greatly reduced back action on the mechanical element being monitored and may reach the quantum limit for a measurement of the position of a mechanical oscillator even with use of a non-quantum-limited amplifier [1, 2].

Simply the tunneling transducer is a variable resistance transducer, such as a scanning tunneling microscope (STM), held close to the sample to monitor the fluctuation. The motion of a NEMS device modulates the gap of a tunnel junction between the tip and the NEMS device and thus will modulate the tunneling probability. When the junction is biased with a constant voltage, the current measured by an amplifier which follows the tunnel probe provides a sensitive

measure of the tunneling gap and therefore of the displacement of the NEMS device, as shown in Figure 1.8.

When the gap between the probe tip and NEMS device is small enough, the tunnel junction is formed and an electron can tunnel through the energy barrier from one side to the other with a finite probability based on the tunneling quantum mechanical effect. As shown in Figure 3.1 the tunneling current I through the junction is related to the dc bias V and the tunnel gap x and can be written as [3]:

$$I = \rho_s(E_F)Ve^{-2kx} \tag{3.1}$$

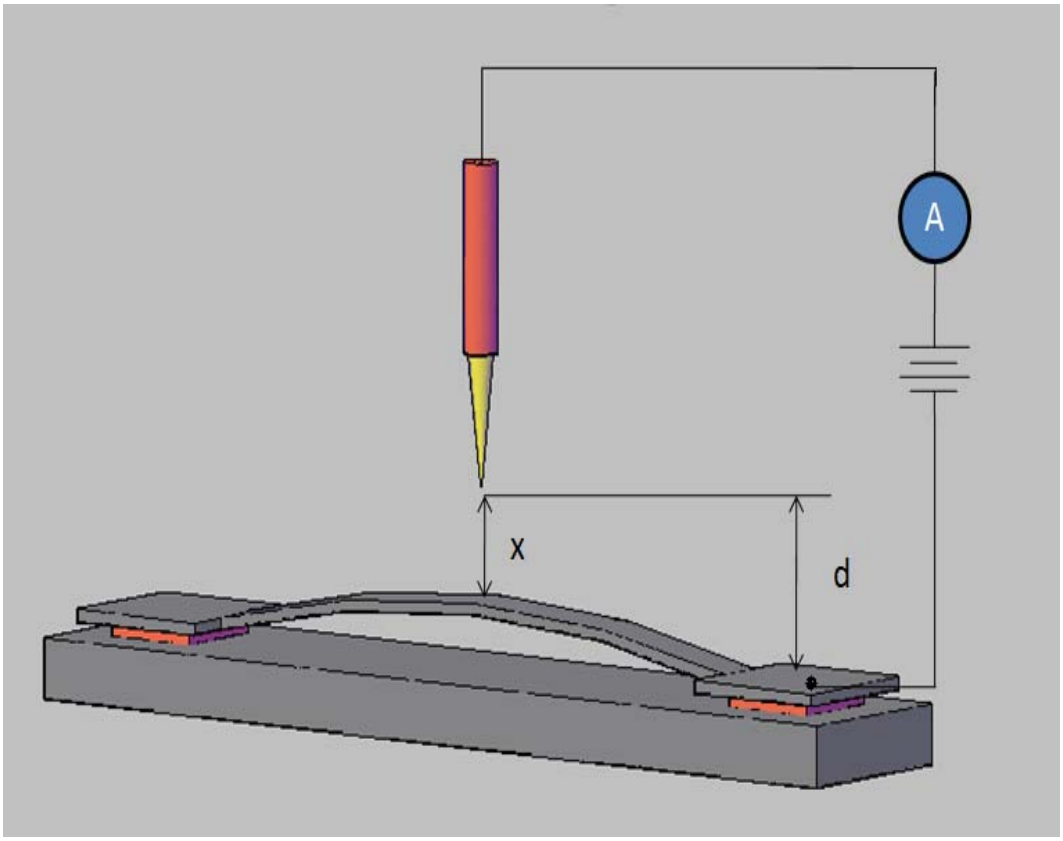

Figure 3.1 Scheme for the detection of displacement through an electron tunneling transducer. The static separation between the NEMS device and the tip is d and the displacement of the NEMS device is (d-x).

Here $\rho_s(E_F)$ is the local density of electronic states in the NEMS device which can be assumed to be voltage-independent and κ is the decay constant for electron wave-function within the gap, $\kappa = \sqrt{2m_e\Phi}/\hbar$, here m_e is the mass of electron, Φ is the work function of the metal and ħ is Planck's constant divided by 2π. The typical value of κ is about 1.15Å^{-1} for gold where the gold work function is about 5.4eV.

Based on the exponential dependence of tunneling current on the electron tunneling gap and the decay constant $\kappa \approx 1.15$Å^{-1}, it is clear that the tunneling transducer will be very sensitive to the motion of the sample. Let us suppose that an electronic circuit is capable of detecting 1% variation in a 1 nA current, then the distance can be calculated as following:

$$\partial x = \frac{\partial I}{2\kappa I} \approx 0.004\ \text{Å}$$

To represent the tunneling transducer easily, we convert the various noises in the measurement into a limiting displacement floor [4]:

$$[S_x(\omega)]^{1/2} = \left(\frac{S_I^{(A)}(\omega)}{4\kappa^2 I^2} + \frac{e}{2\kappa^2 I} + \frac{S_F^{(BA)}}{m_{eff}^2\left((\omega_0^2-\omega^2)^2 + \frac{\omega^2\omega_0^2}{Q^2}\right)}\right)^{1/2} \qquad (3.2)$$

the first term on the right hand side represent the equivalent current noise of the current amplifier – usually in the range $S_I^{1/2} \approx 10^{-13}$ A Hz$^{-1/2}$ and this current noise of the current amplifier can be decreased by the design of current amplifier. The second term arises from current noise. The spectral density of the current noise is the usual expression for shot noise plus the Johnson-Nyquist noise of the tunneling current,

$$S_i = 2eI + 4\kappa_b T / R \qquad (3.3)$$

The shot noise dominates the Johnson-Nyquist noise when DC bias voltage between the tip and sample $V > 2\kappa_b T / e = 51$ mV at 300K. So here the John-Nyquist noise is omitted. For a typical tunneling current of 1 nA, the spectral density of shot noise is $[S_I^{(s)}]^{1/2} \approx 10^{-14}$ A Hz $^{-1/2}$.

The character of the backaction force noise in a tunneling transducer has been researched. The spectrum of the force fluctuations is the white noise with a spectral density given by

$$S_F^{(BA)} \approx (\frac{p}{e})^2 2eI + (\hbar\kappa)^2 \frac{I}{e} \qquad (3.4)$$

The first term is that an electron which tunnels from the probe to the mechanical oscillator carries momentum and this creates a force, f = pi/e, where p is the momentum of tunneling electron and i/e is the tunneling rate, on mechanical oscillator. This term is completely correlated with the shot noise current fluctuations of the transducer and the spectral density can be written as $(p/e)^2 2eI$. The second term which is independent of the shot noise is the fluctuation of the momentum current from the tip to the test mass. This arises from the intrinsic uncertainty of the momentum of each electron which tunnels. For the tunneling electron the position uncertainty is $\triangle x \approx d \approx 1/\kappa$. Then the momentum uncertainty can be written as $\triangle p \approx \hbar/\triangle x \approx \hbar\kappa$. The variance (or the fluctuation in the force) is $\triangle f \quad (\hbar\kappa)I/e$ – given that force is the temporal rate of change of impulse. The spectral density of this noise can be gotten by $(\triangle f)^2$ dividing the effective bandwidth $\triangle\omega \approx I/e$ and can be written as $((\hbar\kappa)^2 I/e$. Thus for a tunnel current about 1 nA and $\kappa \approx 1.15 Å^{-1}$, $[S_F^{(BA)}] \approx 10^{-18}$NHz $^{-1/2}$.

Thus we can calculate the displacement measurement sensitivity of electron transduction based on the above the discussion. The force noise is small and here we can omit it. In our experiment the IVP-300 preamplifier is used and the current

noise of the amplifier is about $10^{-14}AHz^{-1/2}$ according to RHK preamplifier specifications. The noises come mainly come from noise current of the amplifier and the shot noise. Assuming the tunneling current 1nA and $\kappa \approx 1.15Å^{-1}$, the displacement measurement sensitivity is about $4.3fm/Hz^{1/2}$.

From these we know that tunneling transducers can have an exquisitely low noise floor and are sensitive to the minute motion of NEMS devices.

In addition, it is especially important to note that the displacement responsivity of the tunneling transducer is not directly dependent on the dimensions of the transducer. As a result, the tunneling transducer can be miniaturized without loss of displacement resolution. This development creates an opportunity for a broad class of sensor without loss of performance and can be used for ever smaller NEMS device detection.

3.2 Device Actuation

Inducing motion of very small structures has been demonstrated with a variety of techniques, including magnetomotive technique [5], electrostatic (capacitive) actuation technique [6], photothermal technique [7], and piezoelectric actuation technique [8]. There are also other techniques which will be used for NEMS actuation.

In our project, piezoelectric actuation was chosen to drive the resonators in their resonant mode. As we know, some materials have the ability to generate an electric potential in response to applied mechanical stress. This is called the piezoelectric effect. The piezoelectric effect is reversible and this means a piezoelectric material can convert electrical energy into a mechanical displacement or stress. One can use this effect to make piezoelectric actuator, as shown in Figure 3.2.

When the piezoelectric materials are used for actuator, the flat region of the frequency response plot, as shown the yellow area of Figure 3.3 is typically used.

In this region, the relationship of the applied voltage and force is linear and can be written as:

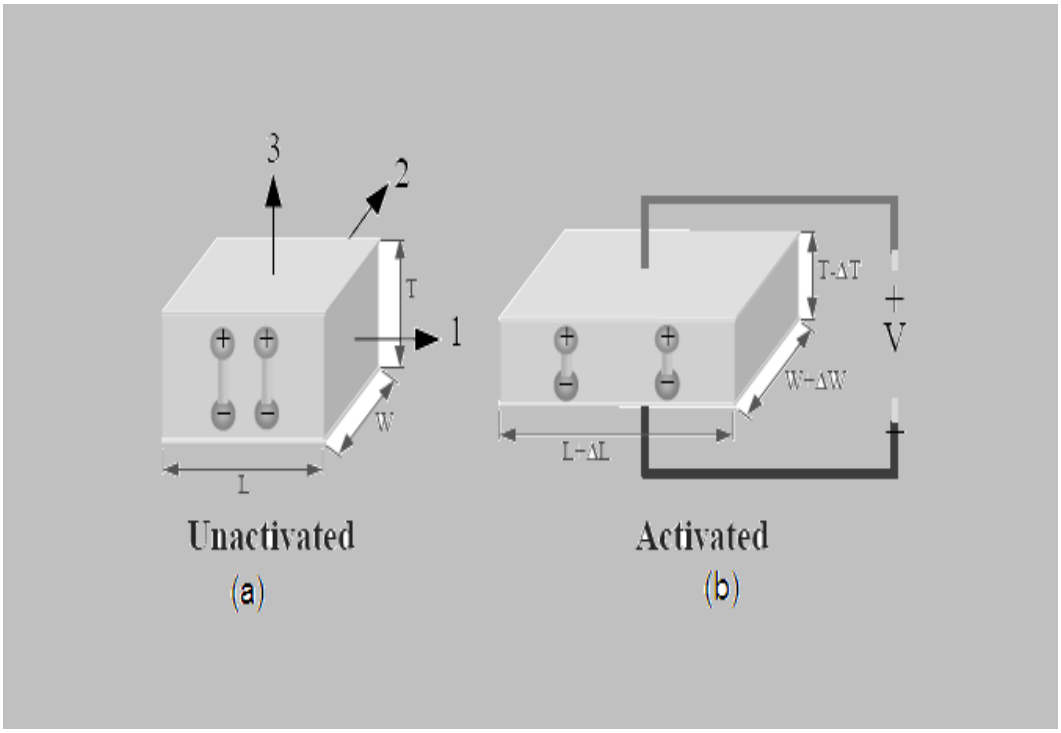

Figure 3.2 Motion of Piezoelectric Material

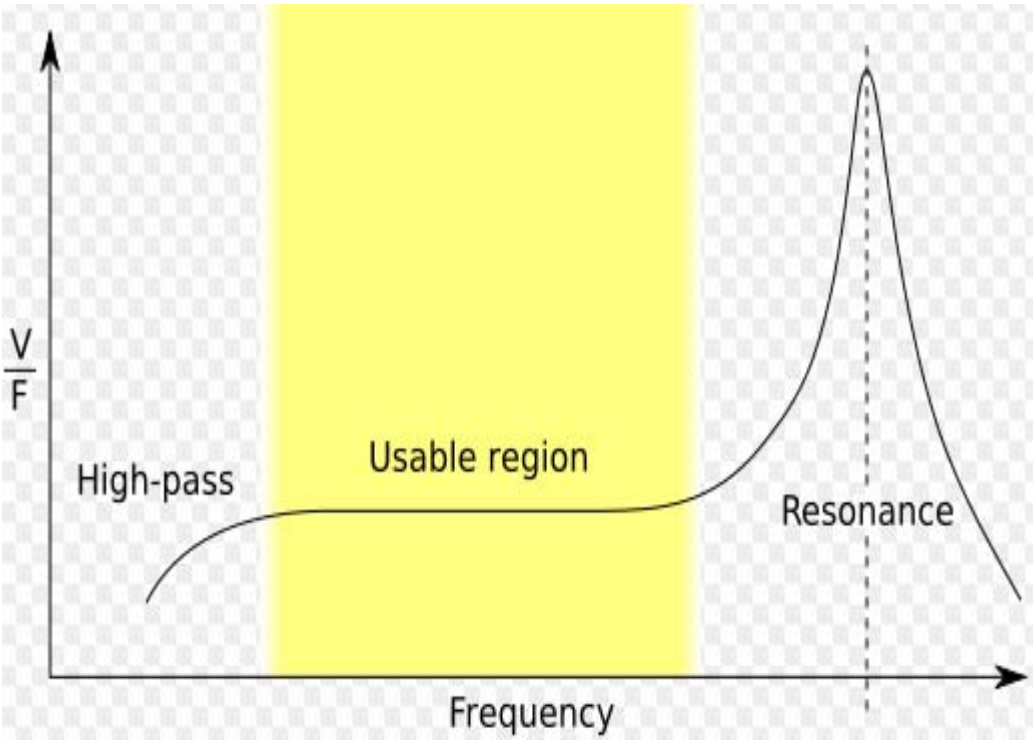

Figure 3.3 Piezoelectric Material Frequency Responses

$$F = KV \tag{3.5}$$

Here K is constant a factor which is related to the material properties and direction. In ideal situation, this region is used to actuate NEMS device. But for real piezo disc, there are several resonance frequencies. When we use the piezo disc to drive MEMS device, the flat region is chosen. Thus the actuation force coming from piezo disc is related to the voltage which is applied to the piezo disc. When an ac voltage, $V = V_{ac}\cos(\omega t)$, is applied to the piezo disc, the actuation force coming from the piezo disc can be written as:

$$F = KV_{ac}\cos(\omega t) = F_0\cos(\omega t) \tag{3.6}$$

When this force is applied to the NEMs device, it will induce the vibration of NEMs. The vibration amplitude of NEMS device can be written as:

$$a_m = \frac{1}{\rho A \ell^3} \frac{F_{ext}}{\omega_m^2 - \omega_c^2 - i\omega_m / Q} \int_0^\ell u_m(x)dx \tag{3.7}$$

And then we put Equation (3.6) into Equation (3.7) and get:

$$a_m = [\frac{1}{\rho A \ell^3} \frac{F_0}{\omega_m^2 - \omega_c^2 - i\omega_m^2 / Q} \int_0^\ell u_m(x)dx]\cos(\omega_c t) \tag{3.8}$$

Here we let $d_0 = \frac{1}{\rho A \ell^3} \frac{F_0}{\omega_m^2 - \omega_c^2 - i\omega_m / Q} \int_0^\ell u_m(x)dx$ and it depends on the material, resonance frequency and actuating force coming from piezo disc. It should be constant for one resonance mode at the constant force. Thus in order to be convenient for the following deduction, the vibration amplitude of NEMS can be written as:

$$a_m = d_0 \cos(\omega_c t) \tag{3.9}$$

This equation about the vibration amplitude of NEMS will be used in the following discussion. Its value depends on the resonant mode, material properties, actuating force and actuating force frequency.

3.3 Mathematical Description of STM Tunneling Junction Downmixing

We have presented some advantages of the electron tunneling transducer, but the useful bandwidth of tunneling transduction is limited by the stray capacitance in macroscopic wiring (discussed in an earlier chapter). In order to overcome this obstacle, a NEMS system with the electron tunneling transducer and piezoelectric actuator can be setup, as shown in the Figure 3.4. Combining the tunneling current equation (3.1) and the vibration of the piezo disc equation (3.9), the tunneling current of Figure 3.4 can be written as:

$$i = \rho_s(E_F)V_{ac1}\cos(\omega_1 t)e^{-2\kappa(d-d_0\cos(\omega_2 t+\Phi))}$$
$$\Rightarrow i = \rho_s(E_F)V_{ac1}\cos(\omega_1 t)e^{-2\kappa d}e^{2kd_0\cos(\omega_2 t+\Phi)} \quad (3.10)$$

The Taylor series for the exponential function e^x at 0 can be written as:

$$e^x = 1+\frac{x^1}{1!}+\frac{x^2}{2!}+\frac{x^3}{3!}+\ldots = 1+x+\frac{x^2}{2}+\frac{x^3}{6}+\ldots \quad (3.11)$$

Using the Taylor series to replace the exponential item of equation (3.10), we can rewrite the tunneling current as the following:

$$i = \rho_s(E_F)V_{ac1}\cos(\omega_1 t)e^{-2\kappa d}\left[1+(2kd_0\cos(\omega_2 t+\Phi))+\frac{(2kd_0\cos(\omega_2 t+\Phi)^2}{2}+\ldots\right] \quad (3.12)$$

Because the higher power items have higher frequency information and are unuseful for our experiment, we can omit the quadratic and higher power items of equation (3.12) and get:

$$i = \rho_s(E_F)e^{-2\kappa d}V_{ac1}\cos(\omega_1 t)(1+2kd_0\cos(\omega_2 t+\Phi)) \quad (3.13)$$

Here one needs to use the sum and difference formulas of trigonometric function.

$$\cos(x+y) = \cos x\cos y - \sin x\sin y$$
$$\cos(x-y) = \cos x\cos y + \sin x\sin y \quad (3.14)$$

According to the equation (3.14), we can get the relationship:

$$\cos x\cos y = \frac{1}{2}(\cos(x+y)+\cos(x-y)) \quad (3.15)$$

Based on the equation (3.15), the equation (3.13) can be rewritten as:

$$i = \rho_s(E_F)e^{-2\kappa d}V_{ac1}[\cos(\omega_1 t) + kd_0\cos((\omega_1+\omega_2)t+\Phi) + kd_0\cos((\omega_1-\omega_2)t+\Phi)] \quad (3.16)$$

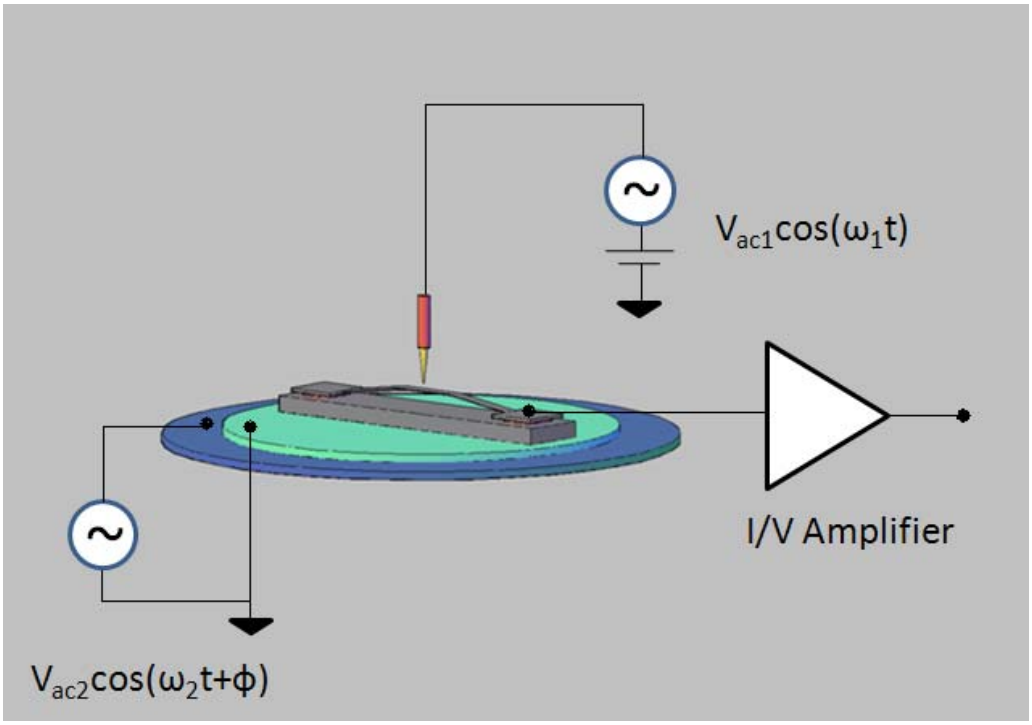

Figure 3.4 The scheme of downmixing which integrates electron tunneling transducer and piezoelectric actuator

From the equation (3.16), one can figure out that the tunneling current includes three different frequency signals when we omit the quadratic or higher order terms of the equation. The frequency information of tunneling current is displayed in Figure 3.5.

Figure 3.5 Information of Tunneling Current in Frequency Domain

Thus when we have two high frequencies which are close to each other, these two high frequencies can be down mixed when they pass through the STM tunneling junction. As the result the difference of two high frequencies can be seen at the tunneling current output. One can easily readout the information with normal STM and improve the ability to readout high frequency information with STM. This allows an electron tunneling transducer to detect the motion of high frequency NEMS devices.

3.4 Configurations of Tunneling Junction Frequency Downmixing

In order to transfer the high frequency to low frequency to detect, we design the STM downmixing electric circuit as shown in Figure 3.6 based on the derivation of the above discussion. We will analyze this scheme in detail in this section.

In the scheme, the ac power supply is the signal generator, Agilent N9310A, which has a sweep frequency function. A sweeping frequency signal which is generated by the signal generator is sent to the power splitter to divide into two same power and frequency signals.

One of them is directly sent to the piezo disc. Due to reversible piezoelectric effect, a mechanical force will be created and this force will drive the NEMS

device into motion. The amplitude of NEMS device vibration can be expressed as equation (3.9). But the motion of NEMS is not necessarily in phase with the force which is created by the piezo disc due to response time and other complex factors.

Another signal is sent to the STM tip through a single sideband mixer, SSB 05-15-3K-6K, and Bias Tee. At the single sideband mixer this signal will mix with a low frequency signal which comes from the Lock-in amplifier reference output and which frequency is located within the STM bandwidth. This low frequency can be chosen as long as it retains within the STM bandwidth. Here we can choose a frequency based on the noise floor in order to improve the sensitivity of detection. At the output of the mixer, two signals are produced with 10dB power difference - one higher sideband frequency and the other lower sideband frequency, which one is the higher power be chosen. For purposes of this argument, the lower power signal can be assumed to be negligible. Then this signal will pass a bias tee to combine with a DC voltage. Here the function of bias tee is to combine the high frequency and DC without the high frequency signal reaching the DC electronic output or the DC signal loading mixer, lock-in, or ac source output. After that this combined signal is applied to the STM tip. At the tunneling junction, the two signals which are divided by the power splitter meet together. Due to the mixing function of tunneling junction, these two signals are mixed and follow the downmixing rule which is described in Equation (3.16) to create three different frequencies. And then this downmixing signal will be amplified by I/V amplifier, RHK IVP-300, and send to the Lock in amplifier, SR 810. As we mentioned in Chapter 1, due to the stray capacitance in macroscopic wiring between the NEMS device and I/V amplifier and the high capacitance of the amplifier itself, the high frequencies will be cutoff. Thus at the output of I/V amplifier, all that remains is the low frequency information which consist of a signal precisely at the reference frequency of the Lock-in amplifier, a DC tunneling current signal, and noise. In the Lock-in Amplifier the downmixing signal will be picked out since its frequency is same as the reference signal frequency. This signal carries the information about the high frequency dynamical

MEMS motion. At the same time, the feedback system maintains in constant current mode, with response to some averaged position of the resonator.

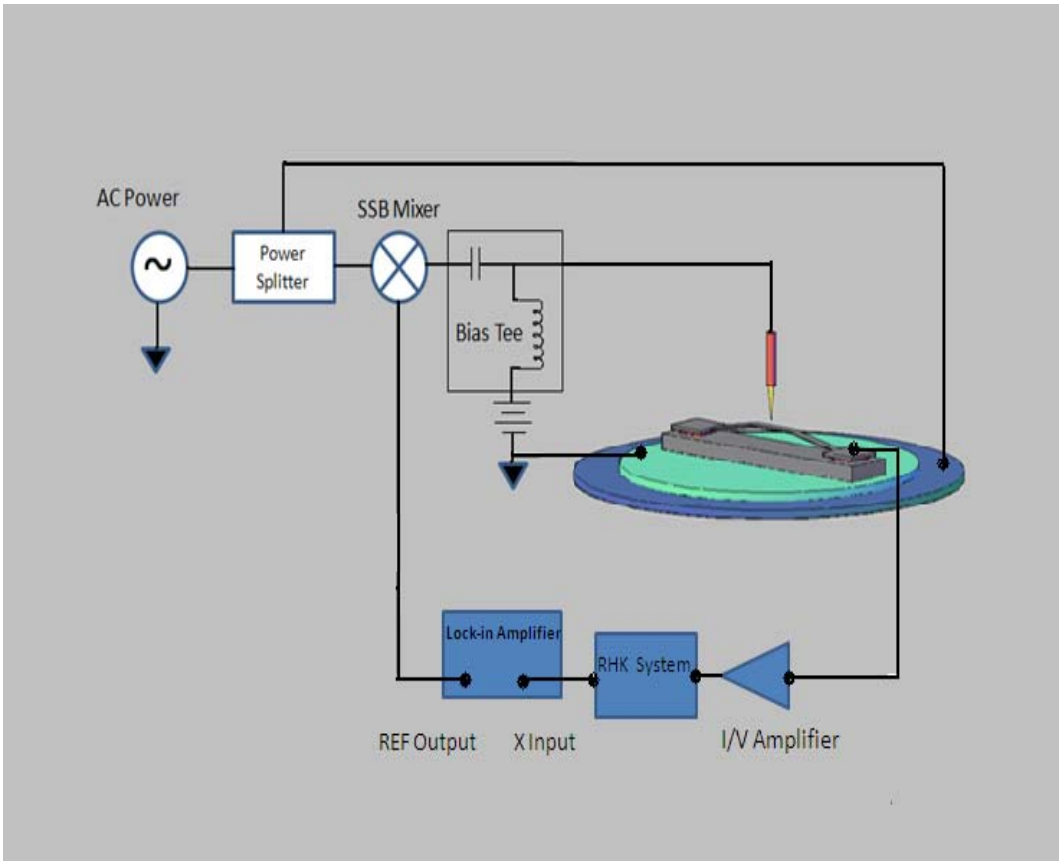

Figure 3.6 Figure 3.6 STM frequency downmixing readout scheme

Now let us explore the phase information of the downmixed result in this electric scheme.

Assume that the signal from the signal generator is:

$$V = V_s \sin(\omega_s t) \tag{3.17}$$

And the signal from the Lock-in amplifier is:

$$V_{downmixing} = V_r \sin(\omega_r t) \tag{3.18}$$

Here the phase different is based on the Lock-in amplifier, the phase difference between the signal from signal generator and the signal from lock-in amplifier is assumed θ_1. When the single sideband mixer is used and we choose the higher sideband, the output of the mixer can be written as:

$$V_{output} = -\frac{1}{2} Vs * V_r \cos[(\omega_r + \omega_s)t + \theta_1] \tag{3.19}$$

When the piezo disc actuates the MEMS, the motion of NEMS is not necessarily in phase with the force due to response time and other complex factors. We can set this phase difference to be θ_2. Thus based on Equation (3.9), the vibration of MEMS can be written as:

$$d_{MEMS} = a_m \sin(\omega_s t + \theta_1 + \theta_2) \tag{3.20}$$

Here $a_m = \frac{1}{\rho A \ell^3} \frac{F_{ext}}{\omega_m^2 - \omega_c^2 - i\omega_m^2 / Q} \int_0^\ell u_m(x) dx$ is the amplitude of NEMS at actuating force F_{ext} and F_{ext} is related to the voltage applied to piezo disc.

For STM, when the bias voltage is far less than the Fermi energy of the metal the tunneling current can be written as:

$$\begin{aligned} & I \propto (V_{bias} + V(\omega)) e^{-2k(d + d_{MEMS})} \\ & \Rightarrow I \propto (V_{bias} + V(\omega)) e^{-2kd} e^{-2kd_{MEMS}} \\ & \Rightarrow I \propto (V_{bias} - \frac{1}{2} V_s * V_r \cos[(\omega_r + \omega_s)t + \theta_1]) e^{-2k(d + d_{MEMS})} \end{aligned} \tag{3.21}$$

Here $k = 0.51 * \sqrt{\phi(eV)}\ ^{\circ -1}A$. For Au □=1.185Å^{-1}.

Use Taylor:

$$e^x = 1 + x + \frac{1}{2!}x^2 + \frac{1}{3!}x^3 + \ldots$$

$$\sin\alpha\cos\beta = \frac{1}{2}[\sin(\alpha+\beta) + \sin(\alpha-\beta)]$$

$$\sin\alpha\sin\beta = -\frac{1}{2}[\cos(\alpha+\beta) - \cos(\alpha-\beta)]$$

$$I \propto (V_{bias} - \frac{1}{2}V_s V_r \cos[(\omega_s+\omega_r)t+\theta_1])e^{-2kd}[1-2ka_m \sin(\omega_s t+\theta_1+\theta_2)+\ldots] \tag{3.22}$$

When we omit high frequency items and just keep reference frequency items, we obtain:

$$I \propto V_{bias}e^{-2kd} + V_s V_r e^{-2kd} ka_m \sin(\omega_r t - \theta_2) \tag{3.23}$$

Thus, when we use Lock-in Amplifier to measure tunneling current of STM, we can get the amplitude of NEMS motion and the phase information of NEMS motion which is related to initial condition θ_2. For harmonic vibration, the phase sweep through 180 degree when resonance happens. This phase change can also be measured with the STM downmixing readout method.

REFERENCES

1. Bocko, M. F., and Stephenson K. A., Vacuum Tunneling Probe: A Nonreciprocal, Reduced-Back-Action Transducer, *Phys. Rev. Lett.*, 61, 726, (1988)

2. Bocko, M. F., and Stephenson K. A., Tunneling transducers: Quantum limited displacement monitors at the nanometer scale, J. Vac. Sci. B, 9, 1363, (1990)

3. Tersoff, J., Scanning Probe Microscopy and Spectroscopy (Ed.: Bonnell, D.), Wieley, New York, 2000

4. Ekinci, K. L., Electromechanical Transducers at the Nanoscale: Actuation and Sensing of Motion in Nanoelectromechanical Systems (NEMS), *Small*, 8, 786, (2005)

5. Cleland, A. N., and Roukes, M. L., Fabrication of high frequency nanometer scale mechanical resonators from bulk Si crystal, *Appl. Phys. Lett.*, 69, 2653, (1996)

6. Tilmans, H. A., and Legtenberg, R., Electrostatically driven vacuum-encapsulated ploysilicon resonators, *Sens. Actuators A,* 45, 67, (1994)

7. Koenig, D. R., Metzger, C., Camerer, S. and Kotthaus, J. P., Non-linear operation of nanomechanical systems combining photothermal excitation and magneto-motive detection, *Nanotechnology*, 17, 5260, (2006)

8. Masmanidis, S. C., Karabalin, R. B., Valminck, I. D., Borghs, G. Freeman, M. F and Roukes, M. L., Multifunctional Nanomechanical Systems via Tunably Coupled Piezoelectric Actuation, *Science*, 317, 780, (2007)

Chapter 4 STM Downmixing Readout of MEMS Motions

We measure the motion of a MEMS device with tunneling junction downmixing which is described in chapter 3. In order to make sure that the method of tunneling junction downmixing works well, we compare the results that we

measured using STM downmixing with the simulation using COMSOL and the result using optical interferometry [1] for the same device. At the last part of this chapter, we explore some parameters that impact STM downmixing result and the displacement measurement sensitivity with STM downmixing method.

4.1. The MEMS Sample Setup

In our experiment MEMS size devices were chosen solely for ease of telescopic optical alignment of the tunneling tip on the top of individual device structures. The individual structures are silicon doubly-clamped beam and are fabricated with the top-down approach process flow which is described in Chapter 1.5. These doubly-clamped beams have same width, 100 μm, the thickness, 5 μm and different length from 500μm to 2000μm with 150 μm steps. The schematic of the device is shown in Figure 4.1.

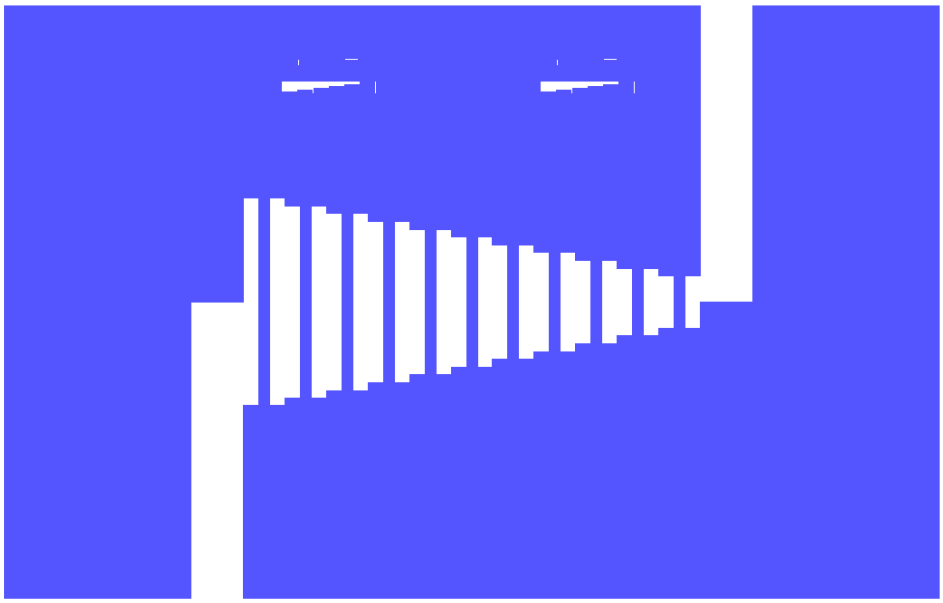

Figure 4.1 Schematic of the doubly-clamped beam

This doubly-clamped beam chip is mounted on a commercial piezo disc which is used as an actuator to drive the doubly-clamped beam during the measurement. The piezo disc and chip are bonded to a special designed printed circuit board (PCB). After these some wire bonding and solders are required to connect

different components together. In particular, the top surface of the piezo disc is grounded to try to minimize electrical cross-talk reaching the chip, while the bottom surface is excited with RF. The tunneling current that leaves the STM tip will travel through the Au surface on the MEMS beams, down the parallel wire bonds to the PCB trace, and be controlled as the tunneling signal. The final sample is shown in Figure 4.2.

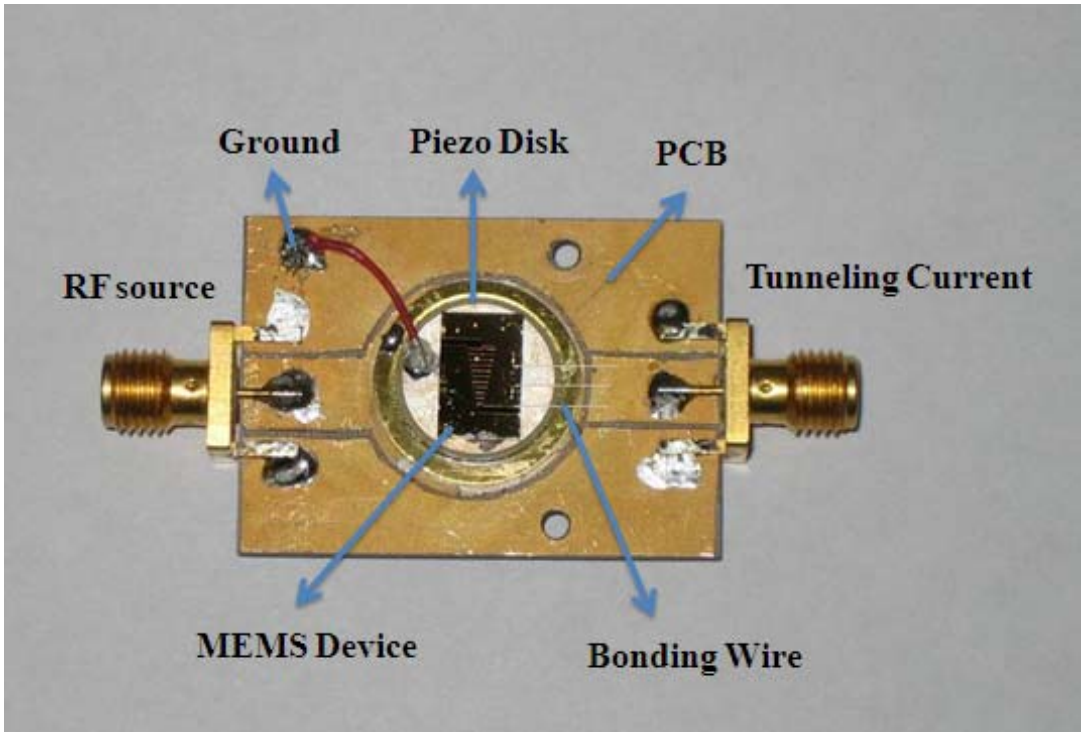

Figure 4.2 The sample of STM downmixing readout. Here MEMS device and the piezo disc which is used to actuate the MEMS device are mounted on the PCB together

This sample is mounted to the sample holder of the STM and put into the vacuum chamber which is introduced in Chapter 2. During measurement the chamber is pumped down to less than 10^{-6} torr.

4.2. The Proof of STM Tunneling Junction Downmixing

Since it is a new method that uses STM as a transducer and frequency downmixing in tunneling junction to readout the motion of MEMS, it requires validation. In order to validate that the STM downmixing is working well, we set up the electric circuits as shown in Figure 3.6 to measure a 500 μm long, 100 μm wide, and 5 μm thick doubly-clamped beam.

The signal generator sends a sine function signal at +13dBm power which sweeps the frequency around the doubly-clamped beam resonance frequency. From the reference output of the Lock-in amplifier a 4.5 kHz sin function signal is sent with 0.35 V_{rms}. Here we choose the 4.5 kHz signal based on two reasons: one is that the bandwidth of the I/V amplifier, IVP-300, is 5 kHz. Another reason is that this frequency area has a lower noise compared to other areas as shown from Figure 2.7 (b). And then we use the spectrum analyzer feature of RHK system software to observe spectral content of the output tunneling current of the STM in order to identify frequency downmixed information.

Figure 4.3 shows the information of downmixed tunneling current of the STM using the electric scheme of Figure 3.6. From RHK system software spectrum analyzer output figures, we can see that the reference frequency amplitude changes as the MEMS device actuating frequency changes. Figure 4.3 (a) shows the downmixed tunneling current FFT far from the resonance frequency of the MEMS device. The downmixed tunneling current amplitude at the reference frequency (4.5 kHz) is very small and is close to the noise floor, so we hardly see it. When we make the frequency of signal generator close to the resonance frequency of the MEMS device, the downmixed tunneling current FFT is shown in Figure 4.3 (b), (c) and (d). From these figures we can see that the amplitude at the reference frequency increases substantially with the sweep frequency close to the resonance frequency. In particular, Figure 4.3 (c) shows the FFT when the drive frequency is closest to the MEMS mechanical resonance frequency. Here, the vibration amplitude is maximum and this causes the downmixed tunneling current to be maximum and largest amplitude at the reference frequency. This show that the STM downmixing is working well and coinciding with the theory

prediction, because the vibration amplitude becomes biggest at the resonance frequency of the NEMS device and this causes the gap between the tip of the STM and the surface of NEMS to decrease and the tunneling current to increase.

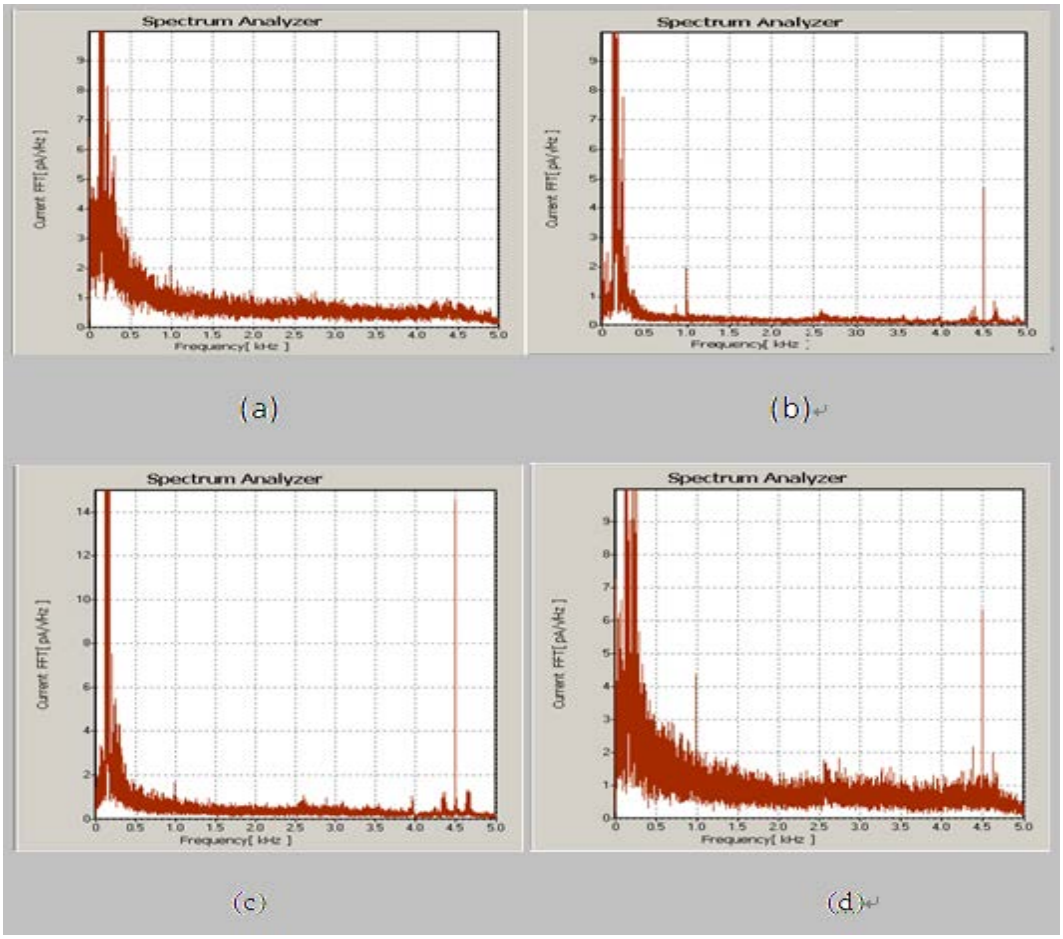

Figure 4.3 The Downmixing Tunneling Current Information from a spectrum analyzer. (a) Drive frequency far from mechanical resonance frequency. (b) and (d) Drive frequency close to the mechanical resonance frequency. (c) Drive frequency closest to the mechanical resonance frequency

Figure 4.4 shows the current FFT information of spectrum analyzer when the drive frequency is close to the mechanical resonance frequency. Here we can see that there are some sidebands around the reference frequency, as shown in Figure 4.4 (b). These sidebands are the results that electrical and mechanical noises (as

shown in Figure 4.4 (b)) mix with the reference frequency in tunneling junction. These also prove the mixing function of tunneling junction.

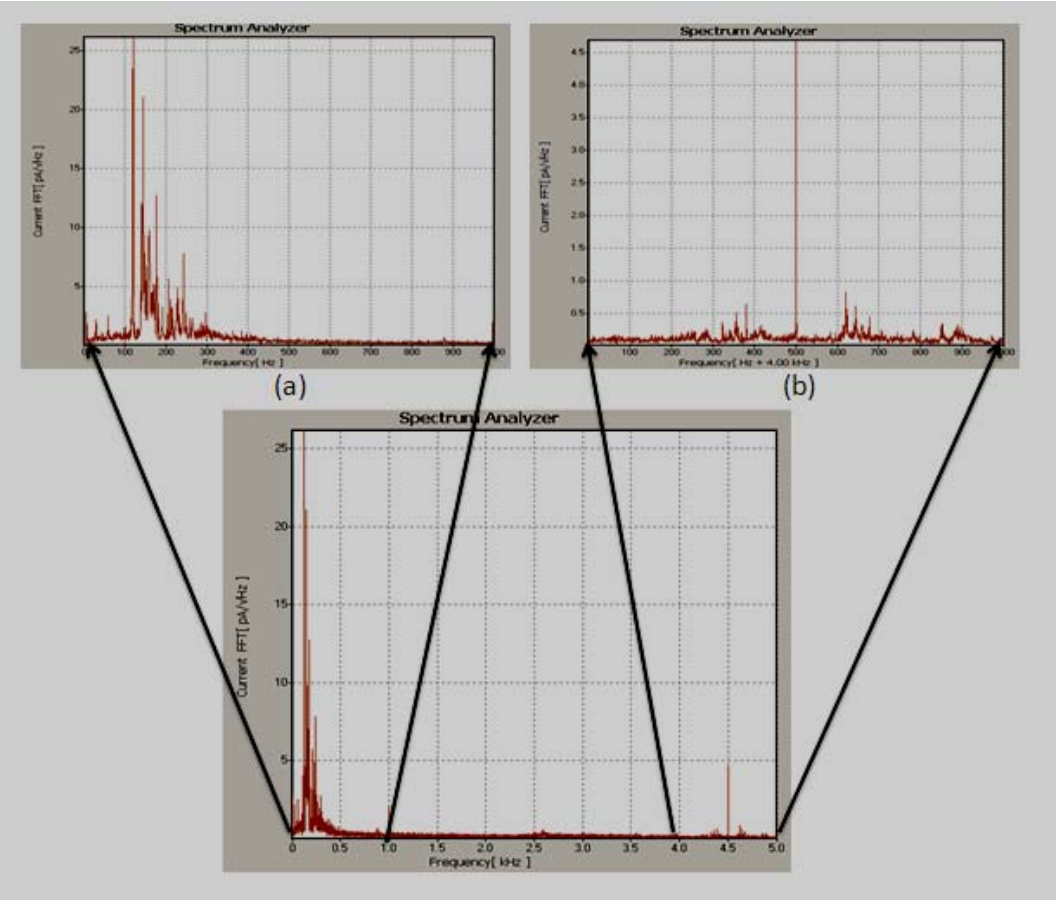

Figure 4.4 The downmixed tunneling current sideband information. Inset graph (a) Electrical and mechanical noise current FFT (b) Reference frequency with sidebands current FFT

Thus we can utilize this method to measure the downmixed tunneling current of reference frequency and get the high frequency information about NEMS vibration. The limit of STM bandwidth is overcome and this makes possible electron tunneling transduction as the detection of MEMS motion, even NEMS motion.

4.3. The Result of STM Downmixing Readout

In order to further validate the STM downmixing readout of electron tunneling transduction, we use the COMSOL software to simulate the eigenfrequency of the doubly-clamped beam and utilize optical interferometry to prove these eigenfrequencies. We then measure the same device with STM downmixing method and compare the results with the simulation and optical interferometry measurement.

4.3.1 Simulation Result of the Doubly-clamped Beam

COMSOL as a finite element simulation software can be used to simulate well the MEMS device. Here we use COMSOL to simulate the eigenfrequency of our double layer doubly-clamped beam. During our simulation the double layers and undercut which is caused by the wet etching are taken into account. The results of eigenfrequency simulation for a 500μm long, 100 μm wide and 5μm thick doubly-clamped beam with double layers - Cr 20 nm and Au 200 nm - and undercut is shown in Table 4.1 and the Figure 4.5 shows the mode shape of COSMOL simulation.

Table 4.1 COMSOL Simulation Result for a long 500 μm, wide 100μm and thick 5μm Silicon Doubly-clamped Beam with Au and Cr Metal Layers

Vibration Mode	First Flexural Mode	Second Flexural Mode	First Torsion Mode	Third Flexural Mode	Second Torsion Mode	Forth Flexural Mode
Resonance Frequency (kHz)	112.801	305.867	447.971	589.216	909.188	954.073

The simulation results in Table 4.1 and Figure 4.5 basically show the motion of our sample. The vibration of our MEMS devices includes normal flexural vibration and torsional vibration.

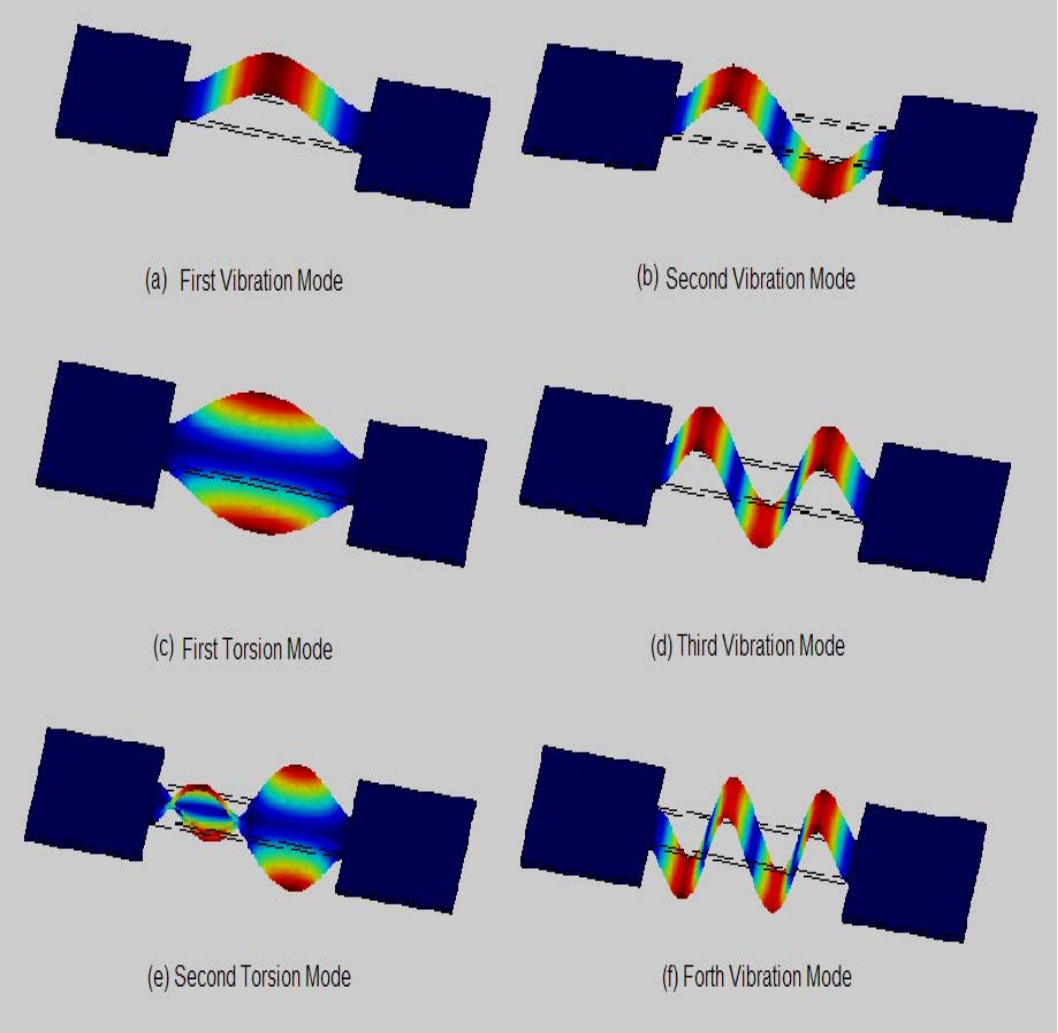

Figure 4.5 COMSOL simulation of beam mode shapes (Color indicates displacement from equilibrium position with minimum displacement at the ends of the beam)

4.3.2 Measurement Result of Optical Interferometry

Through the COMSOL simulation, we have basically the motion information of our MEMS sample. In order to prove that these eigenfrequencies are measurable, we use mature optical interferometry technique [1], as shown in Figure 4.6 to measure the vibration information of our MEMS device. The measured response amplitude and phase as a function of drive frequency for the first six modes of

COMSOL simulation are shown in Figure 4.7 and the results are listed in Table 4.2.

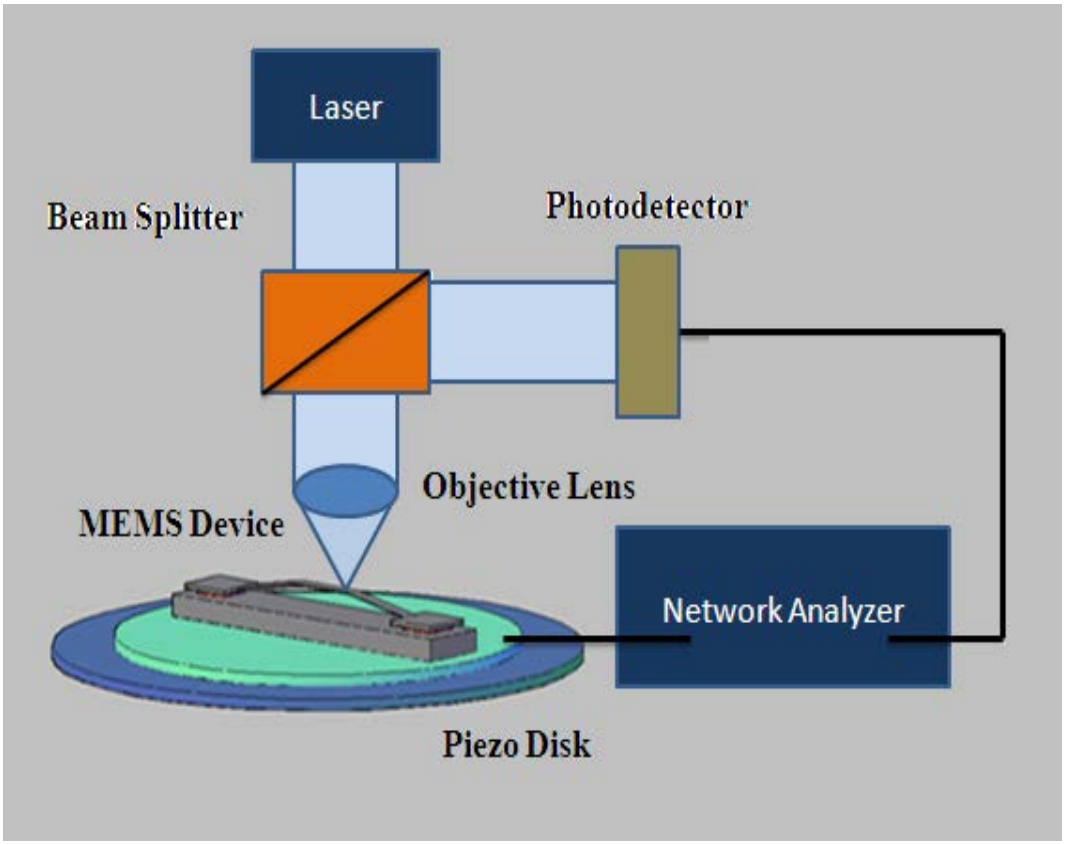

Figure 4.6 Schematic optical interferometry techniques

Table 4.2 Optical Interferometry Measurement Results for a 500 μm long, 100μm wide and 5μm thick Silicon Doubly-clamped Beam with Au and Cr Metal Layers

Vibration Mode	First Flexural Mode	Second Flexural Mode	First Torsion Mode	Third Flexural Mode	Second Torsion Mode	Forth Flexural Mode
Resonance Frequency (kHz)	121.372	310.982	425.921	587.658	832.837	958.476

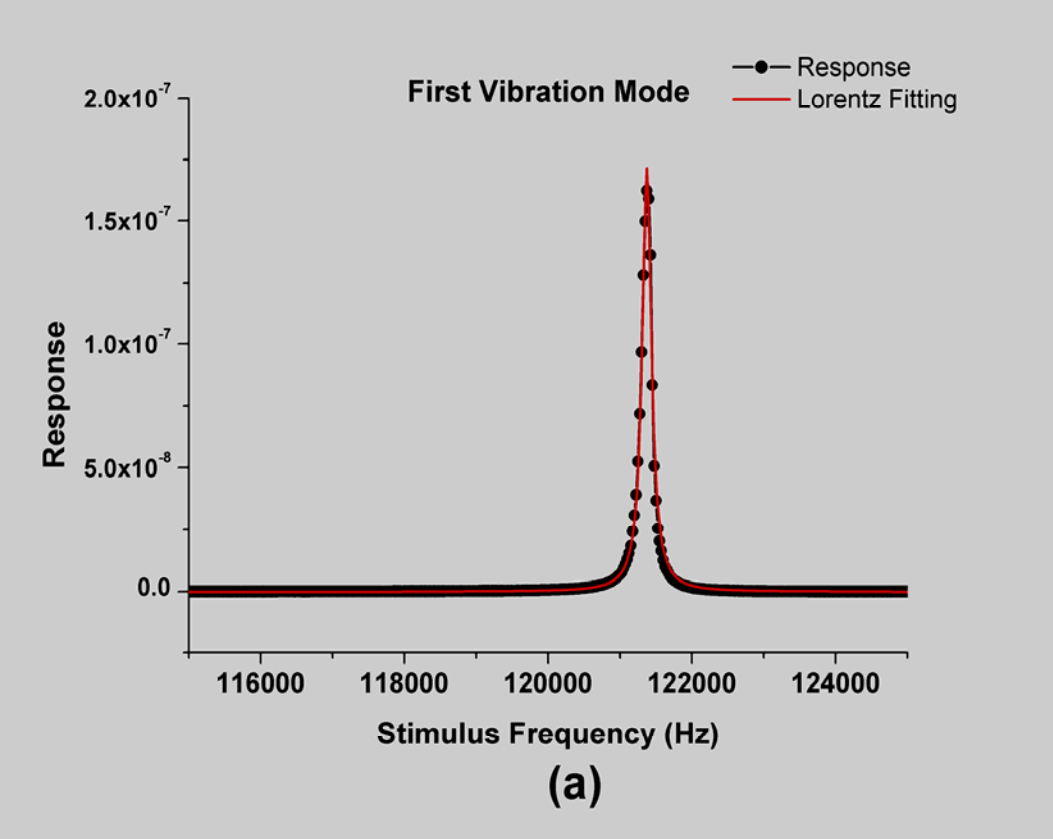
First Vibration Mode
Response
Lorentz Fitting
2.0x10-7
1.5x10-7
1.0x10-7
5.0x10-8
0.0
Response
116000
118000
120000
122000
124000
Stimulus Frequency (Hz)
(a)

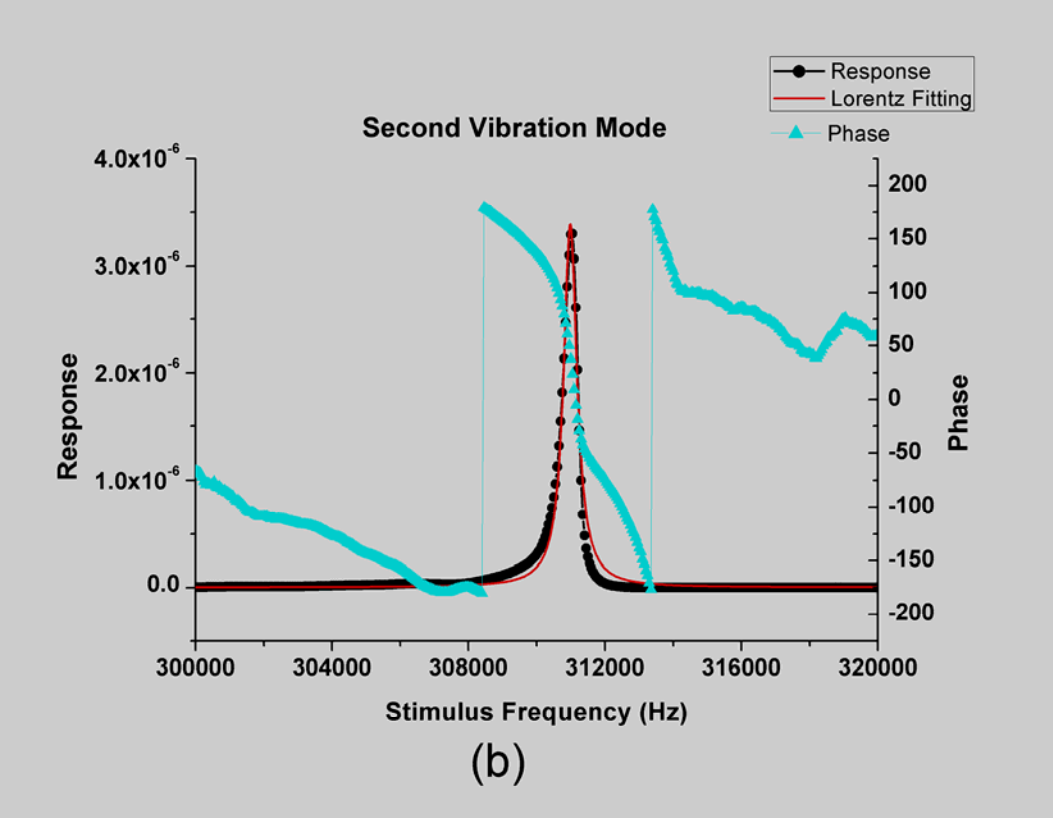
Second Vibration Mode
Response
Lorentz Fitting
Phase
4.0x10-6
3.0x10-6
2.0x10-6
1.0x10-6
0.0
Response
200
150
100
50
0
-50
-100
-150
-200
Phase
300000
304000
308000
312000
316000
320000
Stimulus Frequency (Hz)
(b)

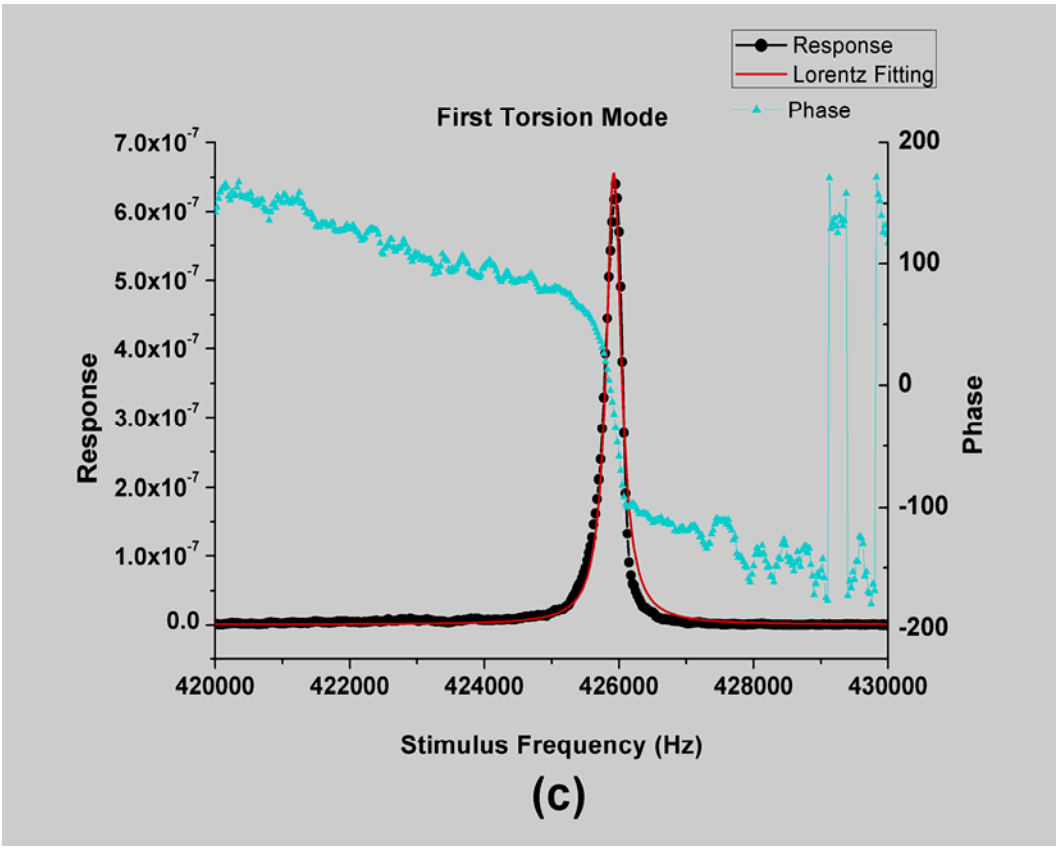
Response
Lorentz Fitting
Phase
First Torsion Mode
7.0x10-7
6.0x10-7
5.0x10-7
4.0x10-7
3.0x10-7
2.0x10-7
1.0x10-7
0.0
Response
200
100
0
-100
-200
Phase
420000
422000
424000
426000
428000
430000
Stimulus Frequency (Hz)
(c)

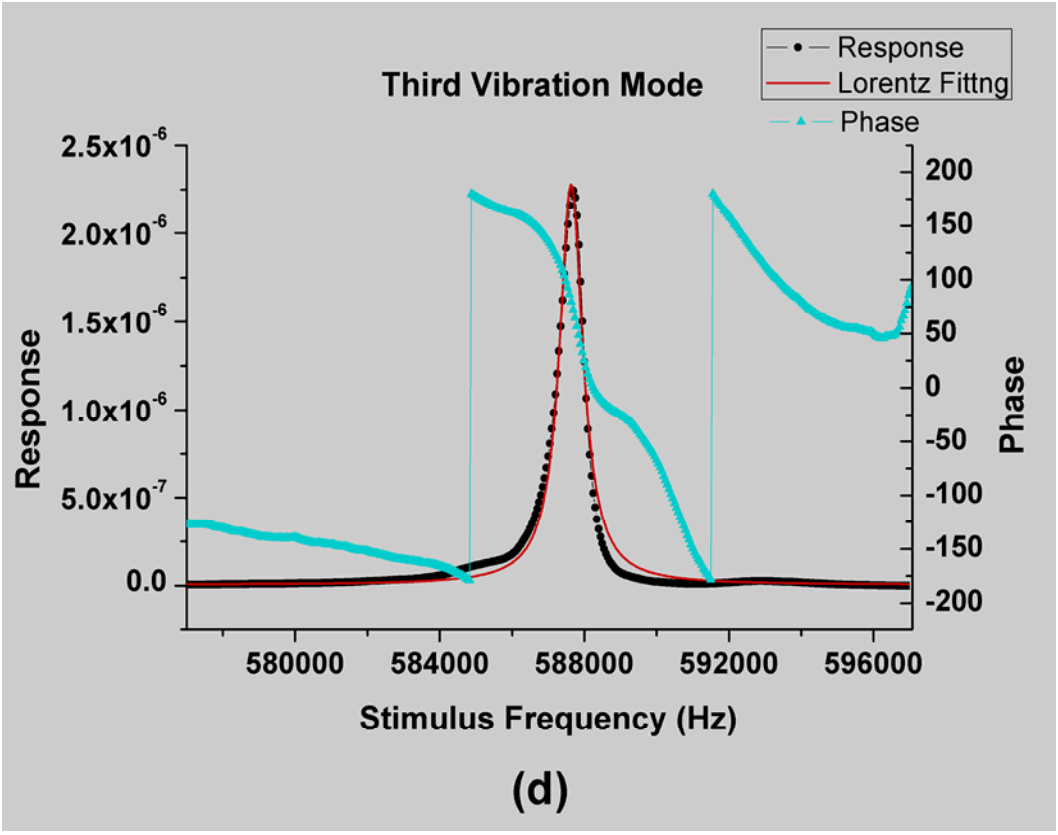
Response
Lorentz Fittng
Phase
Third Vibration Mode
2.5x10-6
2.0x10-6
1.5x10-6
1.0x10-6
5.0x10-7
0.0
Response
200
150
100
50
0
-50
-100
-150
-200
Phase
580000
584000
588000
592000
596000
Stimulus Frequency (Hz)
(d)

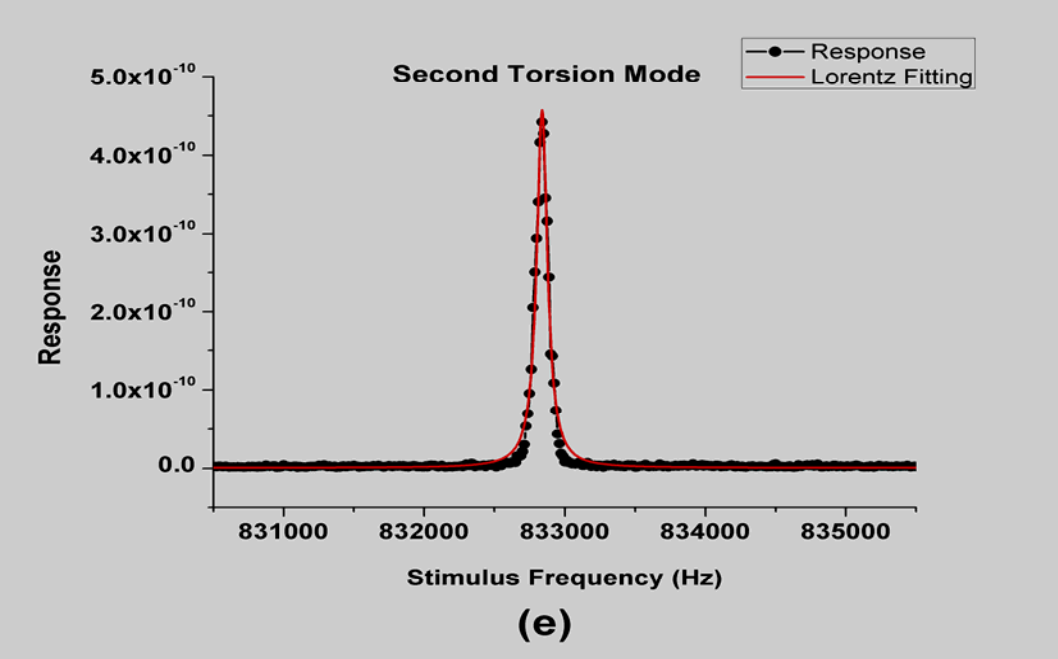

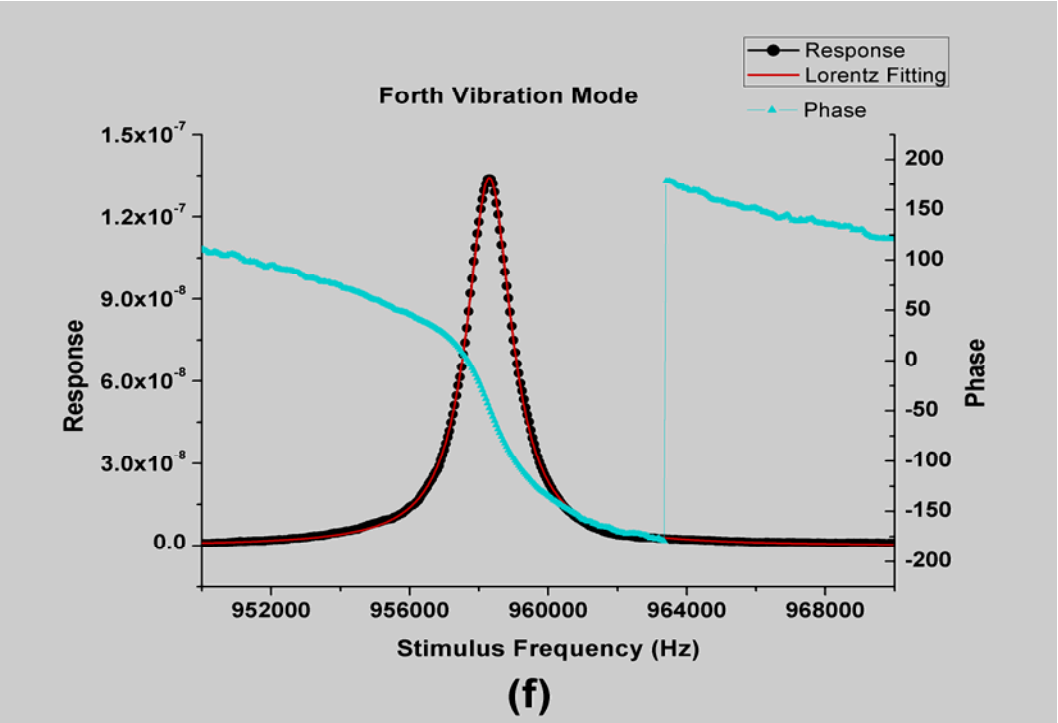

Figure 4.7 Optical interferometry measured response amplitude (black line) and phase (cyan line) as a function of drive frequency. The red line shows the Lorentz fitting for the amplitude of MEMS device

The results which are measured with optical interferometry technique are similar to the COMSOL simulation results. For Figure 4.7 (a) and (e), there is no phase information about the resonance frequency, because we use spectrum analyzer to measure them. This proves that the COMSOL simulation motion of MEMS device is measurable.

4.3.3 The Result of Scanning Tunneling Microscopy Downmixing Readout

In chapter 3, we have talked in detail about the downmixing theory and derived the result of downmixing using math methods. Also in section 4.1, we used RHK software spectrum analyzer to prove scanning tunneling microscopy (STM) downmixing works well. Now we take advantage of this way to measure the MEMS sample which we have simulated with COMSOL and measured with optical interferometry.

The electric circuit is set as Figure 3.6. We use a Labview program, described in Appendix A, to control the signal generator providing sweep frequency and readout the downmixed result from a Lock-in amplifier. Here when two sin function signals are separately sent from the signal generator and Lock-in amplifier reference output, the prediction of X readout in Lock-in amplifier should be similar to the Figure 4.8 (a). Really the vibration amplitude may be complex, so that the motion is not necessarily in phase with the actuating force. The Figure (b) and (c) display two results we measured in our experiment. From the results we can see the output curves are different due the initial point phase difference. In order to avoid this problem and make the result convenient to process, we choose the R readout of the Lock-in amplifier as the result of STM downmixing method. From the equation (3.23),

$$I \propto V_{bias} e^{-2kd} + V_s V_r e^{-2kd} k a_m \sin(\omega_r t - \theta_2) \tag{4.1}$$

The R output of Lock-in amplifier response is the part $V_s V_r e^{-2kd} k a_m$ which is directly related to the vibration amplitude of MEMS devices (a_m) and is

determined by the initial condition of STM. Thus we can use R of Lock-in amplifier to measure the vibration information of MEMS devices and the θ of Lock-in amplifier to measure phase information, respectively.

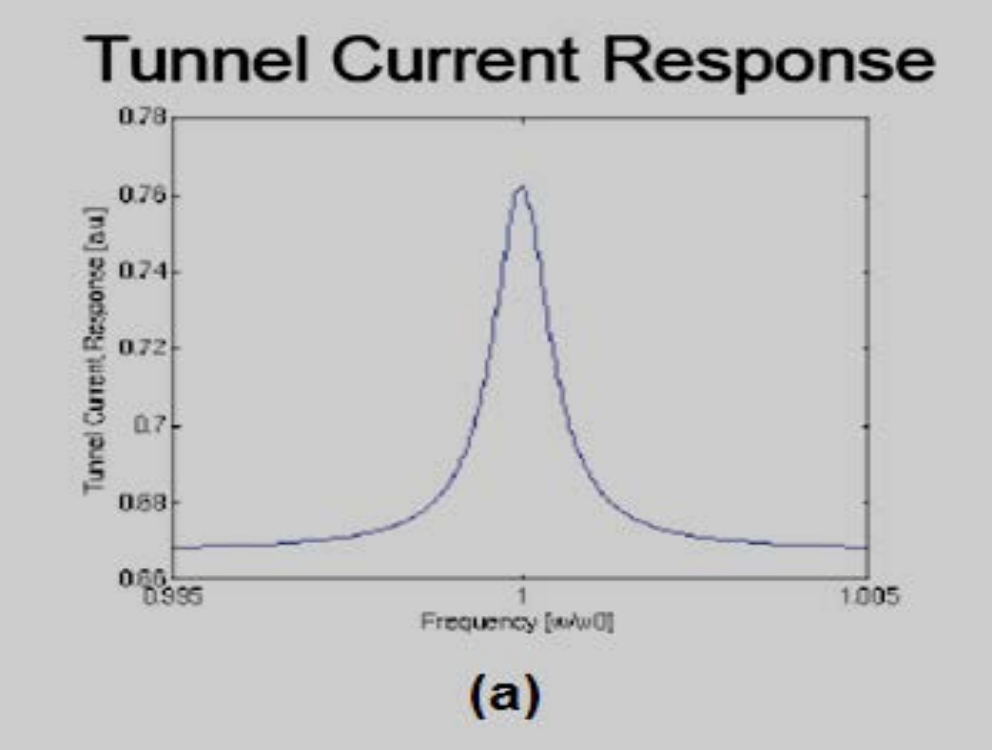

(a)

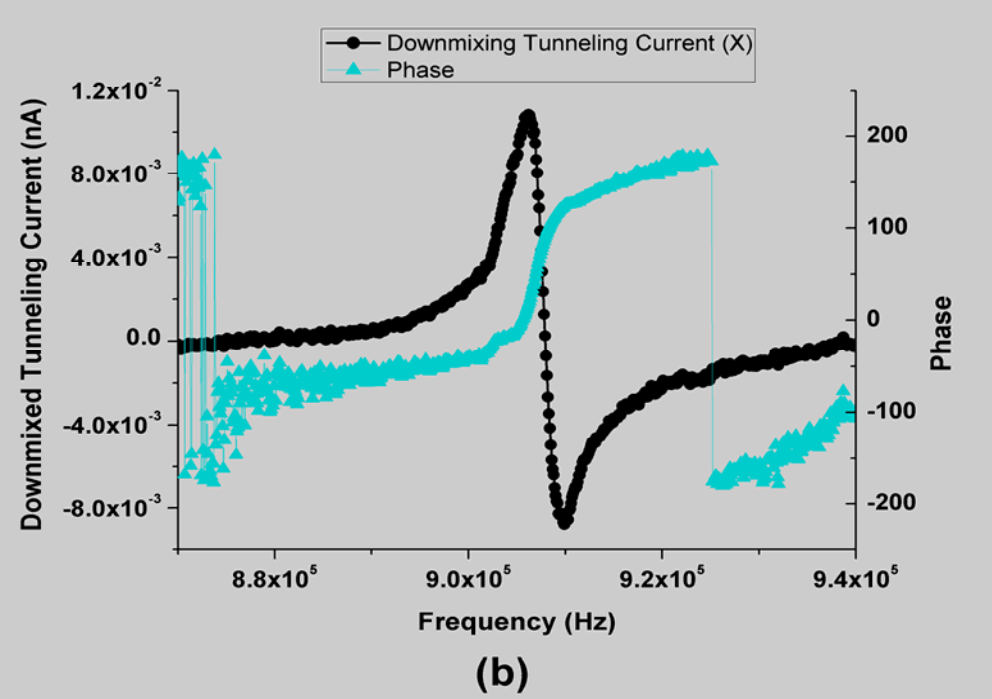

(b)

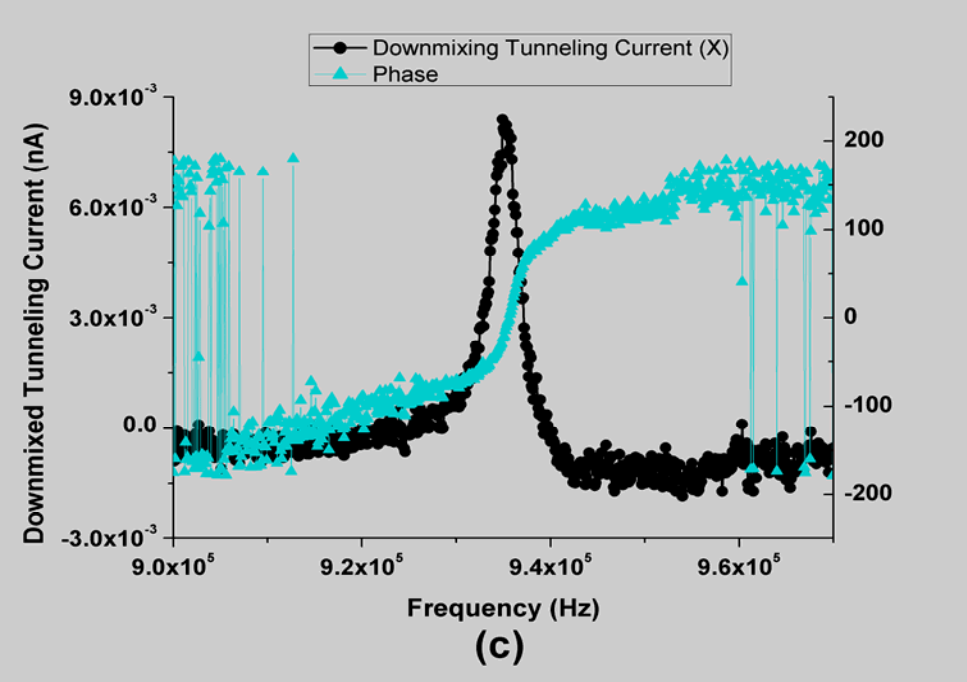

Figure 4.8 The readout Result of STM downmixing (a) Downmixed tunneling response prediction with simulation (b) The real measure result with phase change from 0 to 180 degree (c) The real measure result with phase change from -90 degree to 90 degree

Due to the limitation of our single sideband mixer whose frequency range operates from 0.5 MHz to 15MHz, it is difficult more to measure lower order MEMS modes below 0.5MHz in frequency. Although there is some attenuation for frequency which is lower 0.5MHz, we try to measure the first torsion mode whose resonance frequency is around 450 kHz and get a nice result. For the low frequency fundamental flexural vibration, we are forced to use a different electronic circuit which is similar to the STM downmixing circuits shown in Figure 3.6. In this diagram, the single-side band mixer is replaced with a normal mixer whose output gives the higher side band and lower side-band with the same amplitude at the same time. This means that we can't properly monitor the phase information of the downmixed tunneling current. Appendix B contains the detailed derivation of the output with a normal mixer.

When the Lock-in amplifier is used to measure the downmixed tunneling current, the first term of the tunneling current which is expressed in Equation (4.1) is ignored due to the function of the Lock-in amplifier. Thus the downmixed tunneling current can be written as:

$$I_{downmixed} \propto \frac{1}{2} V_s V_r e^{-2kd} k a_m \sin(\omega_r t - \theta_2) \qquad (4.2)$$

Like we talk before, we measure the R output of the Lock-in amplifier as motion information and which can be expressed as:

$$i_{downmixed} \propto V_s V_r e^{-2kd} k a_m$$

$$i_{downmixed} \propto \frac{V_s V_r k F_0}{\rho A \ell^3} \int_0^{\ell} u_m(x) dx \frac{1}{\omega_m^2 - \omega_c^2 - i\omega_m^2 / Q} \qquad (4.3)$$

Let $A = \frac{-\rho_s(E_F) V_{ac1} k F_0}{\rho A \ell^3} \int_0^{\ell} u_m(x) dx$, they are decided by the beam characteristics, vibration mode of the beam, the piezo disc characteristics and the STM initial condition. For a MEMS device, the A is constant versus frequency change.

$$i_{downmixed} \propto \frac{A}{\omega_m^2 - \omega_c^2 - i\omega_m^2 / Q}$$

$$\left| i_{downmixed} \right| \propto \frac{\left| A \right|}{4\pi^2 \sqrt{(f_m^2 - f_c^2)^2 + (f_m^2 / Q)^2}} \qquad (4.4)$$

To extract the resonance frequency f_m, we fit the measured downmixed tunneling current with the equation (4.4). The detected results of STM downmixing method are listed in Table 4.3. In Figure 4.9, we show the data from the STM downmixed

readout method for the first six vibration mode. For more vibration modes can be seen in Appendix C.

Table 4.3 STM Downmixing Measurement Result for a 500 μm long, 100μm wide and 5μm thick Silicon Doubly-clamped Beam with Au and Cr Metal Layers

Vibration Mode	First Flexural Mode	First Torsion Mode	Third Flexural Mode	Second Torsion Mode	Forth Flexural Mode
Resonance Frequency (KHz)	128.024	440.002	558.481	881.551	983.024

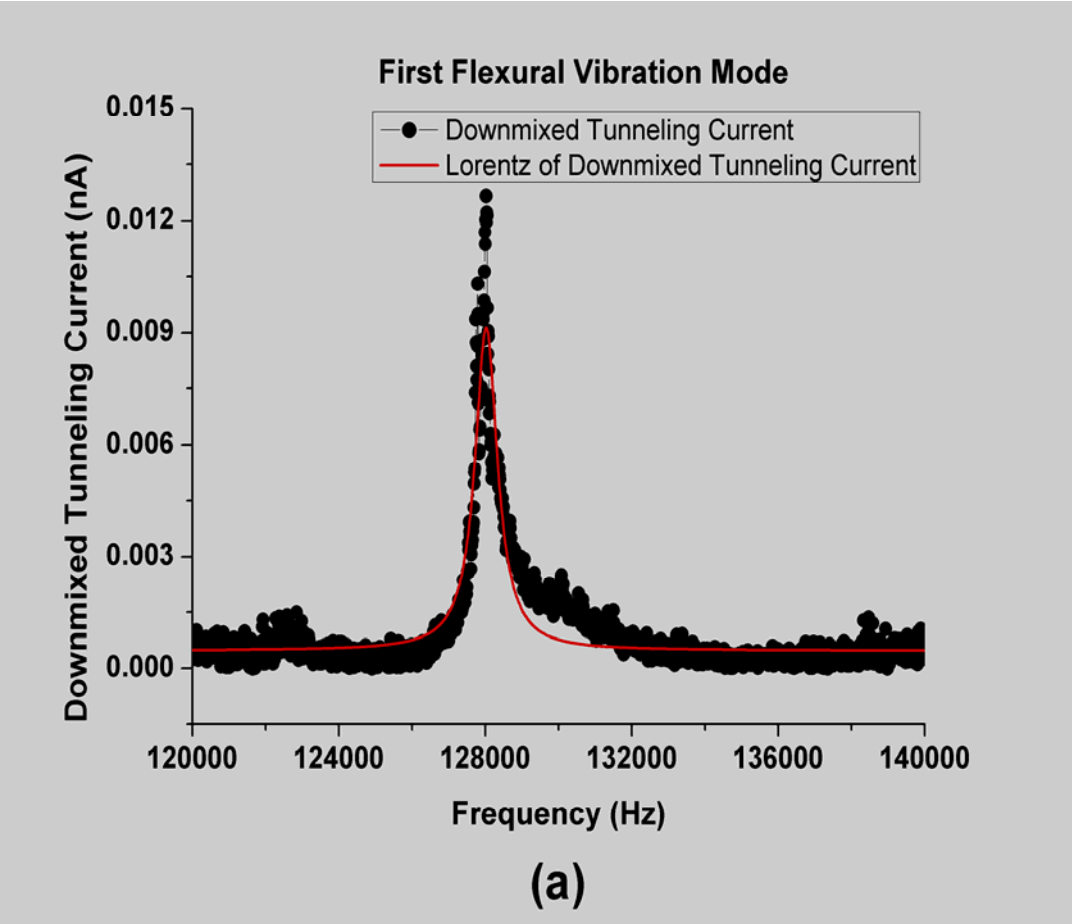

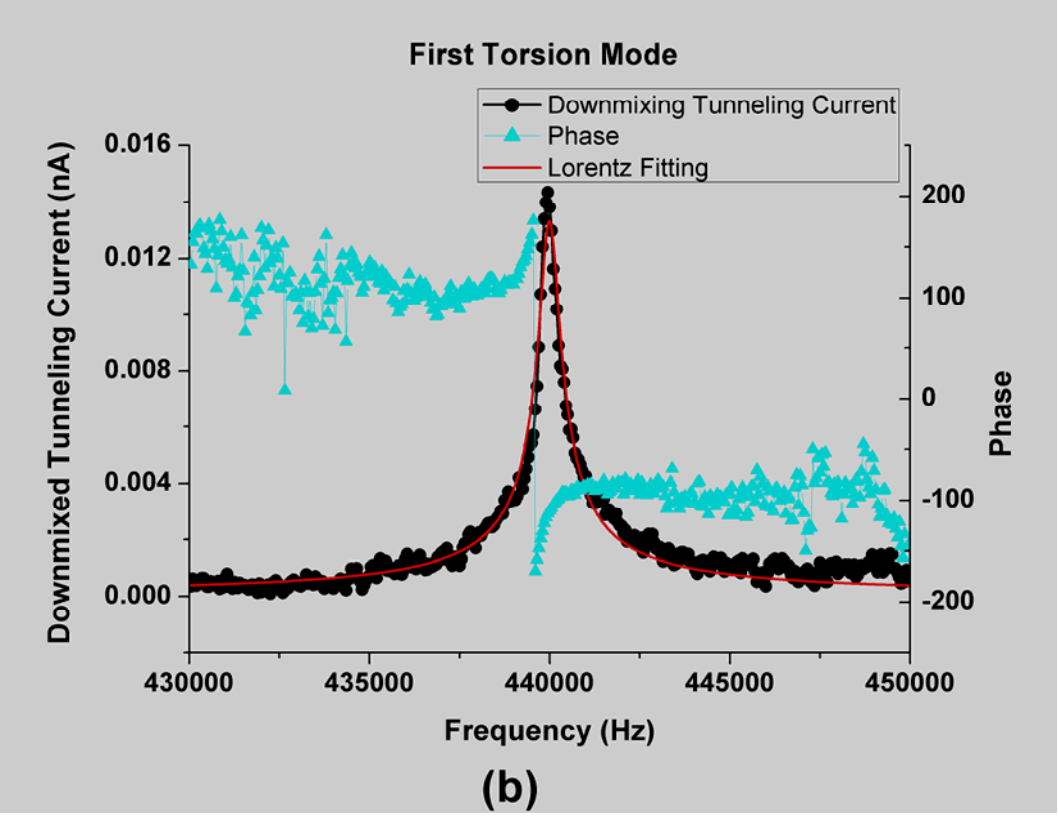
First Torsion Mode
Downmixing Tunneling Current
Phase
Lorentz Fitting
Downmixed Tunneling Current (nA)
0.016
0.012
0.008
0.004
0.000
200
100
0
-100
-200
Phase
430000
435000
440000
445000
450000
Frequency (Hz)

(b)

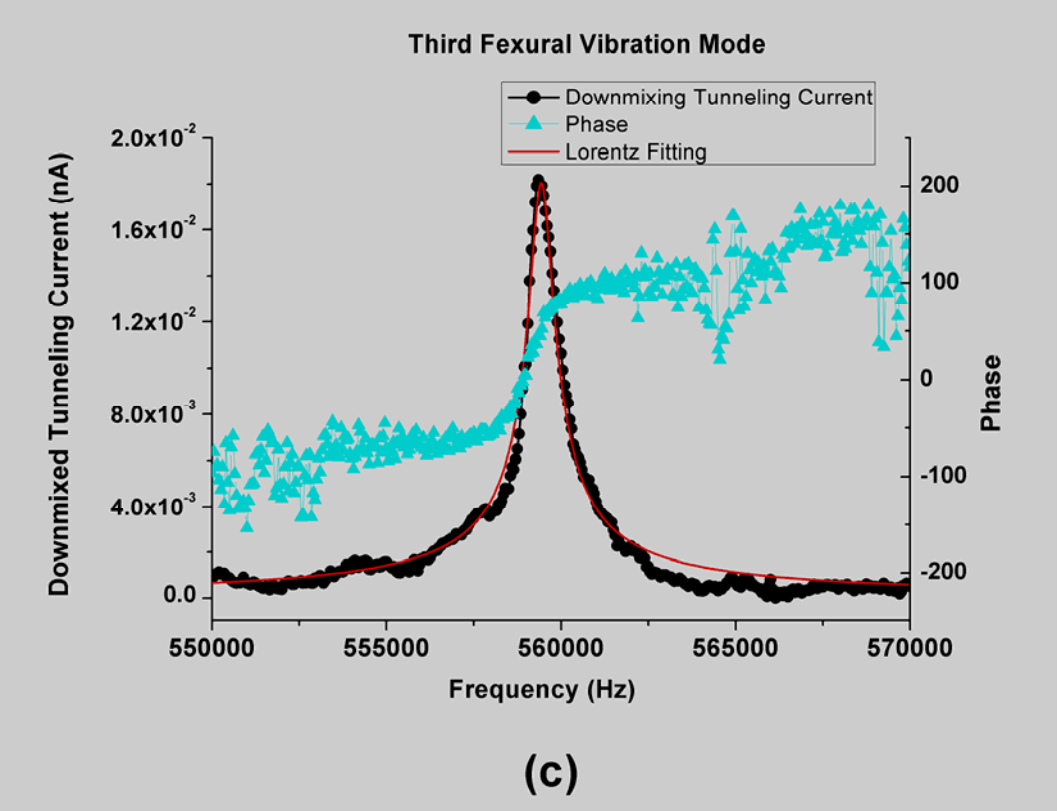
Third Fexural Vibration Mode
Downmixing Tunneling Current
Phase
Lorentz Fitting
Downmixed Tunneling Current (nA)
2.0x10-2
1.6x10-2
1.2x10-2
8.0x10-3
4.0x10-3
0.0
200
100
0
-100
-200
Phase
550000
555000
560000
565000
570000
Frequency (Hz)

(c)

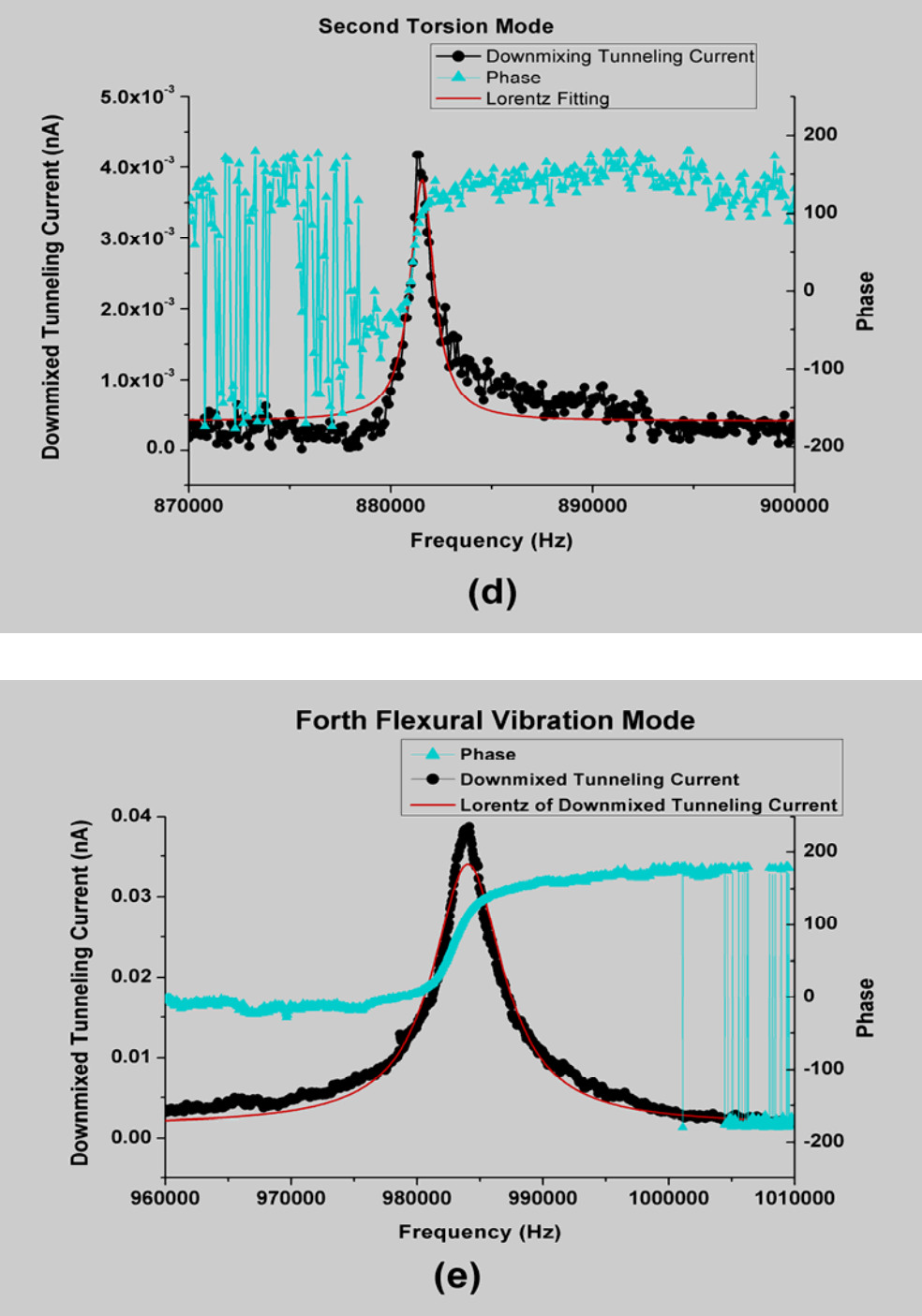

Figure 4.9 The result of STM downmixed Readout (a) Fundamental flexural mode vibration frequency (b) The first torsion mode vibration frequency (c) The third flexural mode vibration frequency (d) The second torsion mode vibration frequency and (e) The forth flexural mode vibration frequency

Comparing Table 4.3 with Table 4.1 and Table 4.2, we can see that the resonance frequencies measured with STM Downmixing are slightly different than those measured with optical interferometry or simulated with COMSOL. The reason is because an interaction potential between the Pt-Ir tip and Gold surface modifies the resonance frequencies [2, 3]. We will talk about this interaction more in the next section where the parameters which impact the results of STM downmixing readout are discussed.

In general, based on the above discussion, we know Scanning Tunneling Microscopy can be used to measure high frequency motion information of MEMS devices with STM downmixing readout method.

4.4. Impact Parameters of Results with STM Downmixing readout Method

We further explore Scanning Tunneling Microscopy (STM) downmixing readout methods and investigate some parameters which will impact the downmixing results. These parameters include the actuating power of piezo disk, the DC tunneling current between the sample and the tip, the DC bias voltage between the sample and the tip, and the measuring position along the MEMS beam.

4.4.1 Forces between STM tip and MEMS Device

In order to exploit the impact parameters of STM, the forces between the STM tip and MEMS device should be known. In the present case, where a small distance for tunneling is required, some physical forces arising from quantized field have to be considered in addition to the electrostatic force; namely, the van der Waals force and Casimir force become relevant.

The van der Waals force, named after Dutch scientist Johannes Diderik van der Waals, is the attractive or repulsive force between atoms, molecules, and surfaces. They differ from covalent bonds and the electrostatic interaction of ions in that they are caused by correlations in the fluctuating polarizations of nearby particles (a consequence of quantum dynamics). In the present case, the van der Waals force can be approximated by using the model of a sphere in front of a plane [4],

$$F_{vdW} = \frac{HR}{6d^2} \tag{4.5}$$

where R is the radius, d is the distance between the sphere and the plane and the interaction constant H is called the Hamaker constant, defined as $H=\pi^2 C\rho_1\rho_2$ where C is the attractive interaction strength and ρ_i, i = 1,2 , is the number density of the molecules in the solid (1 or 2).

The Casimir force is a force between uncharged metallic surfaces as a result of quantum vacuum fluctuations of the electromagnetic field [5] with a large impact in micro- and nanotechnology [6] [7]. According to the proximity force theorem [8] [9], the Casimir force using the geometry of a sphere in front of a plane can be written as:

$$F_{cs} = \frac{\pi^3 \hbar c}{360} \frac{R}{d^3} \tag{4.6}$$

where R is the radius, d is the distance between the sphere and the plane, ħ is the Planck constant/2π, and c is the speed of light. When the separation between the STM tip and MEMS device decreases, the Casimir force rapidly increases.

Also with the sphere model, the capacity of tip and MEMS device is deduced from the expression of the force between a sphere and a plane [10].

$$F = 2\pi\varepsilon_0 V_{bias}^2 \sum_{n=1}^{\infty} \left(\frac{\coth\alpha - n\coth(n\alpha)}{sh(n\alpha)}\right)$$

with

$$\alpha = \arg ch\left(\frac{d+R}{R}\right) \tag{4.7}$$

Where d is the distance between the STM tip and the surface of the sample, R is the radius of the STM tip and ε_0 is vacuum permittivity. In this case d << R, the force in Equation (4.9) reduces to:

$$F_{el} \cong \pi \varepsilon_0 V_{bias}^2 \frac{R}{d} \tag{4.8}$$

Figure 4.10 gives an overview of the distance of the various forces. The parameters used for various forces are H=4x10^{-20}J, ħ=1.05459x10^{-34}J·S, ε_0=8.85x10-12F/m, V_{bias}=0.5 V, and R=5μm. In the case of distance d < 1 nm the Casimir force is far larger than van der Waals force and electrostatic force, even the total of van der Waals force and electrostatic force.

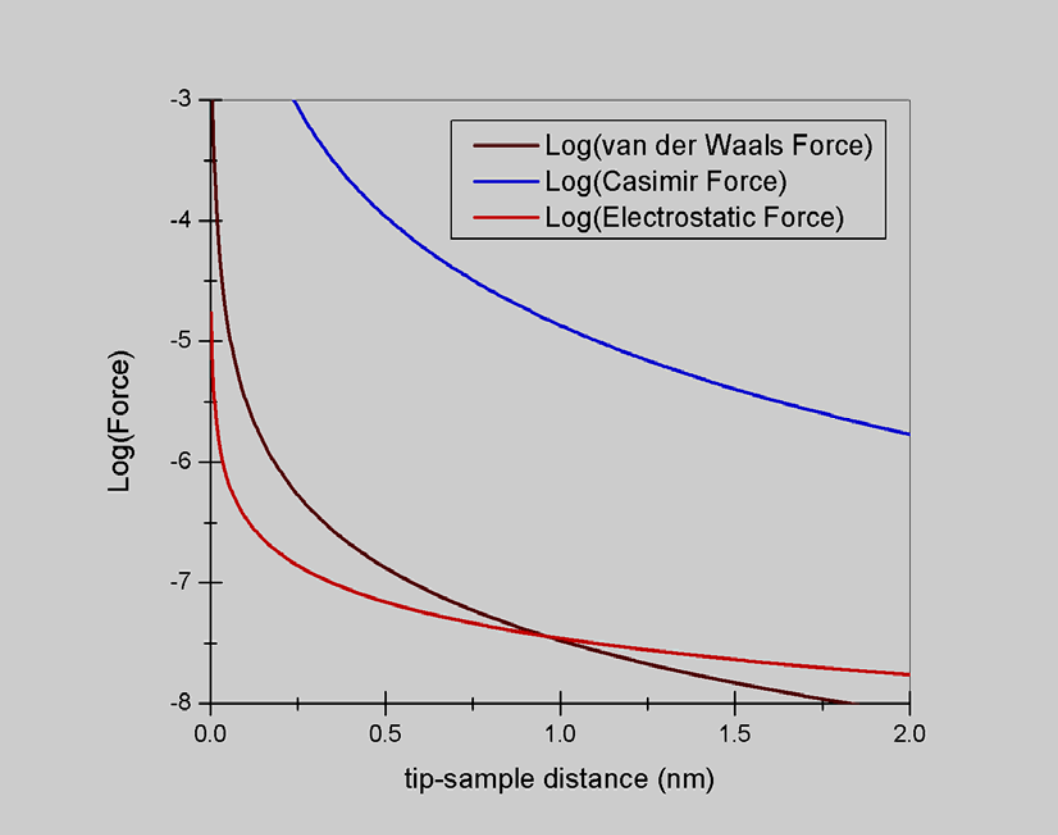

Figure 4.10 Comparison of van der Waals force, Casimir force and Electrostatic force

4.4.2 The Effect of Change DC Tunneling Current

DC tunneling current is used to set the distance between the tip and the sample and impact the sensitivity of measurement. In this section we will focus on the DC tunneling current impact on the downmixed tunneling current and resonance frequencies.

The initial experimental condition is set as: the piezo disk actuating power -11 dBm (22 dBm attenuator is connected between the power splitter and piezo disk), DC bias voltage on the tunneling junction of 0.5 Vrms which directly comes from RHK control system and AC bias voltage on the tunneling junction of 0.1 Vrms which is provided by the single-side band mixer. Following this original experimental condition, we scan the MEMS beam excitation frequency to find the resonance frequencies and downmixed tunneling current peak amplitude as a function of different DC tunneling currents and the results are shown in Figure 4.11. From Equation (4.2), we can see that the downmixed tunneling current is linear to $e^{-2\kappa d}$. Also the DC tunneling current is linear to $e^{-2\kappa d}$. Thus the correlation between the DC tunneling current and downmixed tunneling current is linear relationship. When the DC tunneling current is increased, the downmixed tunneling current should increase and keep this linear relationship. In Figure 4.11(b), we show that the downmixed tunneling current peaks are increasing with increasing DC tunneling current and this agrees with the deduction and the prediction. This result means that at the same conditions we can increase the sensitivity by increasing the DC tunneling current to make the tip close to the sample. Now let us discuss how the DC tunneling current impact the resonance frequency.

At a weak driving force we can model the doubly-clamped beam with a harmonic oscillator characterized by a mechanical resonance frequency $f_0 = 1/2\pi.\sqrt{K/m_{eff}}$, with K spring constant and m_{eff} the effective mass. The change of resonance frequency with the spring constant can be written as:

$$f_0 = \frac{1}{2\pi}\sqrt{\frac{K}{m_{eff}}} \Rightarrow \delta f = \frac{f_0}{2K}\delta K \tag{4.9}$$

When we change DC tunneling current, we can just count the Casimir force based on the discussion of forces between STM tip and MEMS device and Figure 4.10. The change of Casimir force can be written as:

$$\delta F_{cs} = -\frac{\pi^3 \hbar c R}{120 d^4}\delta d \tag{4.10}$$

The force is proportional to δd as $\delta F = K_{tip}\,\delta d$, here K_{tip} is the spring constant which is created by the tip and changes with the change of tip situation, so it is equivalent to spring force. This spring force changes the resonance frequency of MEMS device. From the equation of tunneling current, we can deduce the correlation of the DC tunneling current and the distance between the STM tip and the tunneling surface.

$$I = \rho_s(E_F)V_0 e^{-2kd} \Rightarrow d = -\frac{\ln(\dfrac{I}{\rho_s(E_F)V_0})}{2k} \tag{4.11}$$

From Equation (4.9), (4.10) and (4.11), we can get the correlation of the change of resonance frequency with DC tunneling current change as following:

$$\delta f = -\frac{f_0}{2K}\frac{2\pi^3 \hbar c k^4 R}{15(\ln(\dfrac{I}{\rho_s(E_F)}))^4} \tag{4.12}$$

According to Equation (4.12), the resonance frequency change become small with the increase of DC tunneling current and this agree with the measurement results shown in Figure 4.11 (c).

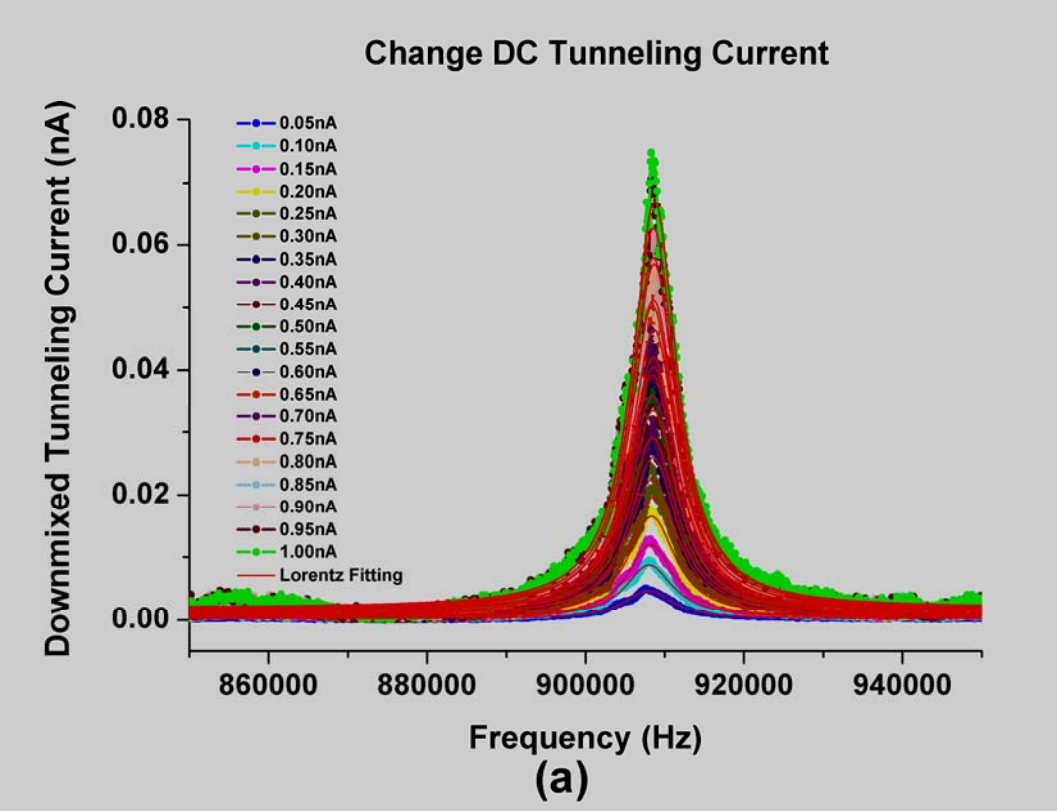
Change DC Tunneling Current
Downmixed Tunneling Current (nA)
0.08
0.06
0.04
0.02
0.00
0.05nA
0.10nA
0.15nA
0.20nA
0.25nA
0.30nA
0.35nA
0.40nA
0.45nA
0.50nA
0.55nA
0.60nA
0.65nA
0.70nA
0.75nA
0.80nA
0.85nA
0.90nA
0.95nA
1.00nA
Lorentz Fitting
860000
880000
900000
920000
940000
Frequency (Hz)
(a)

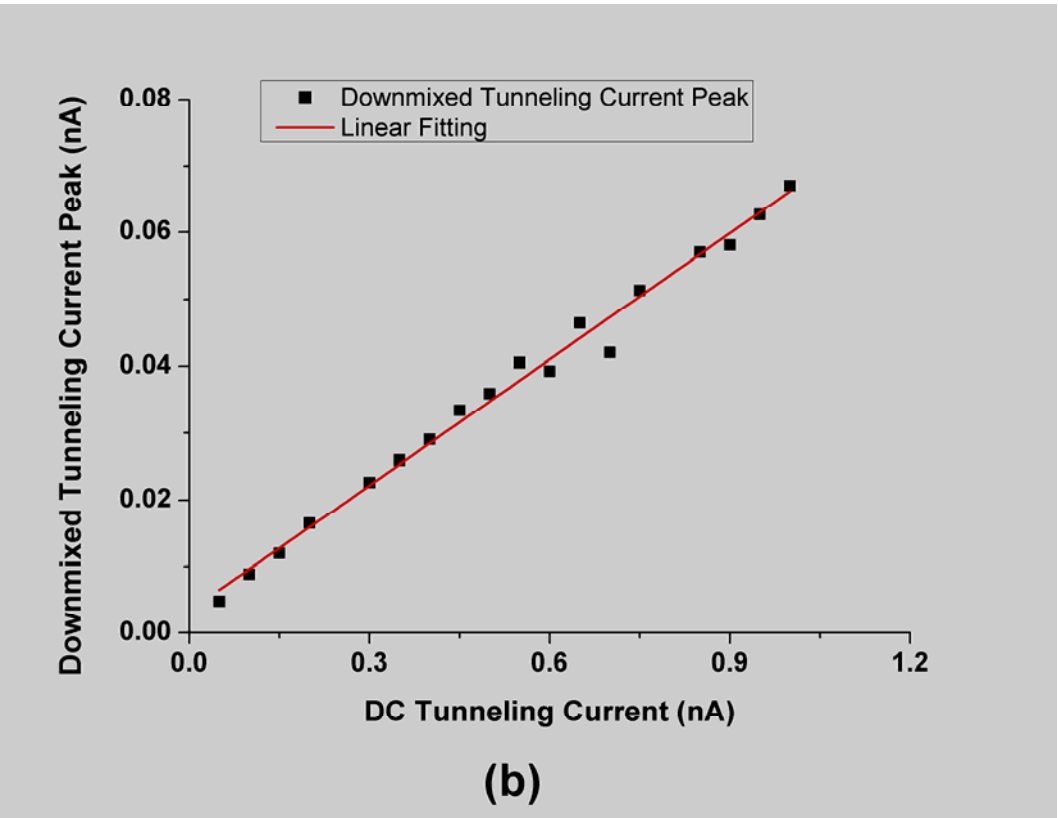
Downmixed Tunneling Current Peak
Linear Fitting
Downmixed Tunneling Current Peak (nA)
0.08
0.06
0.04
0.02
0.00
0.0
0.3
0.6
0.9
1.2
DC Tunneling Current (nA)
(b)

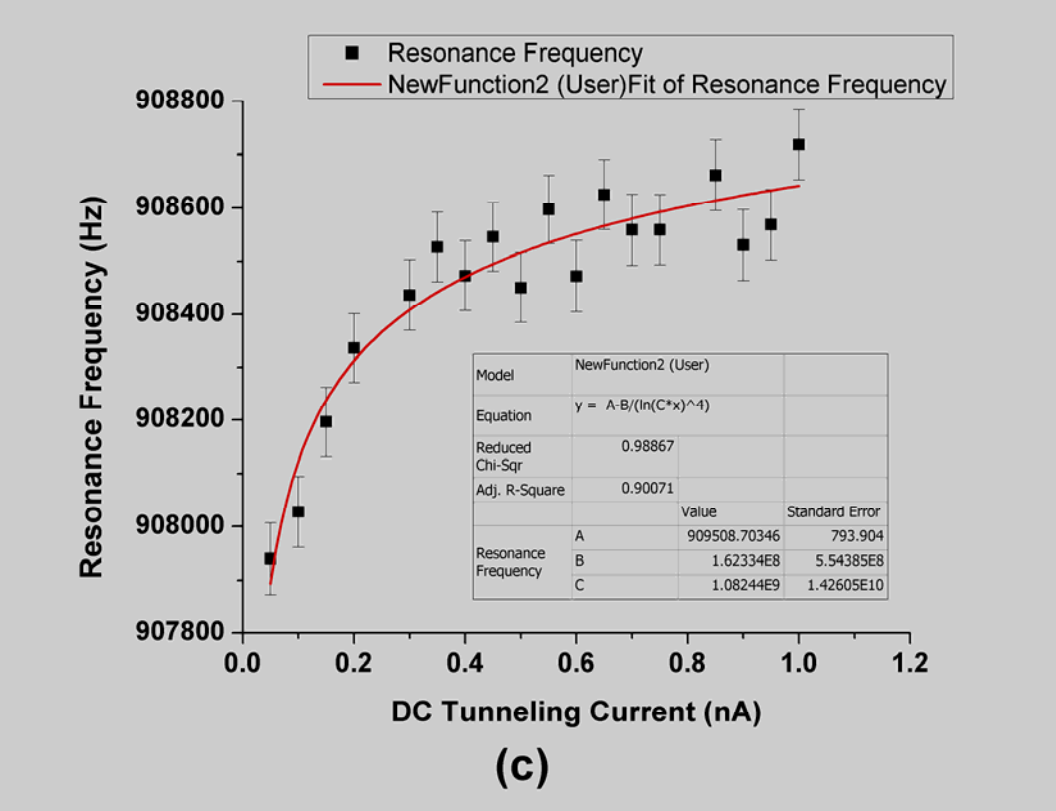

Figure 4.11 The impact of change DC tunneling current (a) The results and fitting of downmixed tunneling current for different DC tunneling current (b) Downmixed tunneling current peak impacted by DC tunneling current (c) Resonance Frequencies impacted by DC tunneling current

4.4.3 The Effect of Change DC Bias Voltage

As an important parameter of STM system, DC bias voltage impacts the downmixed tunneling current and resonance frequencies of STM downmixed method. The value of DC bias voltage decides the relation between the tunneling current and the DC bias voltage [12] and impacts the sensitivity of the STM downmixing method.

During this experiment the piezo disk actuating power, DC tunneling current and AC bias voltage are constant and the DC bias voltage is changed to measure the motion information of MEMS devices. Here, the actuating power of piezo disk is

-11dBm, DC tunneling current is 0.2nA and the AC bias voltage is 0.1Vrms. Based on these conditions, the influence of DC bias voltage to downmixed tunneling current and the resonance frequencies are measured and the results are shown in Figure 4.12.

In Simmons' paper [12], he talked about the relation between the tunneling current density and the bias voltage. For the case that the bias voltage is far less than the barrier height, the tunneling current density as a linear function of DC bias voltage. When the voltage is increasing to intermediate range, the tunneling current density J through the tunneling junction (usually a metal-insulator-metal junction) obeys the general relation:

$$J = \beta(V + \gamma V^3) + O(V^4) \tag{4.13}$$

where β and γ depend on the average barrier height and the tip-sample distance. Since the AC part of bias voltage is constant, when we increase the DC bias voltage, the ratio of the AC bias voltage to the DC bias voltage becomes smaller. This directly causes that the ratio of the dynamic distance to the static distance is smaller and the downmixed tunneling current at resonance frequency become smaller compared to the lower DC bias voltage. The downmixed tunneling current should meet the following correlation:

$$I_{downmixed} \propto \frac{V_{rms}}{V_{DC}} I_{DCtunnelingcurrent} \tag{4.14}$$

From the measured result between the downmixed tunneling current and DC bias voltage in Figure 4.12(b), the curve is basically similar to the discussion in the relation of tunneling current density and bias voltage.

In order to investigate the impact of the various DC bias voltages, we introduce two forces into the equilibrium system of MEMS device: the electrostatic force, attracting the beam toward to the STM tip, and the elastic restoring force, trying

to pull the beam back to its underformed state. The equation of motion for the beam can be written as:

$$EIu_{xxxx} - [T_0 + T(u_x)]u_{xx} + \rho S u_{tt} = \frac{1}{2} C_z[z(x,t)]V^2 \quad (4.15)$$

Here S is the beam's cross-sectional area, E is Young's modulus, ρ is the beam density, and I is the moment of inertia about the longitudinal axis of the beam. The total tension term in brackets, [To + $T(u_x)$], is a sum of residual tension T0 and bending-induced tension: $T(u_x) = (ES/2L)\int_0^L u_x^2 dx$, where L is the beam length. $C_z[z(x,t)]$ is the capacitance between the STM tip and the MEMS device and is calculated based on the sphere model [10].

The beam's total displacement u(x, t) can be written as the sum of a static displacement $z_s(x)$ and a time-varying ac displacement z(x, t): $u(x, t) = z_s(x)+z(x,t)$. To find the frequency in the equation for the time-varying displacement, we approximate the beam shape as $z(x,t) = z_1(t)\sqrt{2/3}[1-\cos(2\pi x/L)]$ [13] [14]. A similar expansion of static deflection, $z_s(x,t) = A_{dc}\sqrt{2/3}[1-\cos(2\pi x/L)]$, is used in the static equilibrium equation to solve for the static deflection amplitude A_{dc}. The equation of motion can be written as [15]:

$$\ddot{z}_1(t) + \omega_0^2 z_1(t) + \alpha_2 z_1^2(t) + \alpha_3 z_1^3(t) = 0 \quad (4.16)$$

For the linear situation, the cubic and quadratic nonlinear coefficients, α_3 and α_2, is equal to zero.

$$\omega_0^2 = [\frac{EI}{3\rho S} + \frac{EA_{dc}^2}{6\rho}](\frac{2\pi}{L})^4 + \frac{T_0}{3\rho S}(\frac{2\pi}{L})^2 - \frac{KV^2}{\rho S} \quad (4.17)$$

Here K is capacitance expansion coefficient and is given by the geometry. The resonance frequencies can be tuned by the DC bias voltage, because the

interaction potential between the Pt-In tip and the gold surface of MEMS devices bring an electrostatic force to make spring constant change. From the resulting equation of motion (4.16), the resonance frequencies decrease with the increase of the DC bias voltage. The results agree with the measurement of STM downmixing method, as shown in Figure 4.12 (c). The similar results about the impact of DC bias voltage to the resonance can be found at Kozinsky's paper [2].

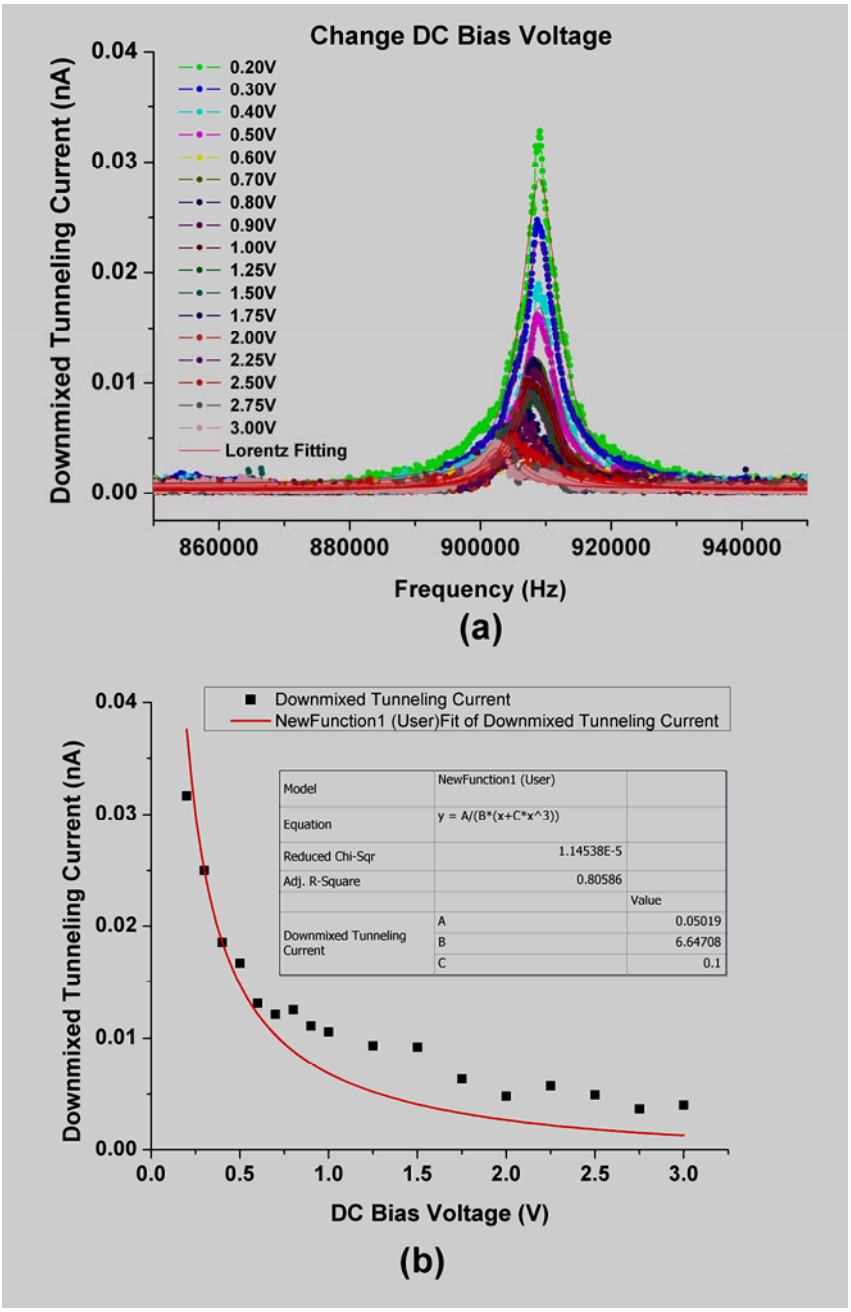

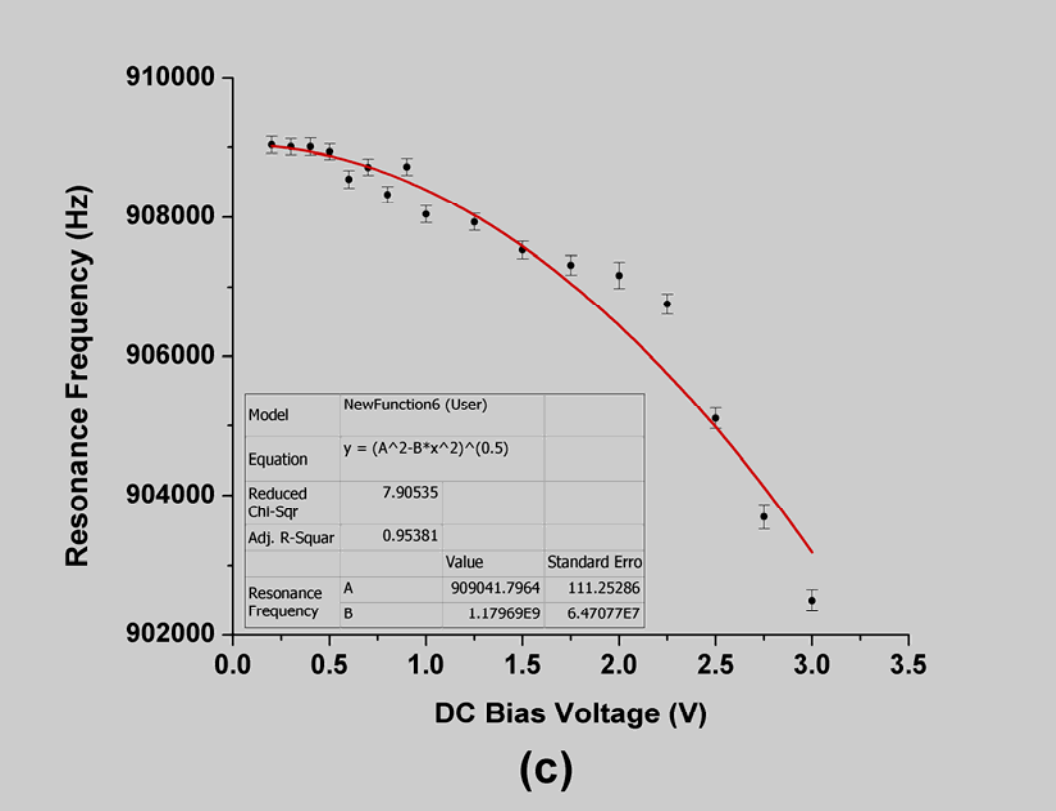

Figure 4.12 Effect of DC Bias Voltage in STM Downmixing Method (a) The results and fitting of downmixed tunneling current for different DC bias voltage (b) Downmixed tunneling peaks change with DC bias voltage (c) Resonance frequencies are modified by DC bias voltage

4.4.4 The Effect of Change Piezo Disk Actuating Power

The change of actuating power causes the change of force which is used to drive the MEMS motion. In the linear region of piezo disk, the driving force is proportional to applied voltage and will increase with increasing actuating power. Figure 4.13 shows the frequency response, measured by reflection, of the piezo disk which is used for actuating our MEMS devices. The inset graphs of Figure 4.13 just amplify the interesting section of Figure 4.13.

The piezo response, through not entirely flat over the range of interest for exciting the MEMS device, is changing relatively slowly with frequency; we will assume

the driving force amplitude is basically flat over the scan range and linear with driving voltage.

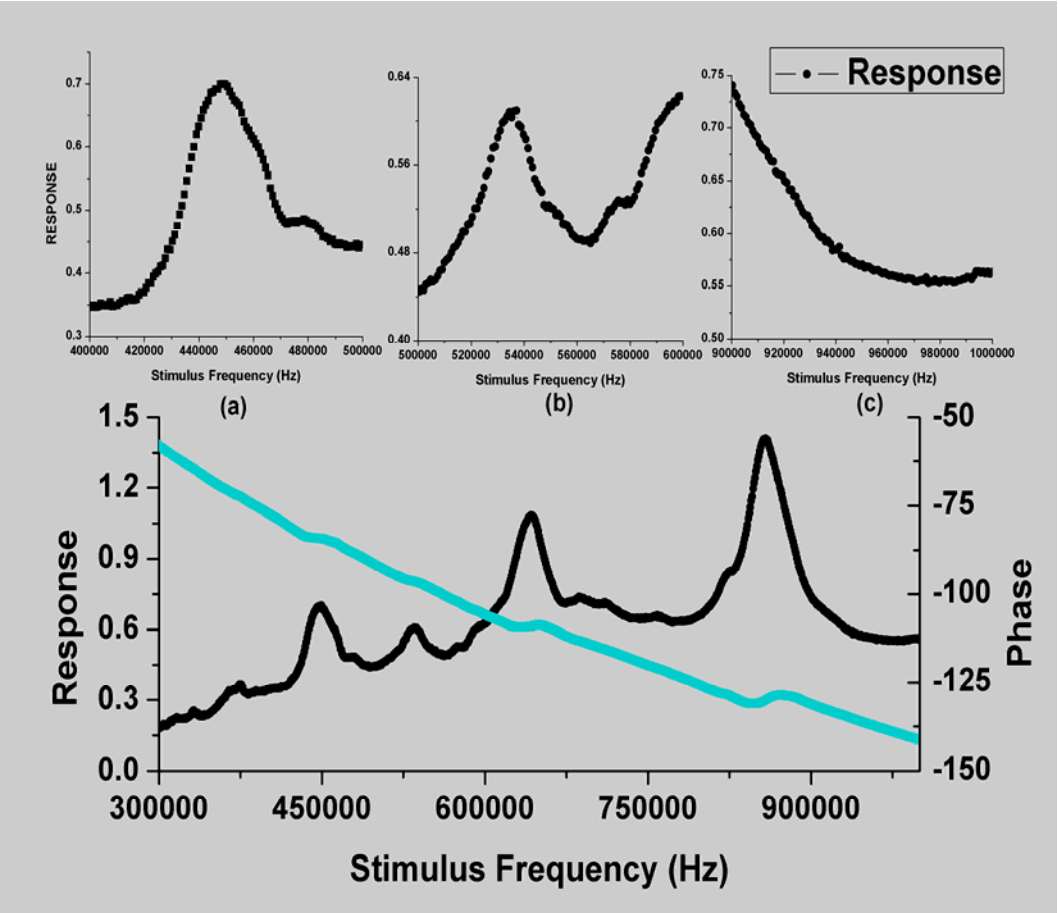

Figure 4.13 The piezo disk frequency response. Inset graph (a) shows the piezo disk frequency response from 400 kHz to 500 kHz (b) shows the piezo disk frequency response from 500 kHz to 600 kHz and (c) shows the piezo disk frequency response from 900 kHz to 1 MHz

The bigger driver force makes the vibration amplitude of our MEMS devices bigger. Thus the gap between the tip and the sample is modified by the actuating power and the downmixed current should change as well. In order to measure the impact of changing actuating power, we set the DC bias voltage to 0.5 Vrms and the DC tunneling current 0.25nA as the initial state of the STM and apply our

down-mixing readout for variable attenuation. Attenuators are used to change the actuating power of the piezo disk. The downmixed tunneling current and the resonance frequencies are modified by the actuating power, as shown in Figure 4.14.

From Equation (3.1) that gives the relationship between the tunneling current and the distance from the tip to sample, we can get the following equation:

$$\begin{aligned} &\partial I = (-2\kappa)\rho_s(E_F)Ve^{-2\kappa x}\partial d \\ &\Rightarrow \frac{\partial I}{\partial d} = (-2k)I \end{aligned} \tag{4.18}$$

From Equation (3.5) the relationship between the actuating force and the applied voltage, we can get the following relationship:

$$\partial F = K\partial V \tag{4.19}$$

Then we use the Equation (3.7) which gives the relationship between the actuating force and vibration amplitude to get:

$$\partial d = \left(\frac{1}{\rho A\ell^3}\frac{1}{\omega_m^2 - \omega_c^2 - i\omega_m / Q}\int_0^\ell u_m(x)dx\right)\partial F \tag{4.20}$$

Using the equation (4.17), (4.18) and (4.19), we can get:

$$\frac{\partial I}{\partial V} = \frac{\partial I}{\partial d}\frac{\partial d}{\partial V} = -\frac{2\kappa I}{\rho A\ell^3}\frac{K}{\omega_m^2 - \omega_c^2 - i\omega_m / Q}\int_0^\ell u_m(x)dx = \text{constant} \tag{4.21}$$

For the given STM initial state, the right side of Equation 4.20 (apart from the current, I) is a constant quantity which depends on the MEMS material and vibration mode. We thus expect the MEMS down-mixed current signal to respond

linearly with applied actuating voltage, consistent with the measurement result which is shown in Figure 4.14 (b).

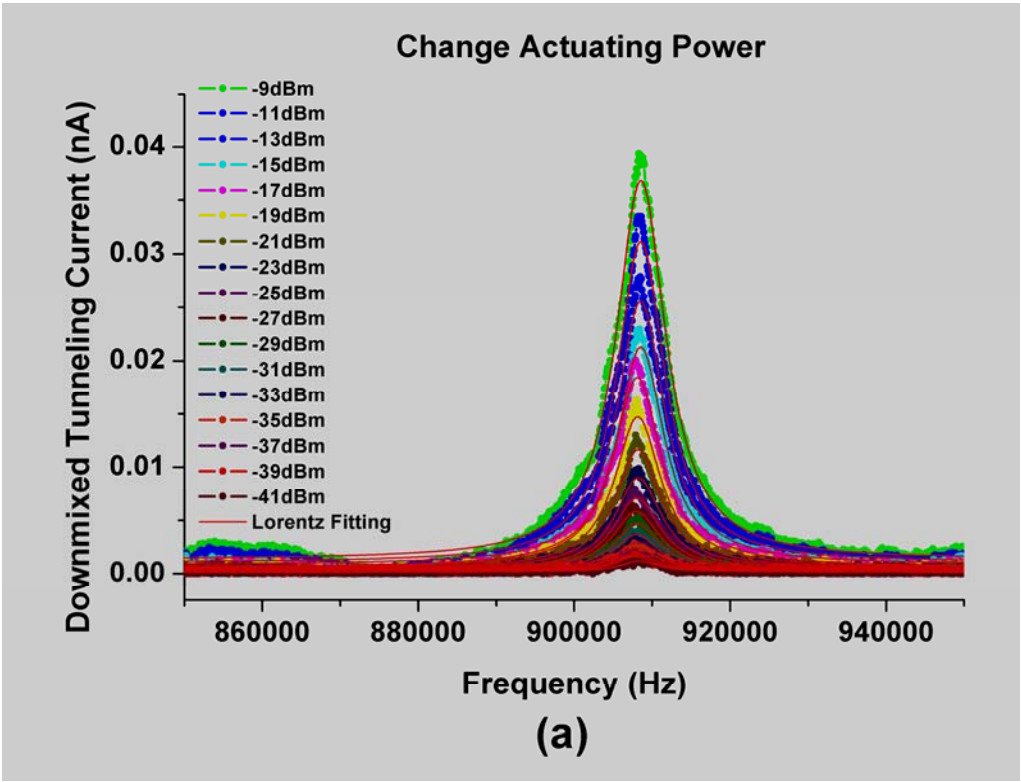

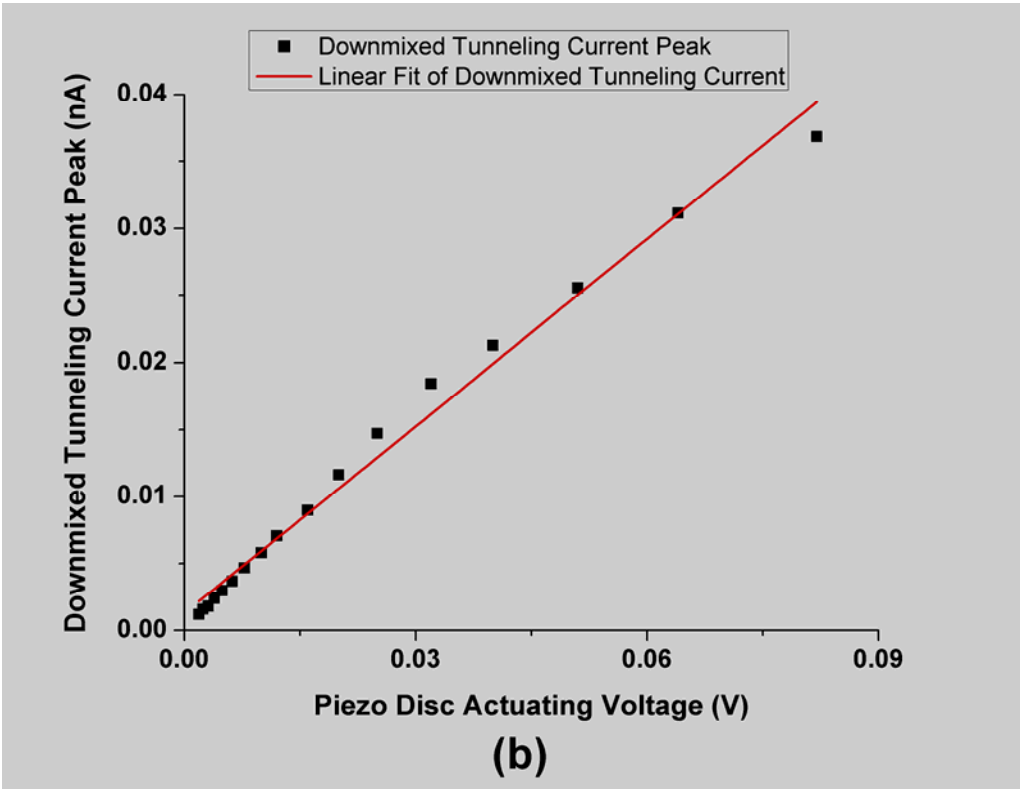

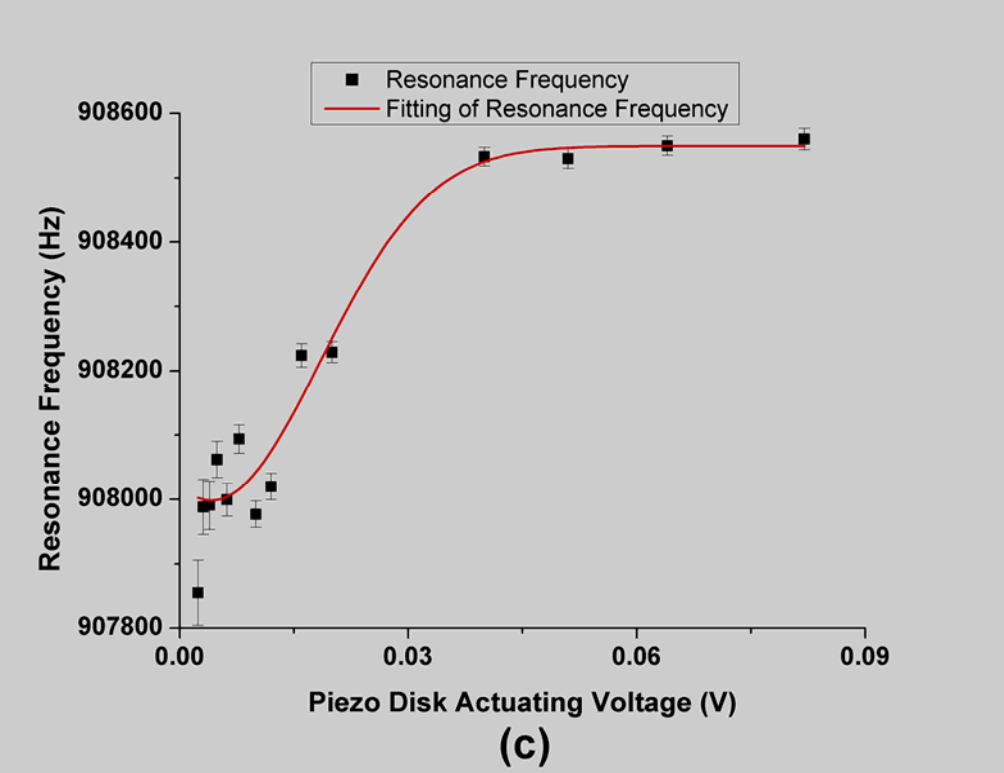

Figure 4.14 The impact of change actuating power. (a) The results and fitting of downmixed tunneling current for different actuating power (b) Downmixed tunneling current peak change with piezo disk actuating voltage (c) The resonance frequencies are modified by the piezo disk actuating voltage

The resonance frequencies are modified by the actuating power, as shown in Figure 4.14 (c). It is possible since the varying actuating power does change the driving forces. Any non-linearity in the MEMS system response to driving force (such as a Duffing or cubic term in the restoring elastic force) can result in frequency shifting at higher powers. That is, the varying driven force seems to result in a spring constant change of the elastic beam [3] [4] that causes the resonance frequency fluctuation shifting. It is instead possible that the tip interaction itself provides an amplitude dependent spring constant that is causing the frequency shifting.

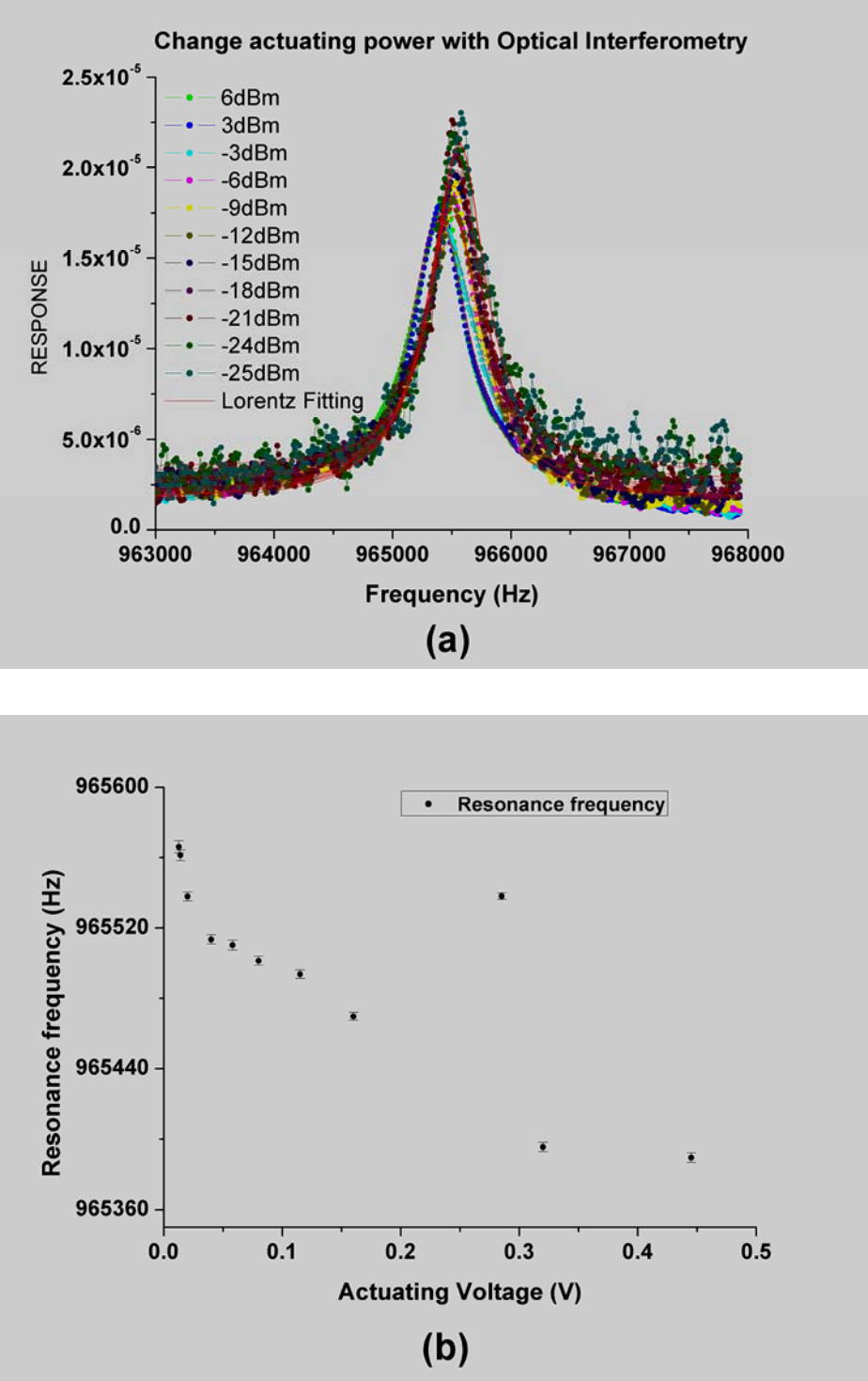

Figure 4.15 Resonance frequency change with actuating power using optical interferometry method (a) The results and fitting curve of response with frequency (d) Resonance frequency are modified by actuating power

To try to shed some light on this frequency dependence, we measure a nominally identical MEMS device under varying drive power using the optical interferometry method. The result is shown in Figure 4.15. In this case, the frequency actually shifts slightly downward with increasing drive voltage, the opposite direction to the STM measured case. In both case, the actual shifts are relatively small. For example, the shift in the STM case is about 1/8th of the mechanical resonance linewidth.

4.4.5 The Effect of the Measuring Position

When the STM downmixing method is used to detect the motion of MEMS devices, there are some intrinsic physical forces between the tip of the STM and the surface of the MEMS device which modify the resonance frequencies of MEMS during the measurement. Since these interaction forces are the point forces, the effect of these interaction forces would be sensitive to the applied position on the MEMS device. In order to exploit the effect of different measuring points, we measure some points along with the beam length direction and the width direction. Along the length direction, we divide the MEMS beam by 10 points along the beam and the distance between adjacent points is uniform. For the width direction we only measure three different points due to the limit of width. These points are measured with the same measurement condition: DC bias voltage of is 0.5Vrms, AC bias voltage is 0.1Vrms, DC tunneling current is 0.2nA and the piezo disk actuating power is -11dBm. Thus will be propitious to compare and analyze the results.

Based on above initial condition, we measure the forth flexural mode information of the 10 points along with the length direction and the measured results are shown in Figure 4.16 (a). The resonance frequencies, the location of each measured point on the forth flexural mode and the phase information of each point at resonance frequency are listed in Figure 4.16 (b). The detail results with phase information for these points can be seen in Appendix D. Here we only simply show the results of the resonance frequencies for these points.

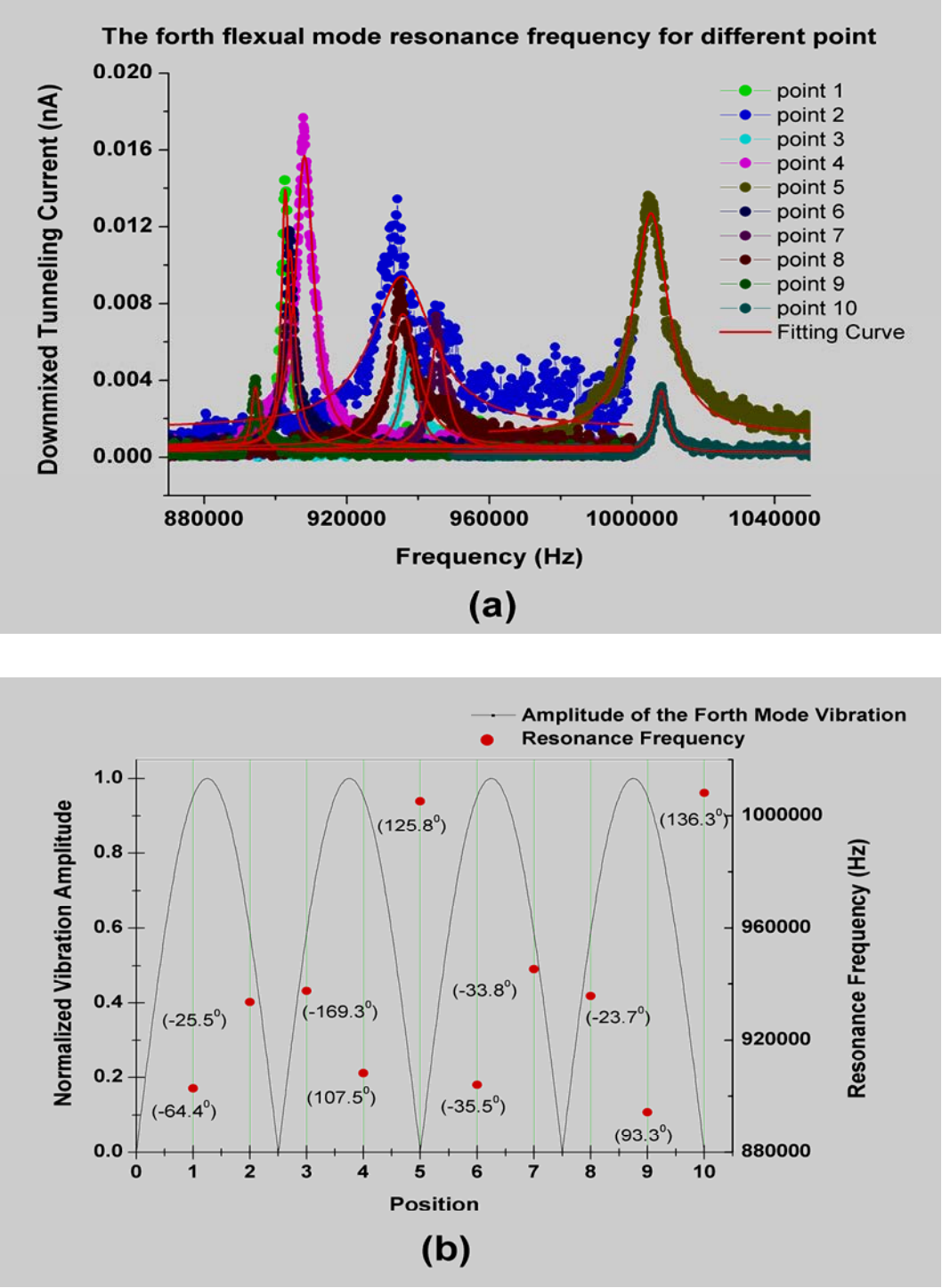

Figure 4.16 Effects of resonance frequencies for the measured point along length direction of the MEMS Beam. (a) The results and fitting curve of different measuring result (b)The solid line show the vibration amplitude for different points of the forth flexural mode and the red dots show the resonance frequency responding point

For the forth flexural mode of the MEMS device, there are four cycles of vibration in the beam. When the beam is roughly divided into 10 uniform parts, three groups with the different distance to the vibration center of each cycle can be gotten. The points 1, 4, 6 and 9 have the similar position for each cycle which is close to the vibration center of each cycle than other two groups. These points have bigger impact on the resonance frequencies and cause that the resonance frequencies shift more than other two groups. The distances from points 2, 3, 7 and 8 to the center of each cycle are medium, so the point cause the impact on the resonance frequencies should smaller than points 1, 4, 6 and 9 and bigger than point 5 and 10. From Figure 4.16, we can see this result. The impact on resonance frequencies for point 5 and 10 is the smallest one and the resonance frequencies of point 5 and 10 are higher than other two situation. But for the point 1, 4, 6, and 9, the impact on the resonance frequencies are the biggest one and the resonance frequencies are the smallest among three groups. From these results, there are two assumptions which cause the change of resonance frequency. One assumption is that there is a force between the tip and the sample surface which depends on the distance between the tip and the sample surface and causes the change of the spring constant. The change of the spring constant of the MEMS beam makes the change of the resonance frequencies. Another assumption is that the tip of the STM introduces a node at the surface of the MEMS beam and the effective length of the MEMS beam is changed and causes the various resonance frequencies at different points.

Otherwise, we also find that some resonance frequencies are little impacted by the measuring points. In Figure 4.17, the resonance frequencies of 10 points along the length direction are almost similar and have no big shift. For the reasons that cause these results, we can’t completely understand until now. The constant frequencies maybe come from the vibration of the tip or the similar impact on the MEMS device for one special mode at the 10 points. In order to fully understand the STM downmixing method, we need to further exploit the impact of the measuring point on the resonance frequencies and phase shift information for the different points.

Although we cannot fully understand how the measuring point impact on the resonance frequencies of the MEMS device, in order to understand the reasons of resonance frequency shift, we also measure the change of resonance frequencies along the width direction for special points. We find that the resonance frequencies change with the measuring position of MEMS beam. The graph (as shown in Figure 4.18) displays the vibration and phase information at point 1415 of 1700 and center. The results show that the resonance frequency increases when the measured point moves to the edge of MEMS beam. For the reasons what cause the phase different, we cannot clearly explain that until now. Although we cannot explain the reasons why the phase is different for different points with the same initial condition, we can clearly find this phase information is related to the initial condition and the measuring point. If we measure the same point with the same initial condition, we get the same results for the phase change. Some works need to do to understand the phase information we measured.

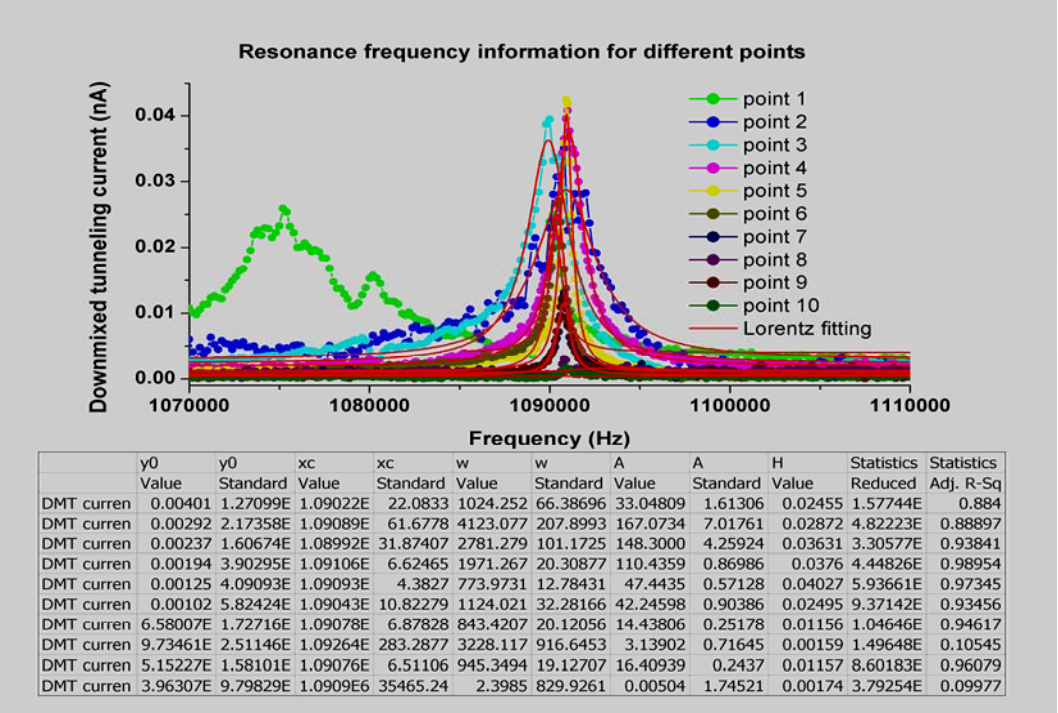

	y0	y0	xc	xc	w	w	A	A	H	Statistics	Statistics
	Value	Standard	Value	Standard	Value	Standard	Value	Standard	Value	Reduced	Adj. R-Sq
DMT curren	0.00401	1.27099E	1.09022E	22.0833	1024.252	66.38696	33.04809	1.61306	0.02455	1.57744E	0.884
DMT curren	0.00292	2.17358E	1.09089E	61.6778	4123.077	207.8993	167.0734	7.01761	0.02872	4.82223E	0.88897
DMT curren	0.00237	1.60674E	1.08992E	31.87407	2781.279	101.1725	148.3000	4.25924	0.03631	3.30577E	0.93841
DMT curren	0.00194	3.90295E	1.09106E	6.62465	1971.267	20.30877	110.4359	0.86986	0.0376	4.44826E	0.98954
DMT curren	0.00125	4.09093E	1.09093E	4.3827	773.9731	12.78431	47.4435	0.57128	0.04027	5.93661E	0.97345
DMT curren	0.00102	5.82424E	1.09043E	10.82279	1124.021	32.28166	42.24598	0.90386	0.02495	9.37142E	0.93456
DMT curren	6.58007E	1.72716E	1.09078E	6.87828	843.4207	20.12056	14.43806	0.25178	0.01156	1.04646E	0.94617
DMT curren	9.73461E	2.51146E	1.09264E	283.2877	3228.117	916.6453	3.13902	0.71645	0.00159	1.49648E	0.10545
DMT curren	5.15227E	1.58101E	1.09076E	6.51106	945.3494	19.12707	16.40939	0.2437	0.01157	8.60183E	0.96079
DMT curren	3.96307E	9.79829E	1.0909E6	35465.24	2.3985	829.9261	0.00504	1.74521	0.00174	3.79254E	0.09977

Figure 4.17 Effect of resonance frequency for different measured point along the length direction of the MEMS beam (small resonance frequency shift)

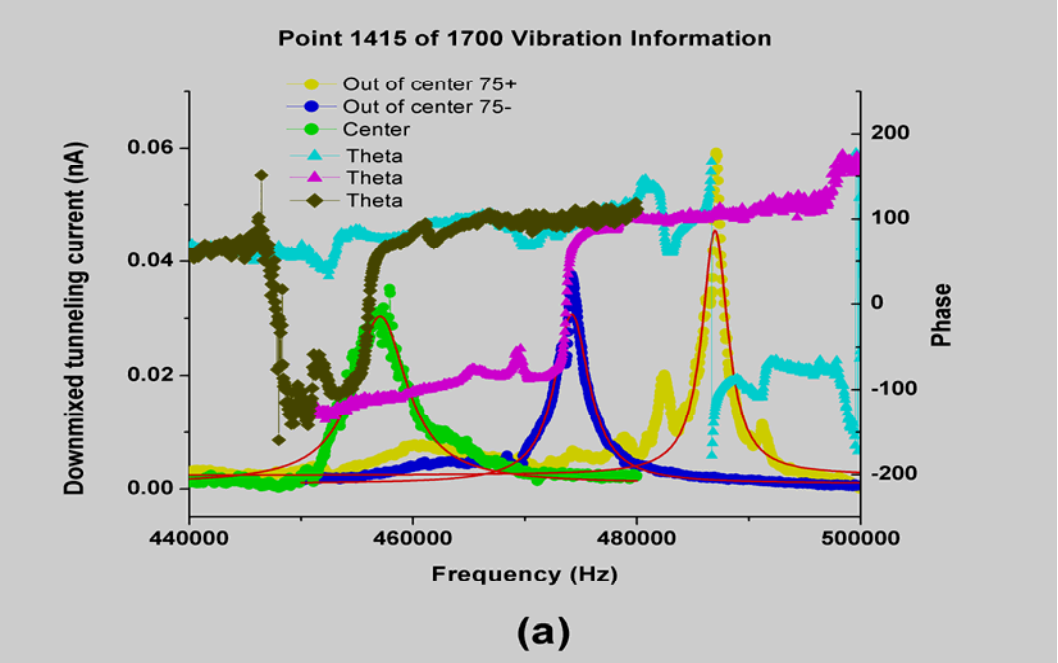

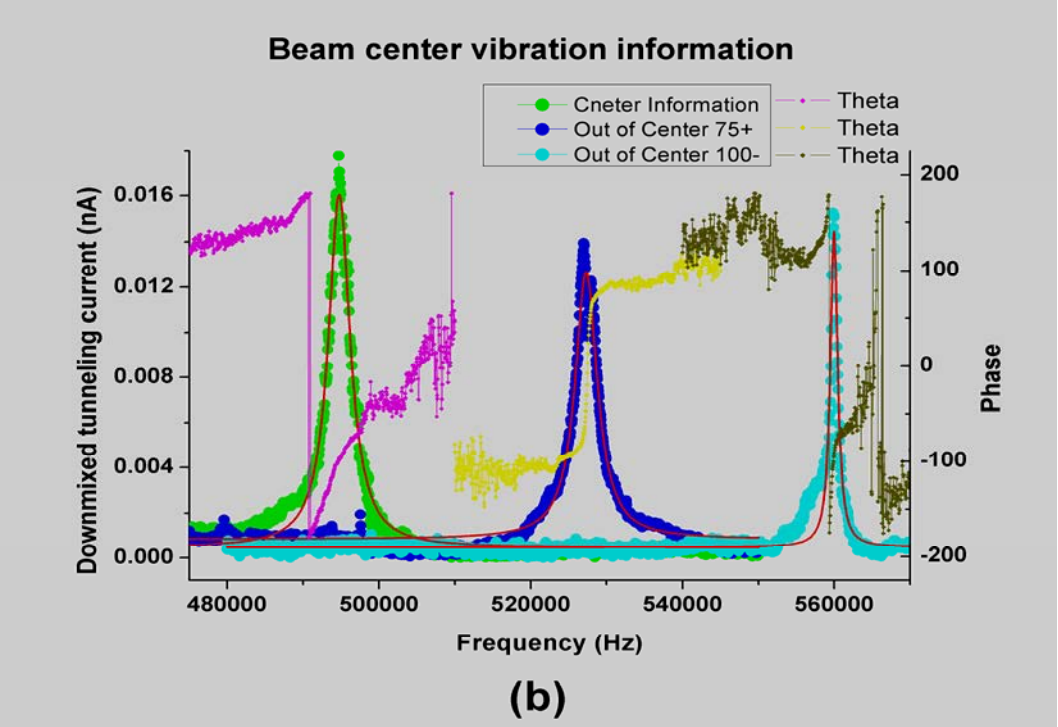

Figure 4.18 Effect of resonance frequency and phase for different points along the width direction of the MEMS beam (a) the resonance frequency and phase information at 1415 of 1700 of the beam (b) the resonance frequency and phase information at center of beam

Until now, we have investigated the STM downmixing method and exploit some parameters of STM system which impact the measurement of MEMS motion. Also the effect of measuring position along the beam is measured. This will help us to use the STM downmixing method to measure small displacement in the future work. Thus we demonstrated that use electron tunneling transducer with STM downmixing technique to measure the high frequency information of MEMS device and overcome the limit of frequency due to the stray capacitance between the amplifier and tunneling junction.

4.5. The displacement sensitivity of the STM downmixing readout method

The displacement measurement sensitivity of the STM downmixing is limited by the current noises present in the measurement system. Given a small change in the distance separation, there will be a corresponding shift in the tunneling current, also downmixed tunneling current. If the change of downmixed tunneling current is below the current noise floor, then it is impossible to distinguish the response from the noise.

For our experiment, we can use the spectrum analyzer software of RHK system to measure the current noise. The measured results are shown in Figure 4.19. From the graphs we can see the current noise is about 10^{-13} A/Hz$^{1/2}$ which include current noise of the amplifier, the shot noise, the current noise which is caused by backaction forces and some electrical and mechanical noise coming from our STM system. When the tunneling current is 0.25nA and $\kappa = 1.15 Å^{-1}$, the displacement measurement sensitivity of our system is about 174 fm/Hz$^{1/2}$. This sensitivity is lower than the calculation prediction in Chapter 3. This is because that the estimation of sensitivity in Chapter 3 omits the force noise and the electrical and mechanical noise of the system. At the real STM system, these noises are existed and cause the higher noise floor. In order to increase the displacement measurement sensitivity of the STM downmixing method, some works are required to overcome the mechanical and electrical noise in the STM system. Otherwise we can increase the tunneling current to increase the

displacement measurement sensitivity of the STM downmixing method. But from the effect of the STM downmixing method, we know that some forces increase with the increasing of tunneling current and these forces will impact the displacement measurement sensitivity.

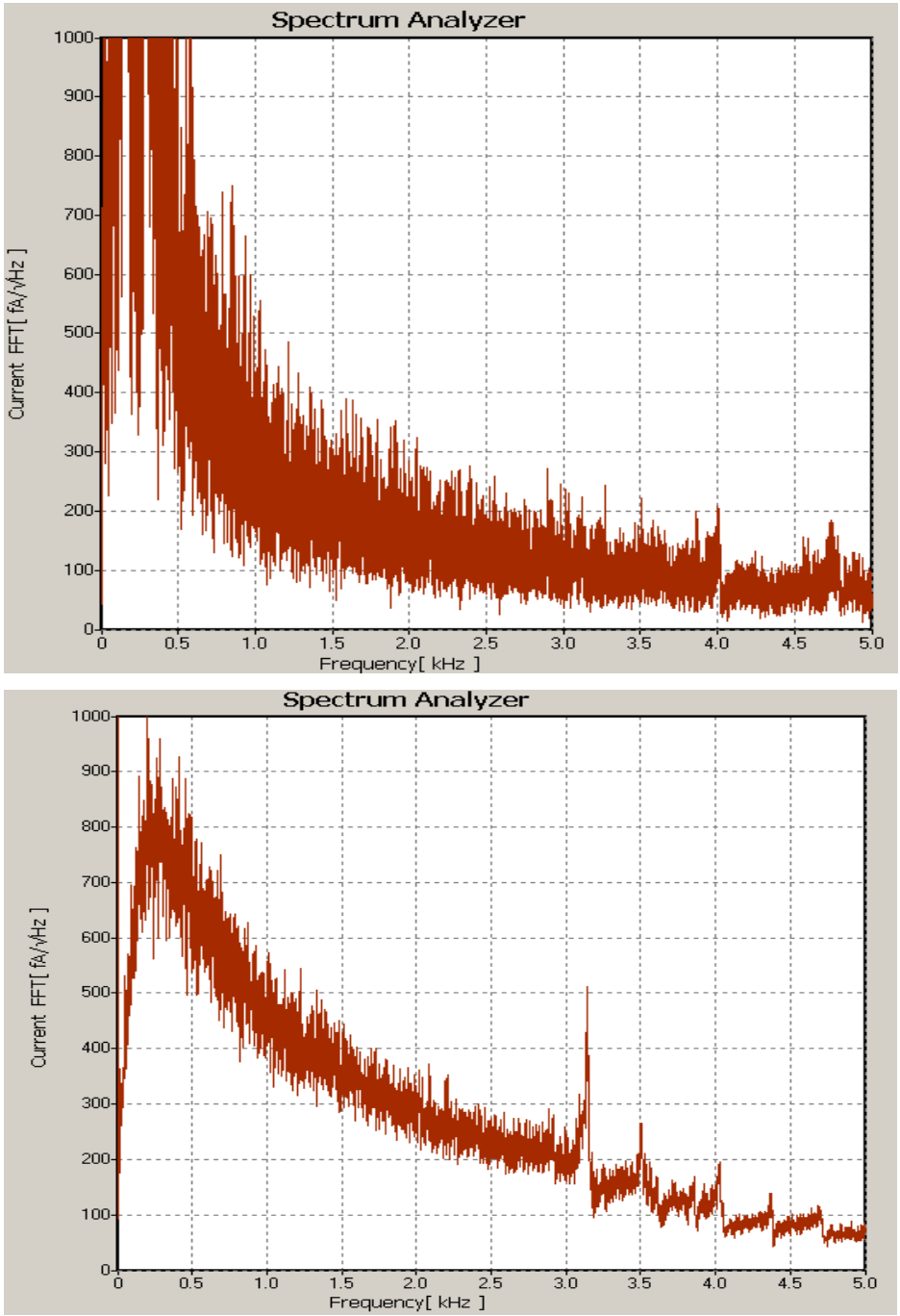

Figure 4.19 The Current noise of STM downmixing method for different point

When STM downmixing method is used to detect the displacement of the MEMS device, the results of downmixed tunneling current are better for smaller amplitude. This is because that for the large vibration amplitude of the MEMS device, some crashes are happened during the measurement due to the slow response of STM and fast vibration of the MEMS device. This cause that some information is lost and there are multiple peaks in the results of downmixed tunneling current. So in our measurement, we try to measure higher vibration mode of the MEMS device and these modes give us better results due to smaller vibration amplitude. For some mode with large vibration amplitude, we can try to change the measuring position and get better results. For example, in order to measure the first mode, we move the tip to close the edge of the beam and get better results. This is because two reasons: one is that the vibration amplitude is smaller at the edge of the beam and this avoids the crash; another is that the impact of the forces between the STM tip and the sample on the beam are smaller than other places.

4.6. Conclusion

We demonstrate the results of STM downmixing method which are compared with the COMSOL simulation results and optical interferometry measurement results and investigate the impact parameters on the downmixed tunneling current. With the current conditions, the displacement measurement sensitivity is about 173fm/$Hz^{1/2}$ which is bigger the theory prediction. This means that we still have room to improve the sensitivity with our STM downmixing method. The future work will focus on the improvement of sensitivity and the application in NEMS displacement measurement.

REFERENCE

1. Carr, D. W., Sekaric, L., and Craighead, H.G., Measurement of nanomechanical resonant structures in single-crystal Silicon, *J. Vac. Sci. Technol. B,* 16, 3821, (1998)

2. Kozinsk, I., Postma, H. W. Ch., Bargatin, I., and Roukes, M. L., Tuning nonlinearity, dynamic range, and frequency of nanomechanical resonators, *Appl. Phys. Lett.*, 88, 253101, (2006)

3. Flowers-Jacob, N. E., Schmidt, D. R., and Lehnert, K. W., Intrinsic Noise Properties of Atomic Point contact Displacement Detectors, *Phys. Rev. Lett.,* 98, 096804, (2007)

4. Israelachvili, J. N., Intermolecular and Surface Forces, Academic, London, (1992)

5. Casimir, H. B. G., On the attraction between two perfectly conducting plates, *Proc. K. Ned. Akad. Wet.*, 51, 793 (1948)

6. Chan, H. B., Aksyuk, V. A., Kleiman, R. N., Bishop, D. J. and Capasso, Federico, Quantum mechanical actuation of Microelectromechanical system by the Casimir force, *Science*, 291, 1941, (2001)

7. Bulks, E., and Roukes, M. L., Stiction, adhesion energy, and the Casimir effect in micromechanical systems, *Phys. Rev. B*, 63, 033402, (2001)

8. Derjaguin, B. V., Abrikosova, I. I., Lifshitz, Direct measurement of molecular attraction between solids separated by a narrow gap, *Q. Rev. Chem. Soc.*, 10, 295, (1956)

9. Blocki, J., Randrup, J., Swiatecki, W. J., and Tsang, C. F., Proximity forces, *Ann. Phys.*, 105, 427, (1977)

10. Durand, E., Electrostatique, Tome II Problemes generaux, Conductrues, p 207, (Masson Paris, 1966)

11. Zalalutdinov, M., Ilic, B., Czaplewski, D., Craighead, H. G., and Parpia, J. M., Frequency-tunable micromechanical oscillator, *Appl. Phys. Lett.*, 77, 3287, (2000)

12. Simmons, J. H., Generalize Formula for the Electric Tunnel Effect between Similar Electrodes Separated by a Thin Insulating Film, *J. Appl. Phys.*, 34, 238, (1963)

13. Postma, H. W. C., Kozinsky, I., Husain, A., and Roukes, M. L., Dynamic range of nanotube- and nanowire-based electromechanical system, *Appl. Phys. Lett.*, 86, 223105, (2005)

14. Eisley, J. G., Nonlinear Vibration of beams and rectangular plates, *J. Appl. Math Phys.*, 15, 167, (1964)

Chapter 5 Future Direction

That electron tunneling transduction can be used to measure the high frequency motion of MEMS devices has been demonstrated by STM downmixing readout of nanomechanical motion. But there are some problems which are left for further exploitation. We will present some ideas for future direction in this chapter and hope they will be helpful for the future work.

5.1. How to measure the nanoscale device

MEMS sized devices were chosen in our project due to the difficulty in aligning the tunneling tip on top of individual device structures with the optical telescope. In order to solve this problem and align the tip on the top of nanoscale devices, one of the methods in mind is field emission (FE) scanning electron microscopy. The basic difference between scanning tunneling microscopy (STM) and field emission scanning electron microscopy (FESEM) is the applied voltage. For a FESEM, a FE current between a sharp metallic tip and sample is employed to resolve surface features and an applied voltage much larger than work function of the emitting material was used [1]. With field emission, a bigger gap can be kept between the tip and the sample. Thus we can scan large areas to get the image of the nanoscale device and do not worry that the tip can crash the nanoscale device and cause sample or tip damage.

In order to make FESEM work, two problem need to be solved. The first one is the control of scanning. The inherent STM system scan range is too small to meet the requirement of FESEM scanning area. Though we have attocubes which can scan 9μm by 9μm area, the initially purchased controller only provides abrupt stepping motions and is not effective at X-Y scanning due to the difference between the forward scanning step and backward scanning step. New attocube control boxes have been purchased, which should allow better X-Y scanning, but still need to be implemented. Another problem is the diameter of the STM tip. The diameter will impact the resolution of image topography [2]. For the same

topography, the sharper tip, the smaller applied voltage is need for FESEM. Also the sharper tip is better for STM downmixing readout and reduces the electrostatic interaction force and the impact of topography. Both are reasons why developing sharper STM tips is a good way forward for this project application.

5.2. Phase Locked Loop (PLL) with STM downmixing readout

In the past decade, nanomechanical system (NEMS) resonators have shown their strong potential as high resolution sensors for ultralow mass detection application. The additional mass of an adsorbed species on the top of the NEMS or MEMS induces a shift in its resonant frequency. To measure this frequency variation, the NEMS is embedded in a phase-locked loop configuration [3]. Since the phase information is retained in STM downmixing, we can integrate our method for PLL configuration and eventual mass sensing or other application. One possible PLL setup is shown in Figure 5.1.

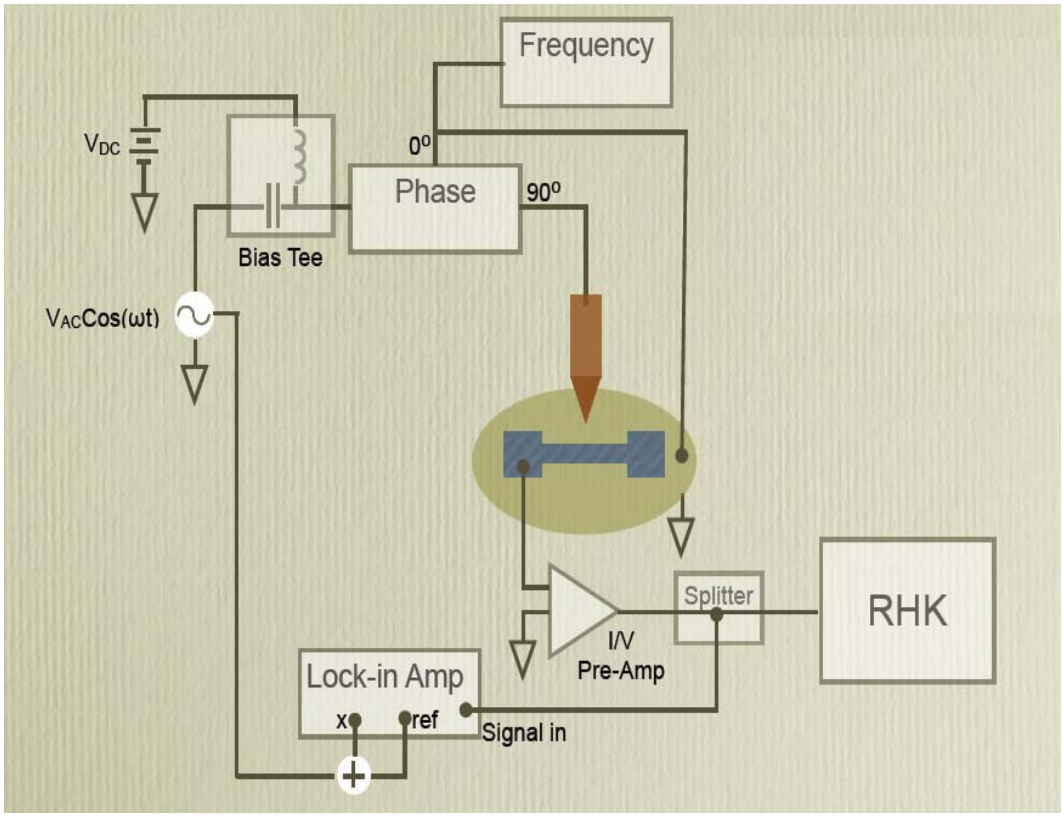

Figure 5.1 The Scheme of Phase-locked Loop with STM Downmixing Method

This STM downmixing PLL has one problem which is in relation to how the background phase changes relatively quickly in the STM downmixing method. From Figure 4.7, the X output of downmixed tunneling current has two shapes due to the different phase starting point. The reasons that the phase start point shifts are not known at this time and cannot be controlled for. A variable phase shifter will be need on the excitation pathway in order to set the phase in a desirable way such that either the X channel or the Y channel provides the null feedback control necessary in a PLL. However, since the background phase quickly changes at different frequencies, as well as for different applied force position (as in Figure 4.13), setting the phase shifter properly could prove to be different. One solution for this problem may be using the X or Y output of the downmixed tunneling current to replace the R output of the downmixed tunneling current. Some improvements are needed for current PLL scheme in order to implement the STM downmixing PLL.

5.3. All-electrical-mechanical-on-chip transduction

Currently, serious and detrimental noise source exist in the instrument which is set up to do STM downmixing readout. These noises include mechanical and electrical noises which come from the ambient of our instrument and impact the sensitivity of the measurement. It will be exciting to think about integrating the STM tip, MEMS device, and electrical parts on one chip. This will decrease the noise coming from ambient and decrease the parasitic capacitance due to wiring. It will be helpful for on-chip detection of small motions with applications ranging from accelerometers in ICT to arrayed mass sensors for biosensing in Health and Medical Technologies.

In the literature, a vertical tip and the electrode were fabricated on individual chips which were subsequently bonded together. The electrode was moved by electrostatic actuators to approach it to the tip. This sensor was made by Kenny et al [4] and was applied in an infrared detector [5]. Also a lateral tunneling sensor was developed by Sadewasser et al [6] and integrated into a

nanoelectromechanical system. A significant difficulty in the manufacture of all mechanical-electrical-on chips is the fabrication of a small gap between the sensor and the NEMS, which should be on the order of 1 nm. Current nanotechnological fabrication techniques reach a lower limit of ~ 10nm. The concept of the present tunneling sensor is based on an adjustable gap between the sensor and the NEMS. For this purpose the sensor is comprised of a tip which is movable and can be translated with respect to the motion of NEMS.

REFERENCE

1. R. D. Young, J. Ward, and F. Scire, The Topografiner: An Instrument for Measuring Surface Microtopography, *Rev. Sci. Instrum.*, 43, 999, (1972)

2. M. A. McCord and R. F. W. Pease, High resolution, low-voltage probes from a field emission source close to the target plane, *J. Vac. Sci. Technol.* B 3, 198 (1985)

3. K. L. Ekinci, Y. T. Yang, and M. L. Roukes, Ultimate limits to inertial mass sensing based upon nanoelectromechanical systems, *J. Appl. Phys.*, 95, 2682, (2004)

4. Kenny, T. W., Waltman, S. B., Reynolds, J. K., and Kaiser, W. J., Micromachined silicon tunneling sensor for motion detection, *Appl. Phys. Lett.*, 58, 100, (1991)

5. Kenny, T. W., Kaiser, W. J., Waltman, S. B., and Reynolds, J. K., Novel infrared detector based on a tunneling displacement transducer, *Appl. Phys. Lett.*, 59, 1820, (1991)

6. Sadewasser, S., Abadal, G., Boisen, A., Dohn, S., et al, Integrated tunneling sensor for nanoelectromechanical system, *Appl. Phys. Lett.*, 89, 173101, (2006)

Appendix A: Labview Program Operation

A Labview program is used to control the input signal of the STM downmixing readout circuit and readout the output of the measurement. The control panel includes three parts and is shown in Figure A.1. The first part is the set-up of instruments. Here the instruments which are used in the experiment will be chosen and activated. The second part is used to set up the parameters which control input signal and some values are required to be input, such as sweep frequency range, sweep steps, signal power and the delay between two steps. The input information is decided in this part. The third part is a monitoring part. Some output information about the STM downmixing readout, such as X output of Lock-in amplifier, phase information, the real delay between two measurement data and frequency change are shown with graphs. This is convenient for monitoring the information of STM downmixed tunneling current. Also there is a control button "STOP" which can terminate the program at anytime during the measurement. The detail Labview program is shown in Figure A.2.

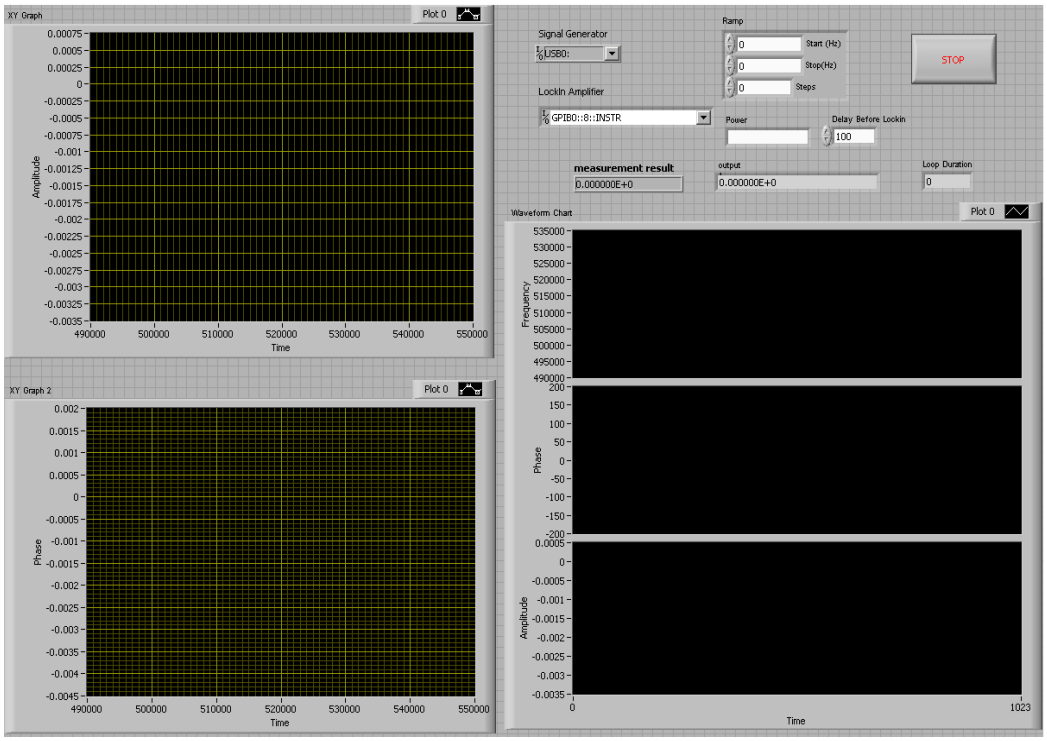

Figure A.1 STM downmixing readout circuit control panel

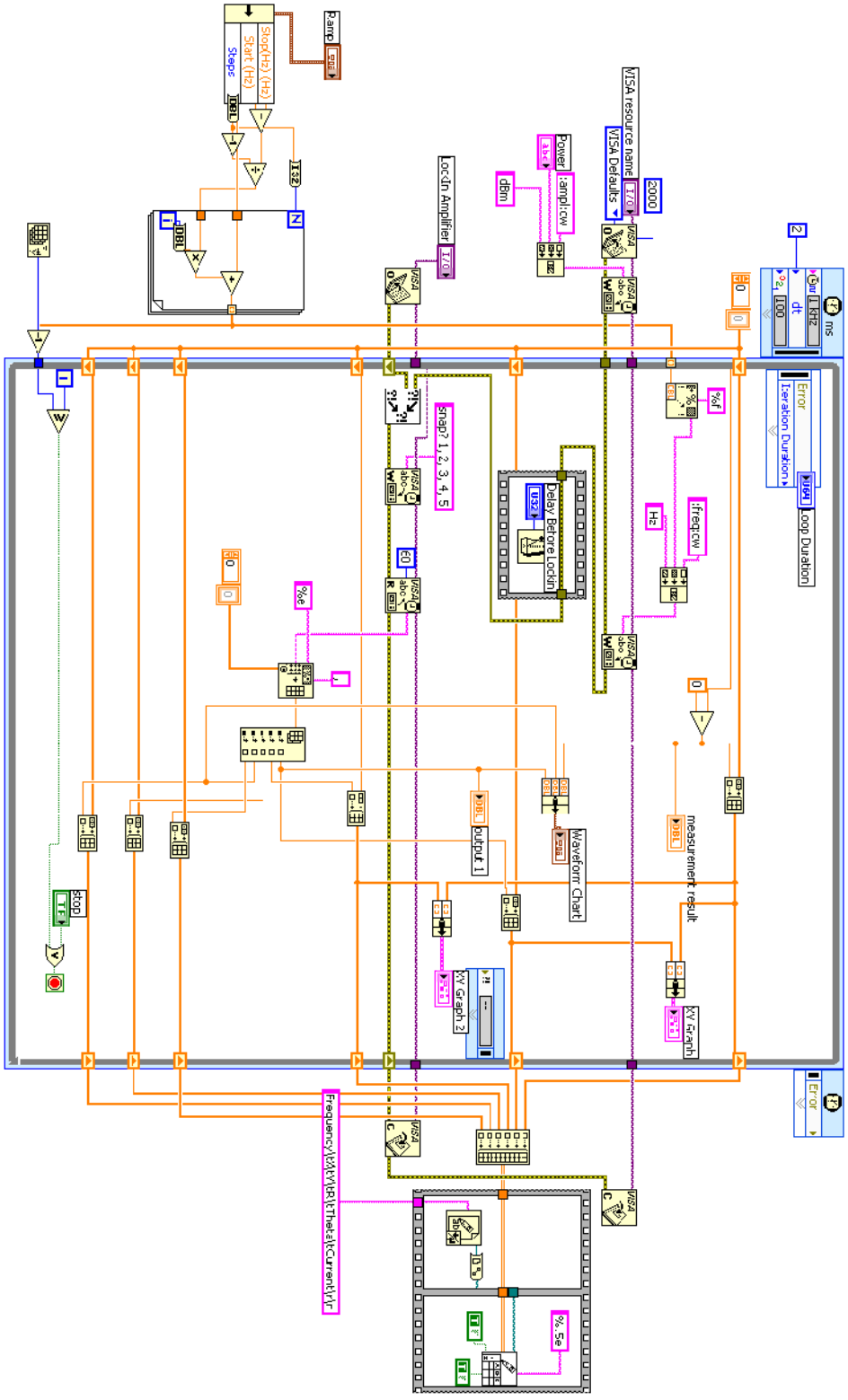

Figure A.2 STM downmixing readout Labview Program

Appendix B: STM Downmixing Analysis with Normal Mixer

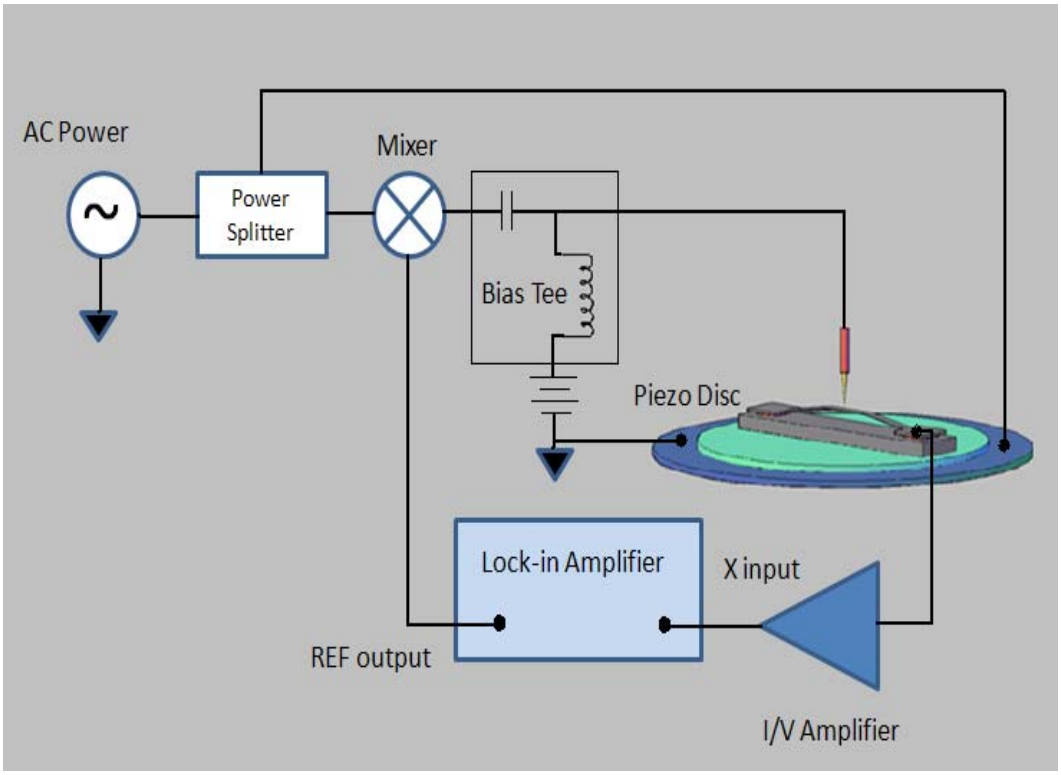

Figure B.1 Schematic of STM downmixing with normal mixer

The scheme of STM downmixing with a normal mixer is similar to the scheme of STM downmixing with the single-side band mixer. The main difference of the two circuits is the detectability of the phase information. The phase information can be monitored by the circuit with single-side band mixer, but for the circuit with normal mixer the phase information can't be monitored. That is, the normal mixer circuit is only able to read one quadrature of the mechanically related signal. The reason for this can be explained by the following derivation.

Assume the signal from the signal generator is:

$$V = V_s \sin(\omega_s t) \tag{B.1}$$

The signal from the Lock-in amplifier is:

$$V_{downmixing} = V_r \sin(\omega_r t) \tag{B.2}$$

If the phase difference is based on the phase of the Lock-in amplifier signal, the phase difference between the generator signal and the lock-in amplifier signal is set θ_1. Then the output of the mixer can be expressed as:

$$V_{output} = V_s \sin(\omega_s t + \theta_1) * V_r \sin(\omega_r t) \tag{B.3}$$

When the piezo disc actuates the MEMS, the response of MEMS has a response time. The response time cause the phase difference and we can set this phase difference θ_2. Thus the vibration of MEMS can be written as:

$$d_{MEMS} = a_m \sin(\omega_s t + \theta_1 + \theta_2) \tag{B.4}$$

For STM, when the bias voltage far less than Fermi energy of the metal, the tunneling current can be written as:

$$I \propto (V_{bias} + V(\omega)) e^{-2k(d - d_{MEMS})} \tag{B.5}$$

$$\Rightarrow I \propto (V_{bias} + V_s \sin(\omega_s t + \theta_1) * V_{ref} \sin(\omega_r t)) e^{-2k(d - d_{MEMS})}$$

Use Taylor series and triangle formulas:

$$e^x = 1 + x + \frac{1}{2!}x^2 + \frac{1}{3!}x^3 + \ldots$$

$$\sin\alpha \cos\beta = \frac{1}{2}[\sin(\alpha + \beta) + \sin(\alpha - \beta)]$$

$$\sin\alpha \sin\beta = -\frac{1}{2}[\cos(\alpha + \beta) - \cos(\alpha - \beta)]$$

The tunneling current can be rewritten as:

$$I \propto (V_{bias} - \frac{1}{2} V_s V_R \{\cos[(\omega_s + \omega_r)t + \theta_1] - \cos[(\omega_s - \omega_r)t + \theta_1]\}) e^{-2kd} [1 + 2ka_m \sin(\omega_s t + \theta_1 + \theta_2) + \ldots] \tag{B.6}$$

The high frequency parts in equation (A.6) will be blocked due to the limit of bandwidth in STM. When we omit high frequencies items and just keep reference frequency items, we can get:

$$I \propto V_{bias} e^{-2kd} - \frac{1}{2} V_s V_r e^{-2kd} k a_m [\sin(\omega_r t - \theta_2) + \sin(\omega_r t + \theta_2)] \tag{B.7}$$

Finally, using triangle identity $\sin\alpha + \sin\beta = 2\sin\frac{\alpha+\beta}{2}\cos\frac{\alpha-\beta}{2}$, the downmixed current is:

$$I \propto V_s V_r e^{-2\kappa d} k a_m \sin(\omega_r t) * \cos(\theta_2) \tag{B.8}$$

The lock-in amplifier picks the ω_r signal. However, when θ_2 is 90 degree, the signal is lost completely (that is, essentially only information about the X quadrature is available using a normal mixer).

APPENDIX C: The Beam Higher Mode Information

In Section 4.3, we use STM downmixing method to measure the first six modes of the MEMS beam. Here we display the measured results for higher mode of the MEMS beam with STM downmixing methods. Due to the complex of STM downmixing method, we cannot pinot out the detail modes which these results belong to. Here we just show these results in Figure C.1. These results are measured at the condition: DC tunneling current is 0.25nA, DC bias voltage is 0.5 V, AC bias voltage is 0.1 Vrms, and the actuating power is -11dBm. With these initial conditions, we can measure the resonance frequencies lower than 5 MHz vibration mode. For the higher frequency information, we do not get the better results due to the limit of the sensitivity of our measurement system for this measuring condition. In Figure C.1 (e) and (h), we can show the situation that the two resonance frequencies are close each other and this causes the superposition of the vibration amplitude and phase shift.

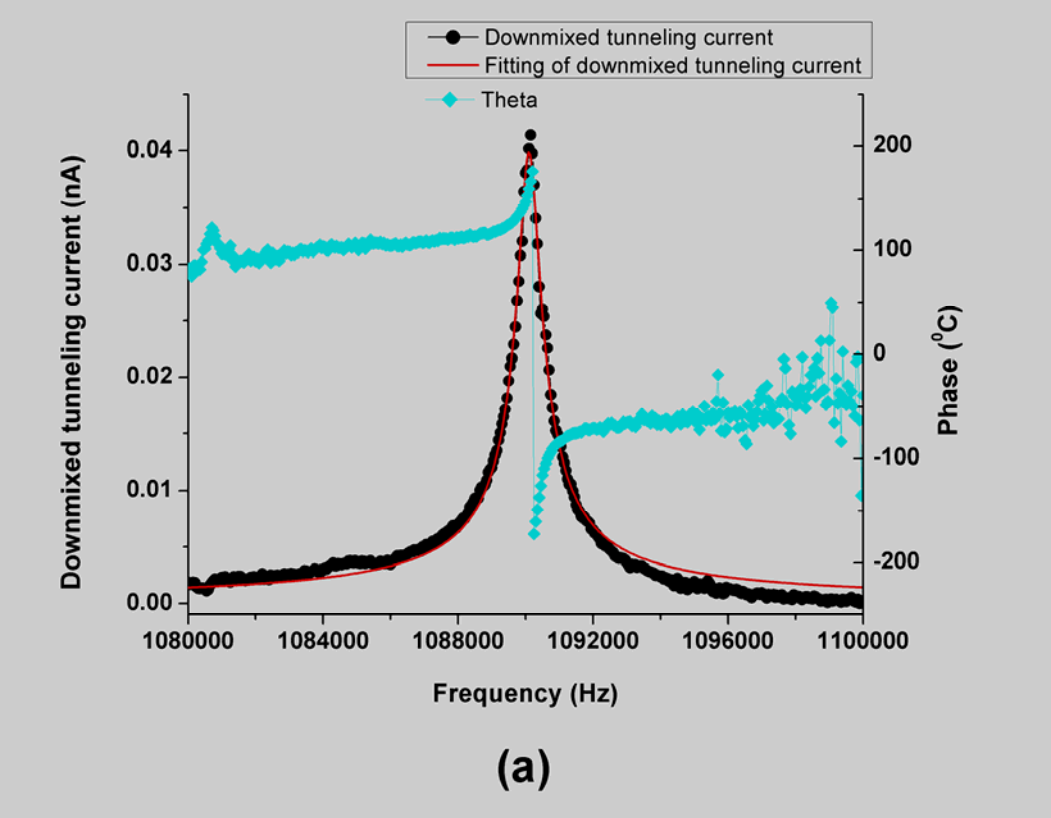

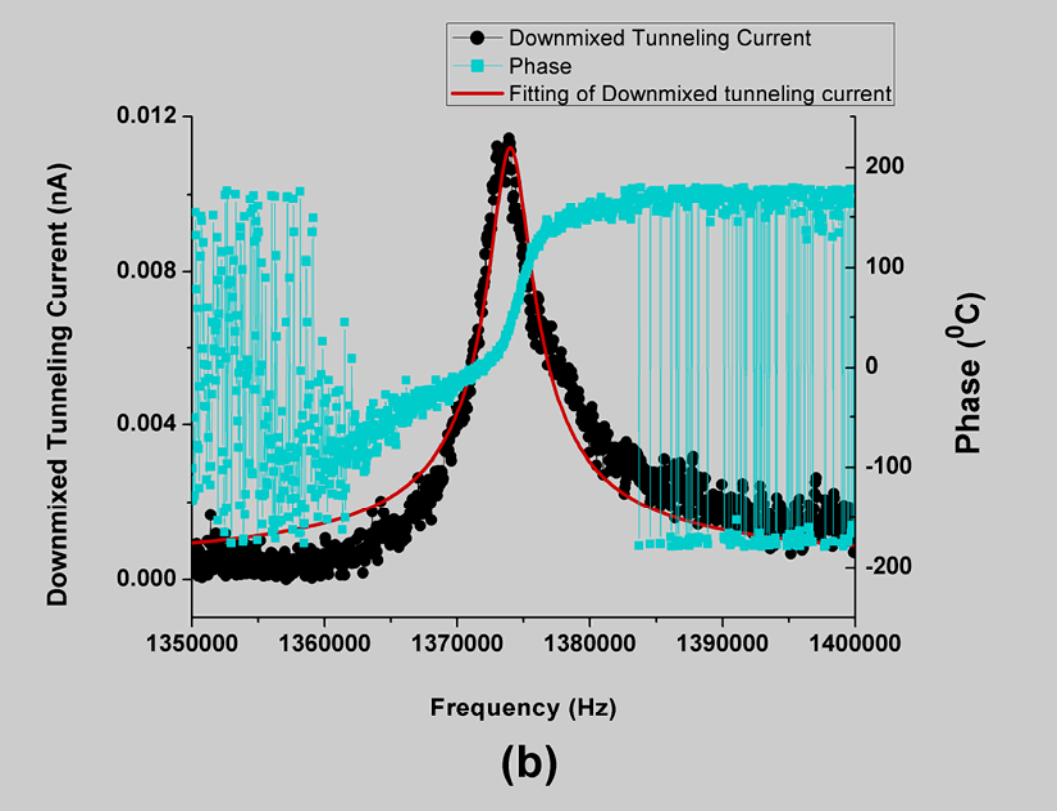
Downmixed Tunneling Current
Phase
Fitting of Downmixed tunneling current
Downmixed Tunneling Current (nA)
Phase (^{0}C)
Frequency (Hz)
0.012
0.008
0.004
0.000
200
100
0
-100
-200
1350000
1360000
1370000
1380000
1390000
1400000

(b)

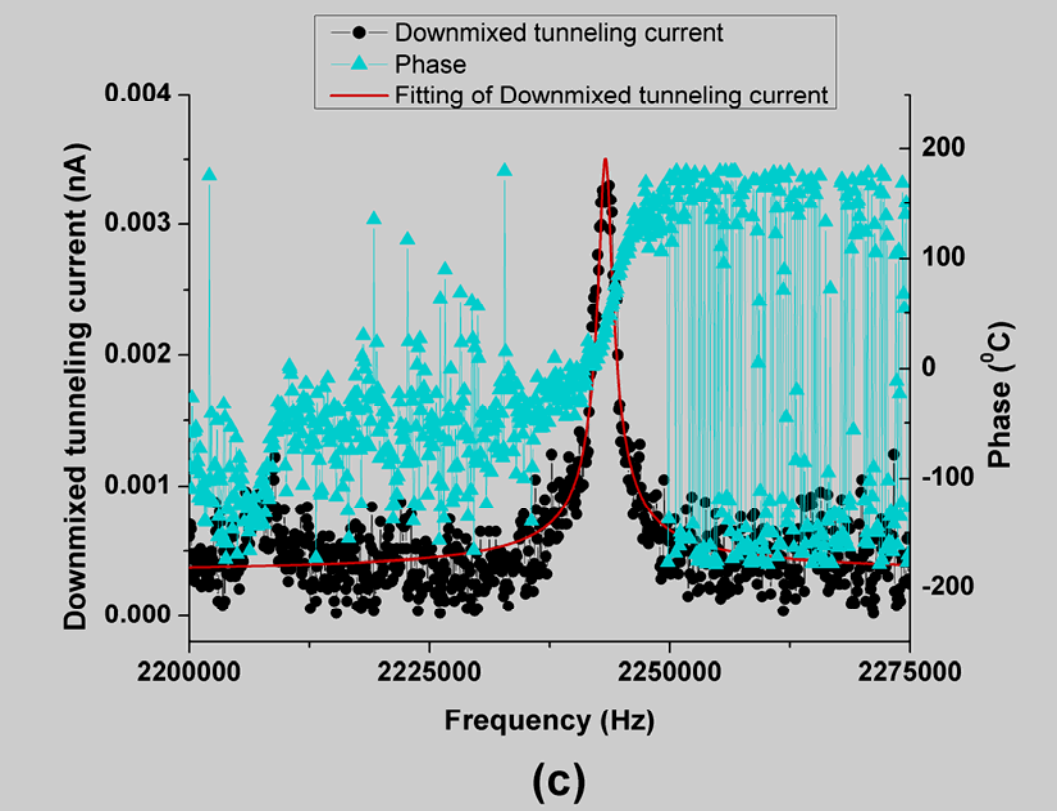
Downmixed tunneling current
Phase
Fitting of Downmixed tunneling current
Downmixed tunneling current (nA)
Phase (^{0}C)
Frequency (Hz)
0.004
0.003
0.002
0.001
0.000
200
100
0
-100
-200
2200000
2225000
2250000
2275000

(c)

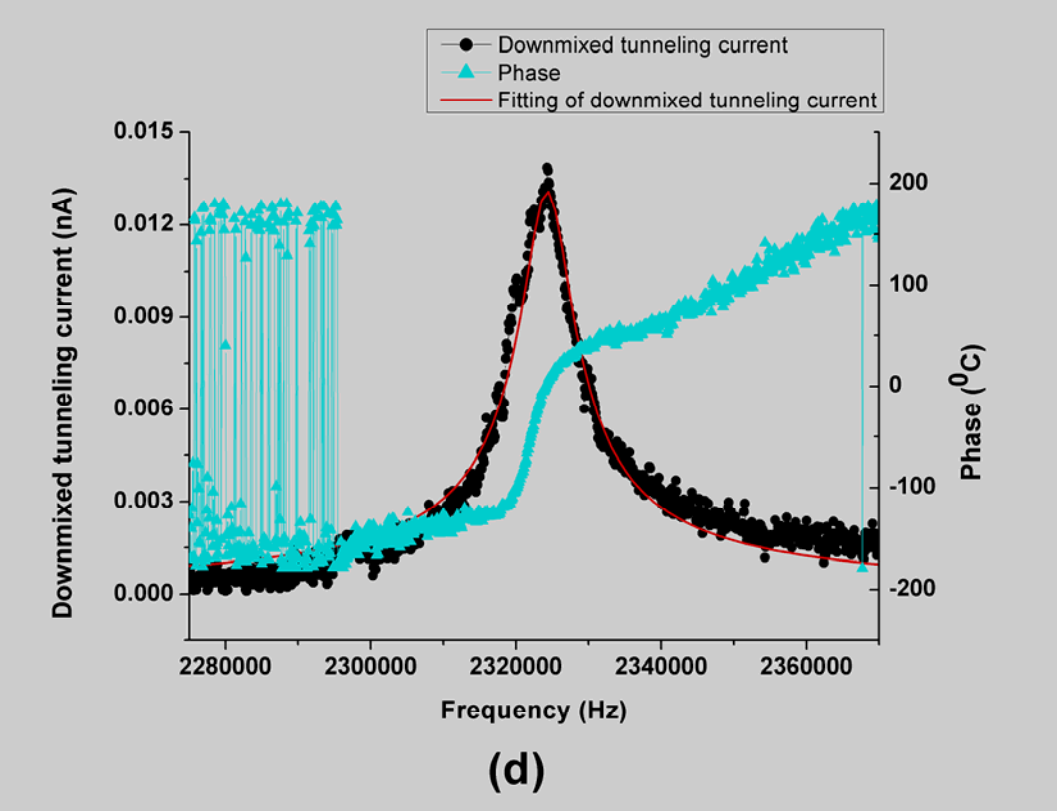
Downmixed tunneling current
Phase
Fitting of downmixed tunneling current
Downmixed tunneling current (nA)
Phase (^{0}C)
Frequency (Hz)
0.015
0.012
0.009
0.006
0.003
0.000
200
100
0
-100
-200
2280000
2300000
2320000
2340000
2360000

(d)

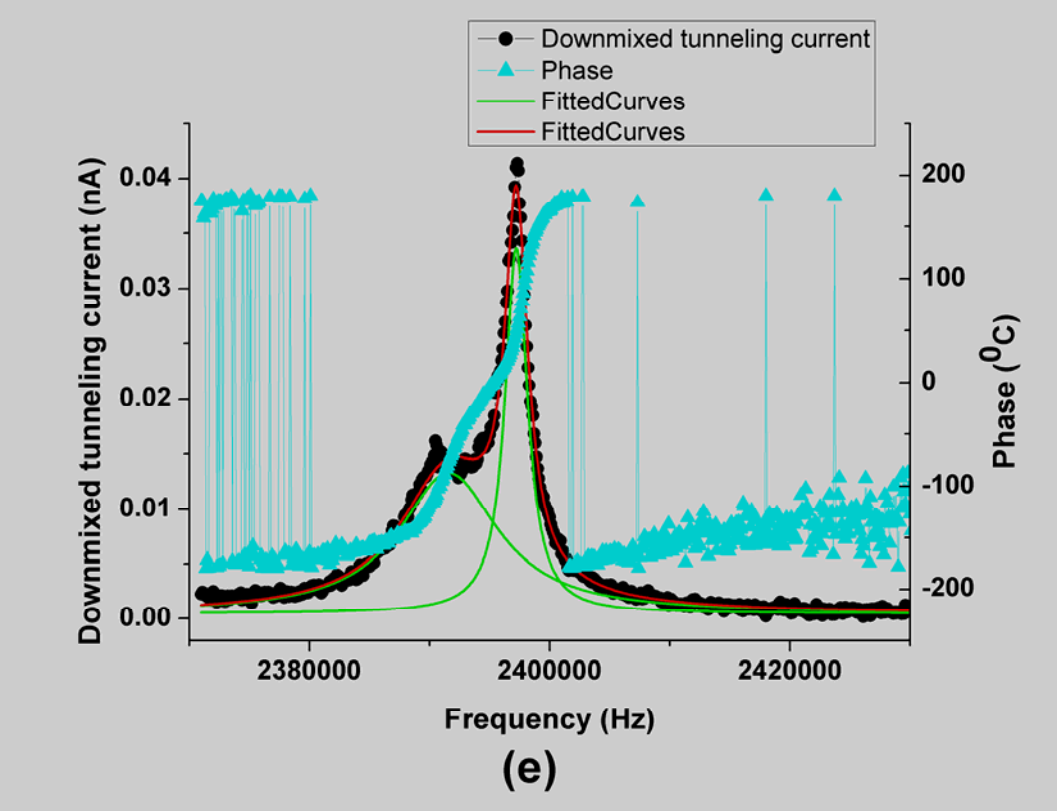
Downmixed tunneling current
Phase
FittedCurves
FittedCurves
Downmixed tunneling current (nA)
Phase (^{0}C)
Frequency (Hz)
0.04
0.03
0.02
0.01
0.00
200
100
0
-100
-200
2380000
2400000
2420000

(e)

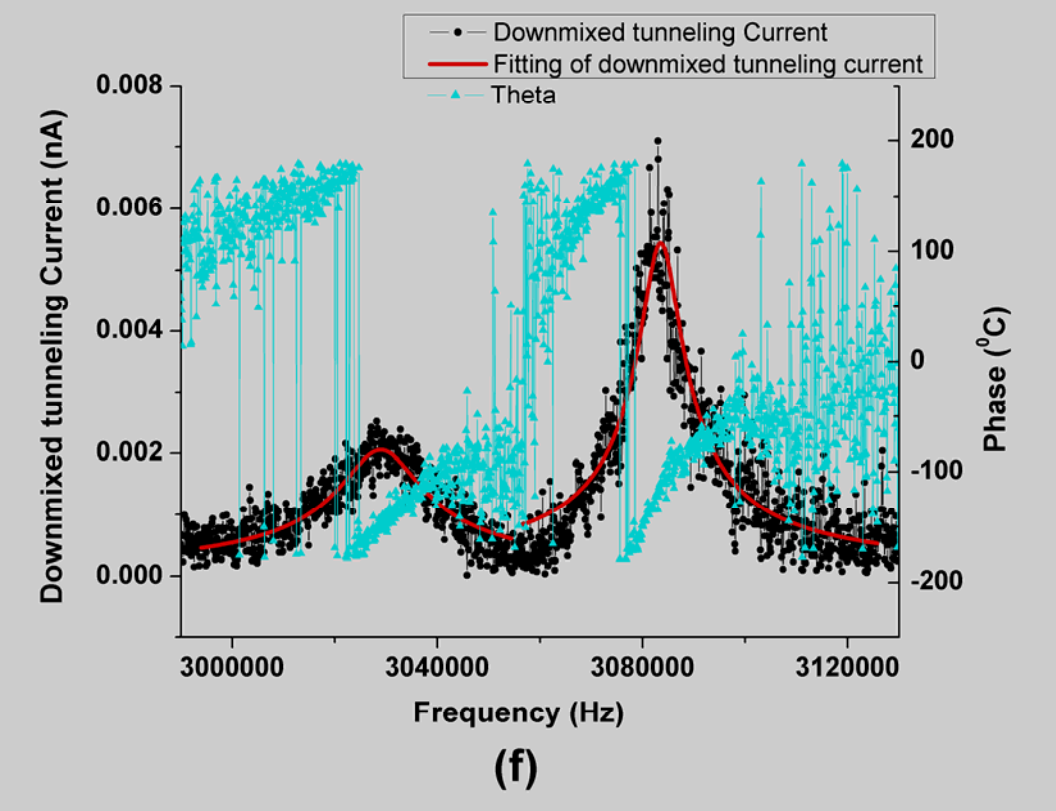
Downmixed tunneling Current
Fitting of downmixed tunneling current
Theta
Downmixed tunneling Current (nA)
0.008
0.006
0.004
0.002
0.000
200
100
0
-100
-200
Phase (°C)
3000000
3040000
3080000
3120000
Frequency (Hz)

(f)

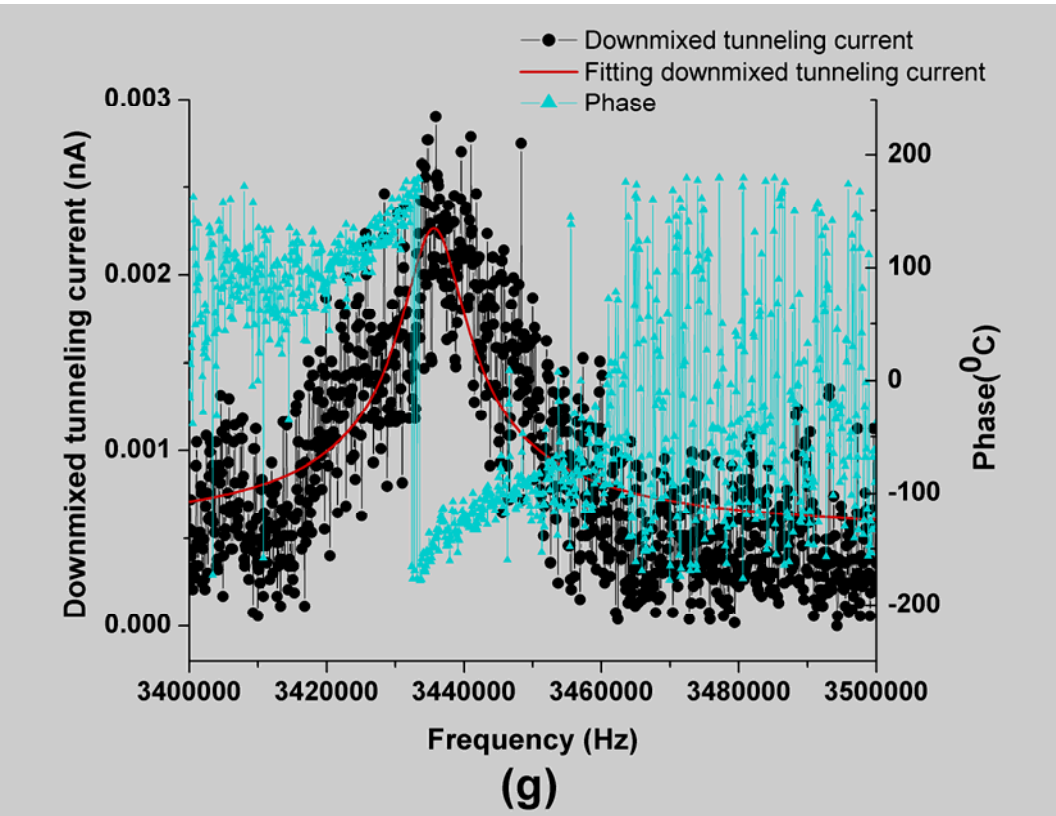
Downmixed tunneling current
Fitting downmixed tunneling current
Phase
Downmixed tunneling current (nA)
0.003
0.002
0.001
0.000
200
100
0
-100
-200
Phase(°C)
3400000
3420000
3440000
3460000
3480000
3500000
Frequency (Hz)

(g)

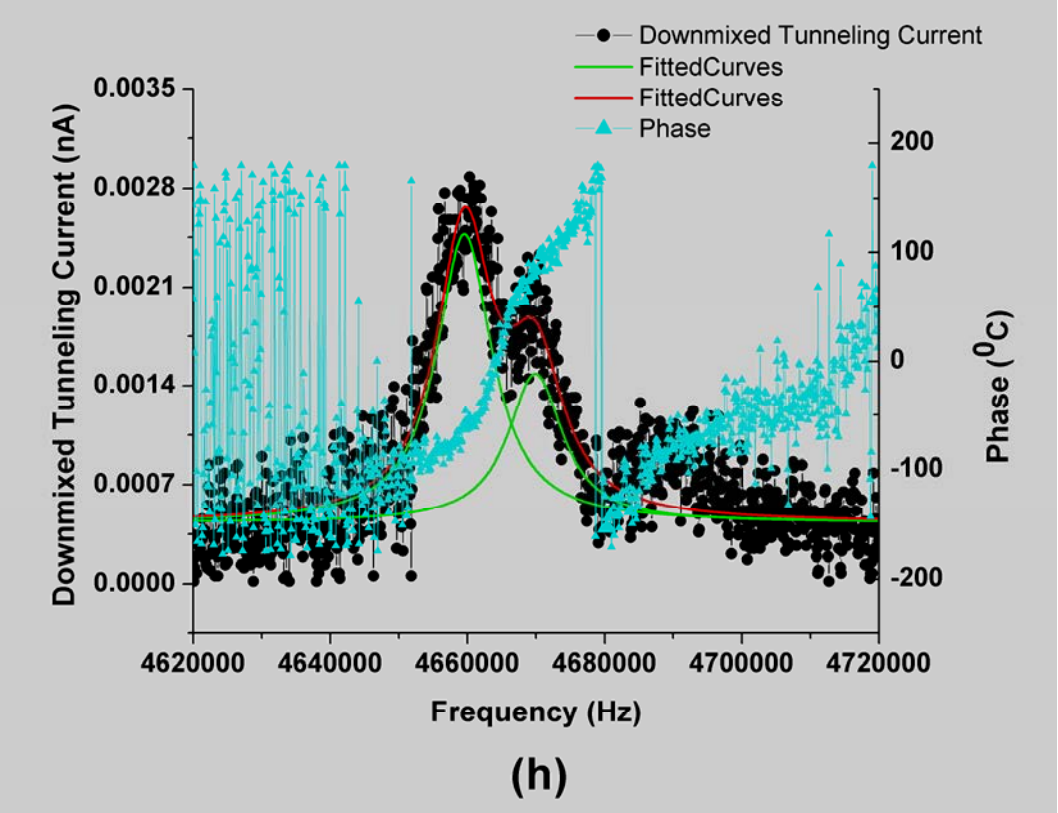

Figure C.1. The measured results for higher mode of the MEMS device vibration

These results further prove the work of the STM downmixing method. With this technique we can measure the vibration information about 5 MHz at current measuring condition which is well over the RC-bandwidth limitation of the STM system. We also can increase the displacement measurement sensitivity of our system by simply increasing DC tunneling current and decreasing the DC bias voltage which are discussed in Chapter 4.

APPENDIX D: Detail Information about the Different Point

When we use the STM downmixing method to measure the resonance frequencies for higher vibration mode of the MEMS device, a confused thing is that the resonance frequencies of the MEMS beam sometimes change with the different measuring points on the beam. There are two different results changing measuring points: one is that the resonance frequencies have a big change with the measuring points which is more than 10 percents; another one is that the resonance frequencies have a small change with the different measuring point. This is discussed in Chapter 4. Here we display the detail information for each point of Figure 4.16 in Figure D.1, in order to see the STM downmixing method and the impact of changing measuring points. The information includes the detail resonance frequencies and phase information of each point in Figure 4.16.

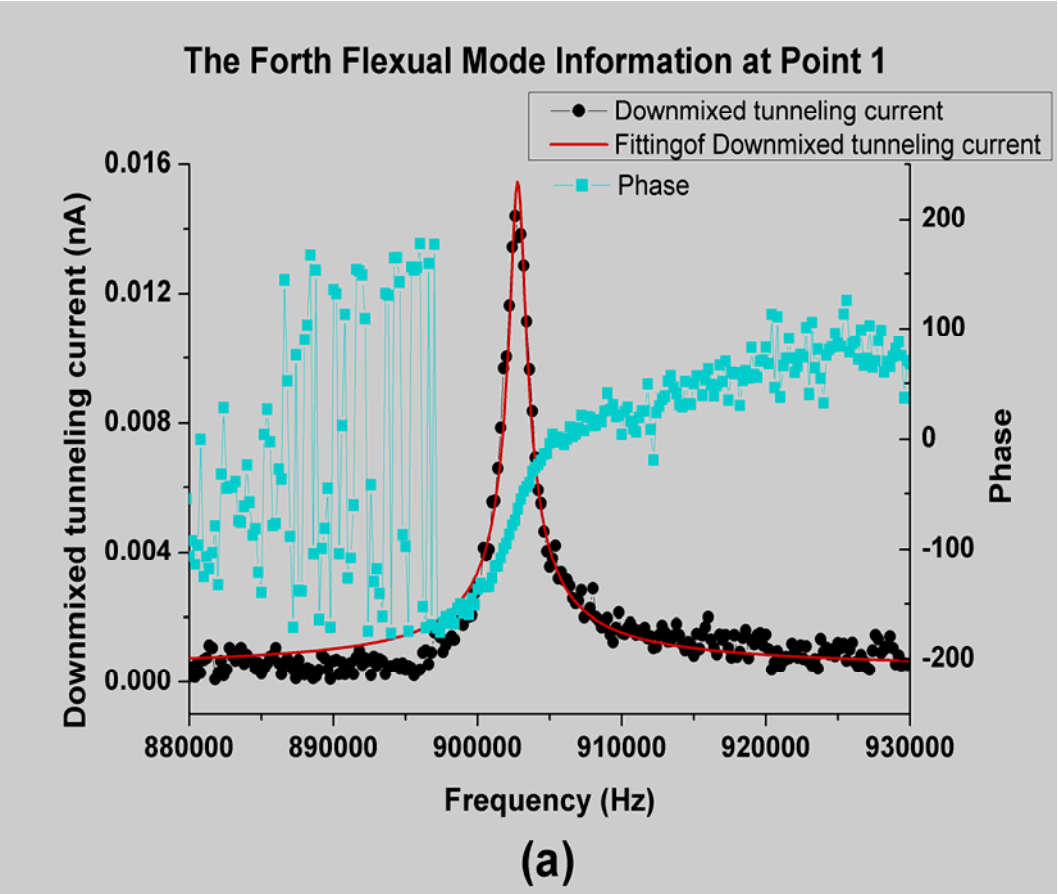

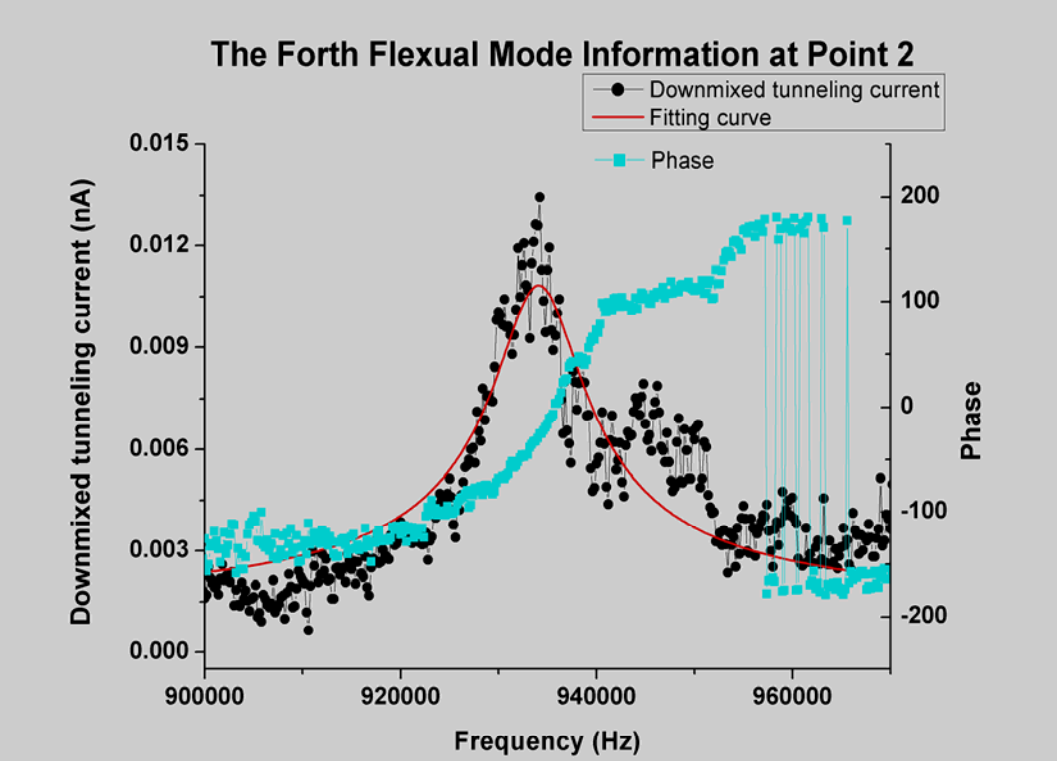
The Forth Flexual Mode Information at Point 2
Downmixed tunneling current
Fitting curve
Phase
Downmixed tunneling current (nA)
Phase
Frequency (Hz)
0.015
0.012
0.009
0.006
0.003
0.000
200
100
0
-100
-200
900000
920000
940000
960000

(b)

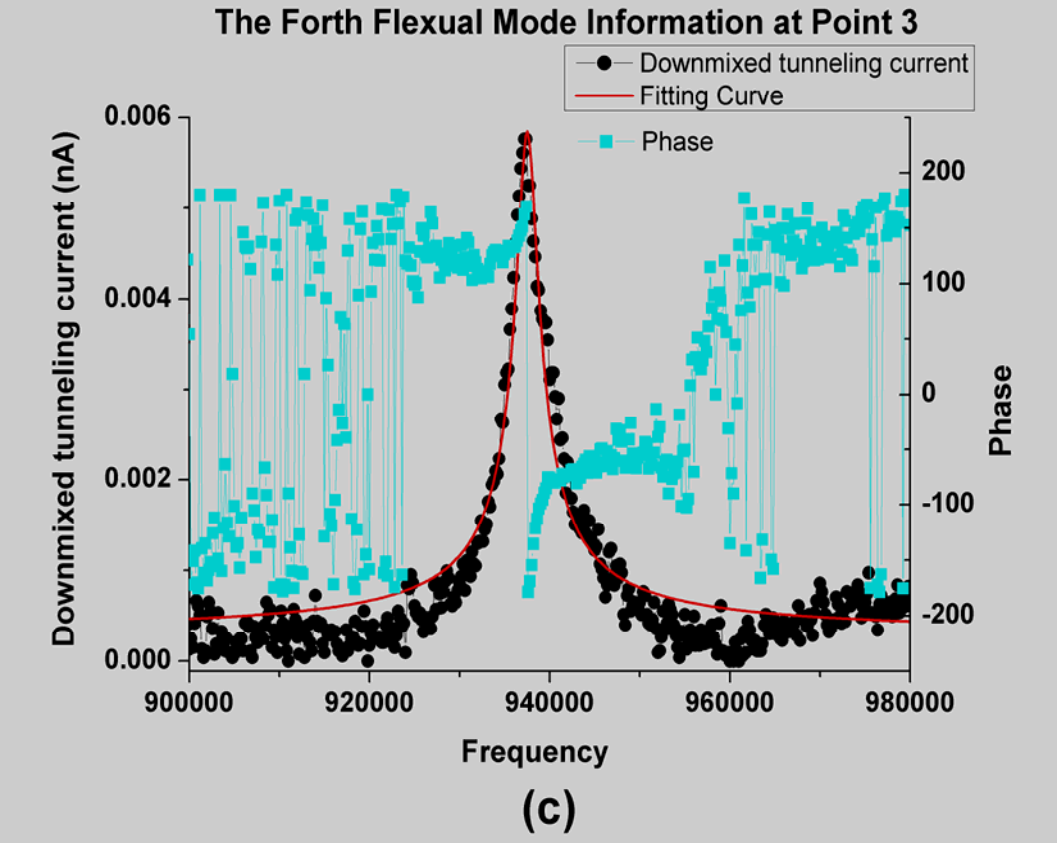
The Forth Flexual Mode Information at Point 3
Downmixed tunneling current
Fitting Curve
Phase
Downmixed tunneling current (nA)
Phase
Frequency
0.006
0.004
0.002
0.000
200
100
0
-100
-200
900000
920000
940000
960000
980000

(c)

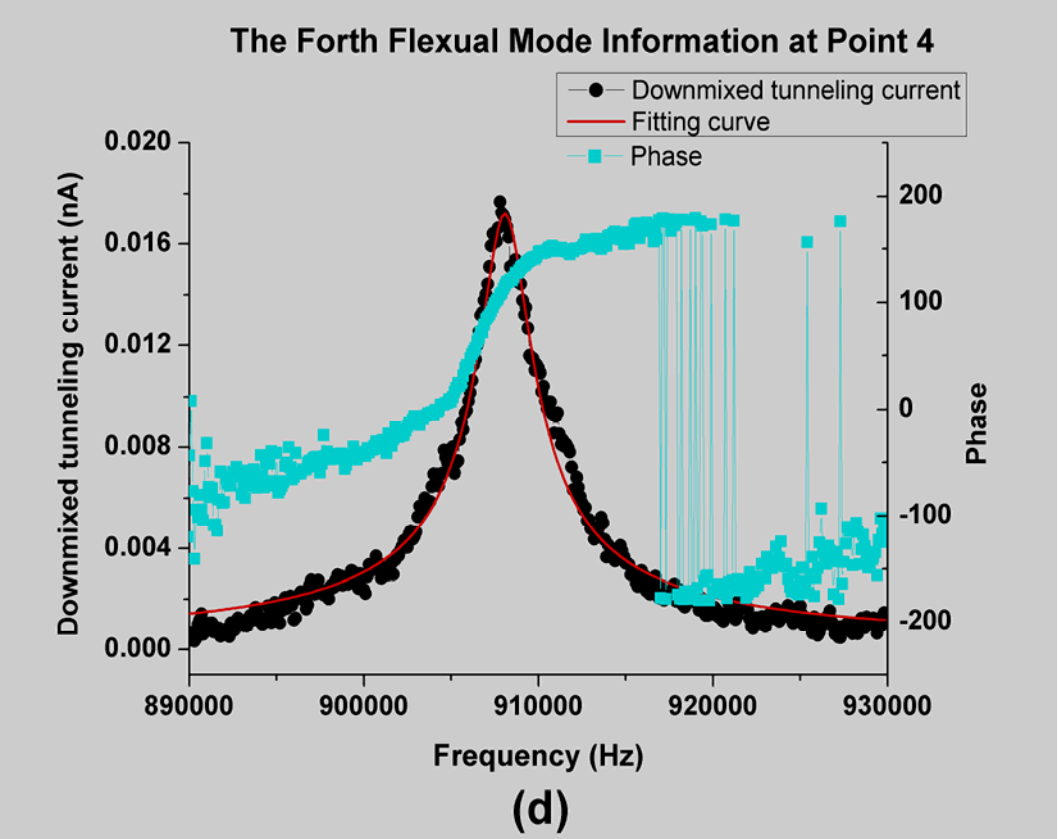
The Forth Flexual Mode Information at Point 4
Downmixed tunneling current
Fitting curve
Phase
Downmixed tunneling current (nA)
Phase
Frequency (Hz)
0.020
0.016
0.012
0.008
0.004
0.000
200
100
0
-100
-200
890000
900000
910000
920000
930000

(d)

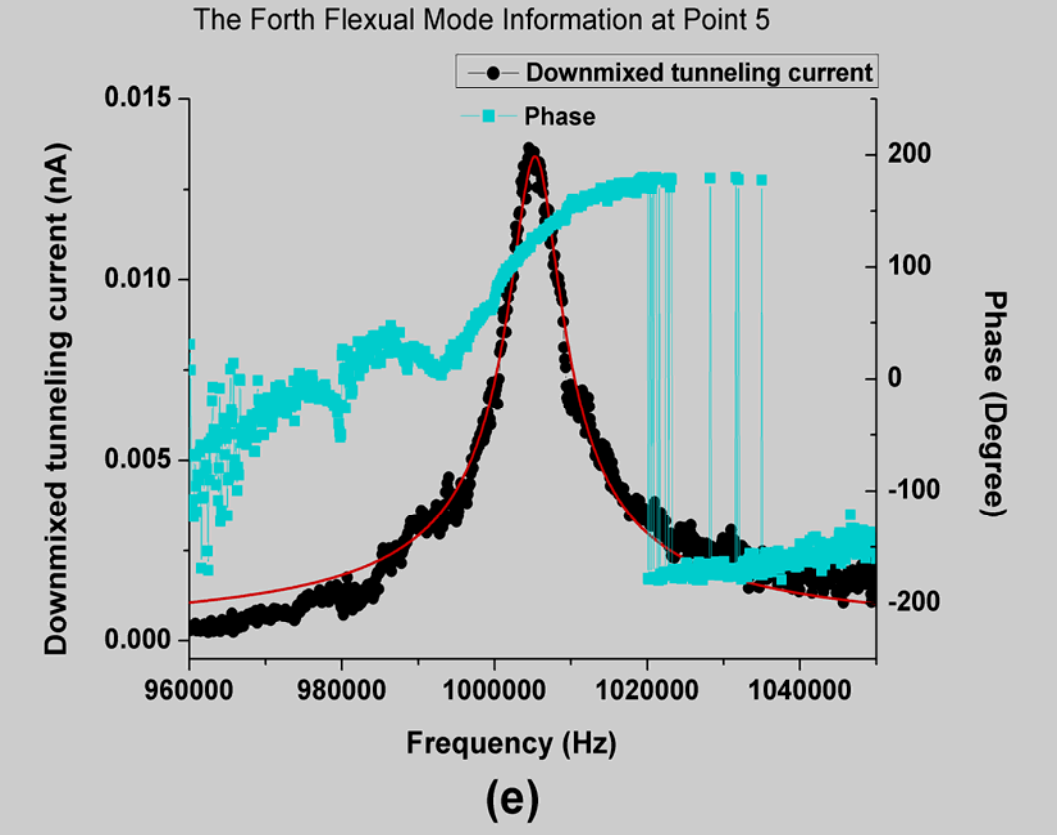
The Forth Flexual Mode Information at Point 5
Downmixed tunneling current
Phase
Downmixed tunneling current (nA)
Phase (Degree)
Frequency (Hz)
0.015
0.010
0.005
0.000
200
100
0
-100
-200
960000
980000
1000000
1020000
1040000

(e)

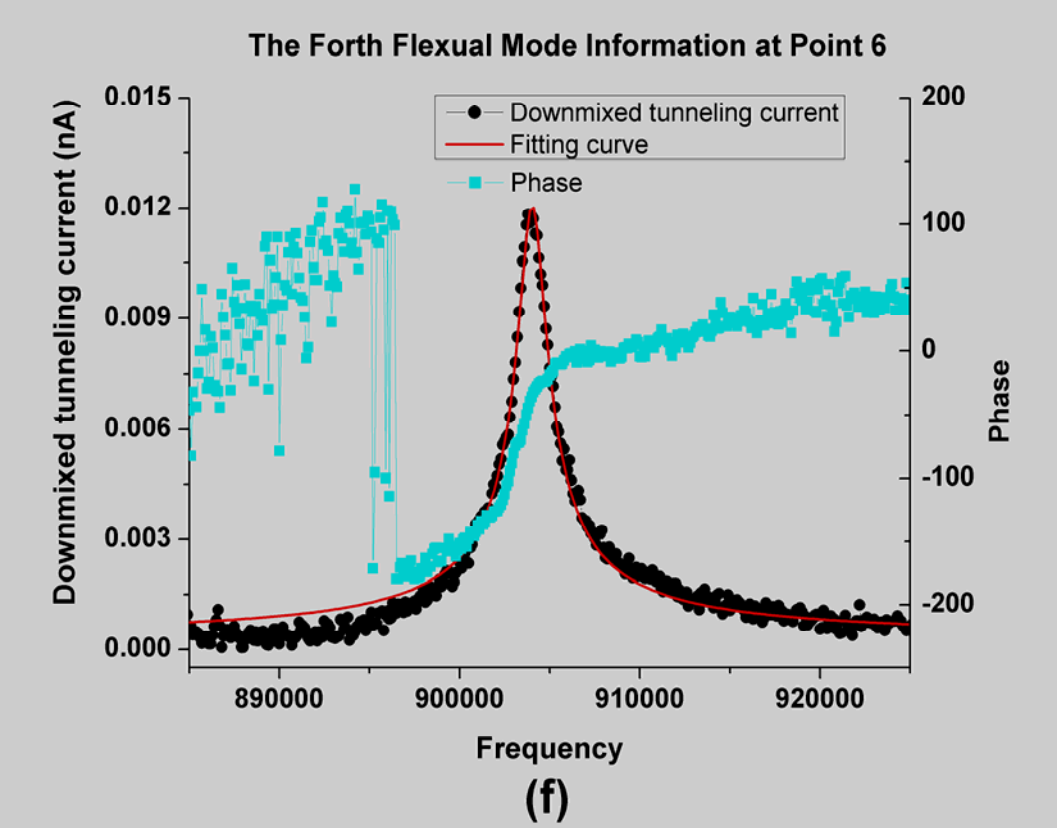
The Forth Flexual Mode Information at Point 6
Downmixed tunneling current
Fitting curve
Phase
Downmixed tunneling current (nA)
Phase
Frequency
0.015
0.012
0.009
0.006
0.003
0.000
200
100
0
-100
-200
890000
900000
910000
920000

(f)

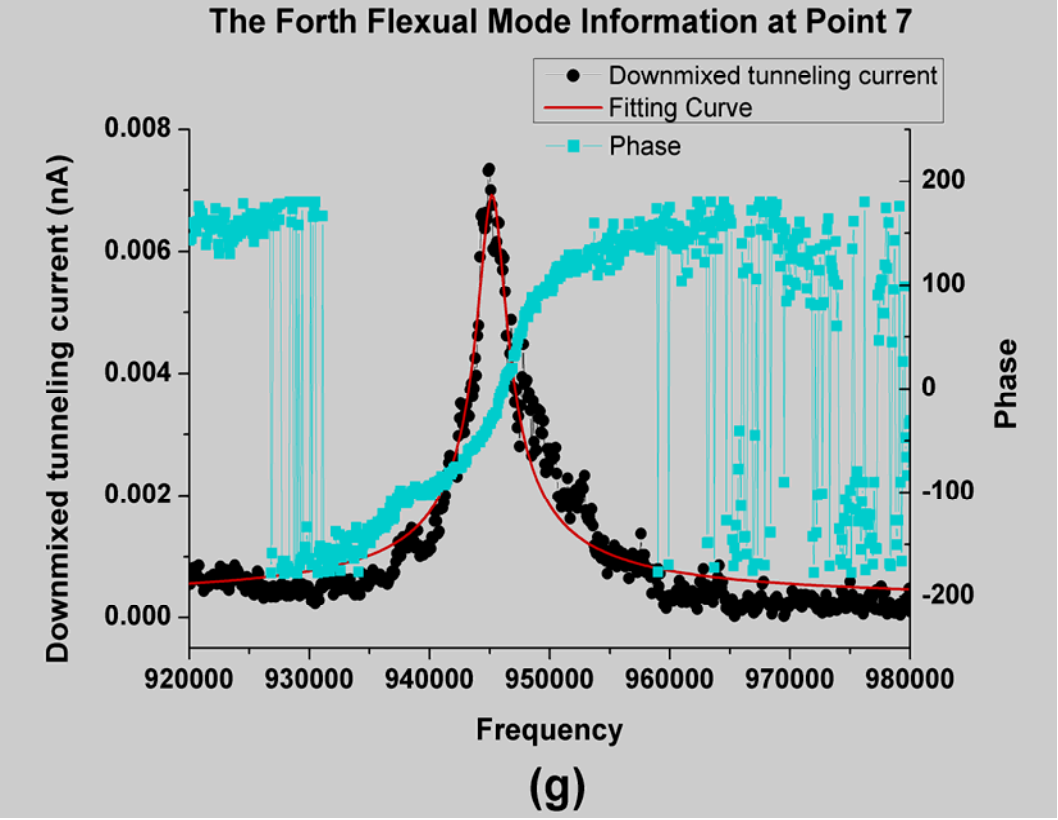
The Forth Flexual Mode Information at Point 7
Downmixed tunneling current
Fitting Curve
Phase
Downmixed tunneling current (nA)
Phase
Frequency
0.008
0.006
0.004
0.002
0.000
200
100
0
-100
-200
920000
930000
940000
950000
960000
970000
980000

(g)

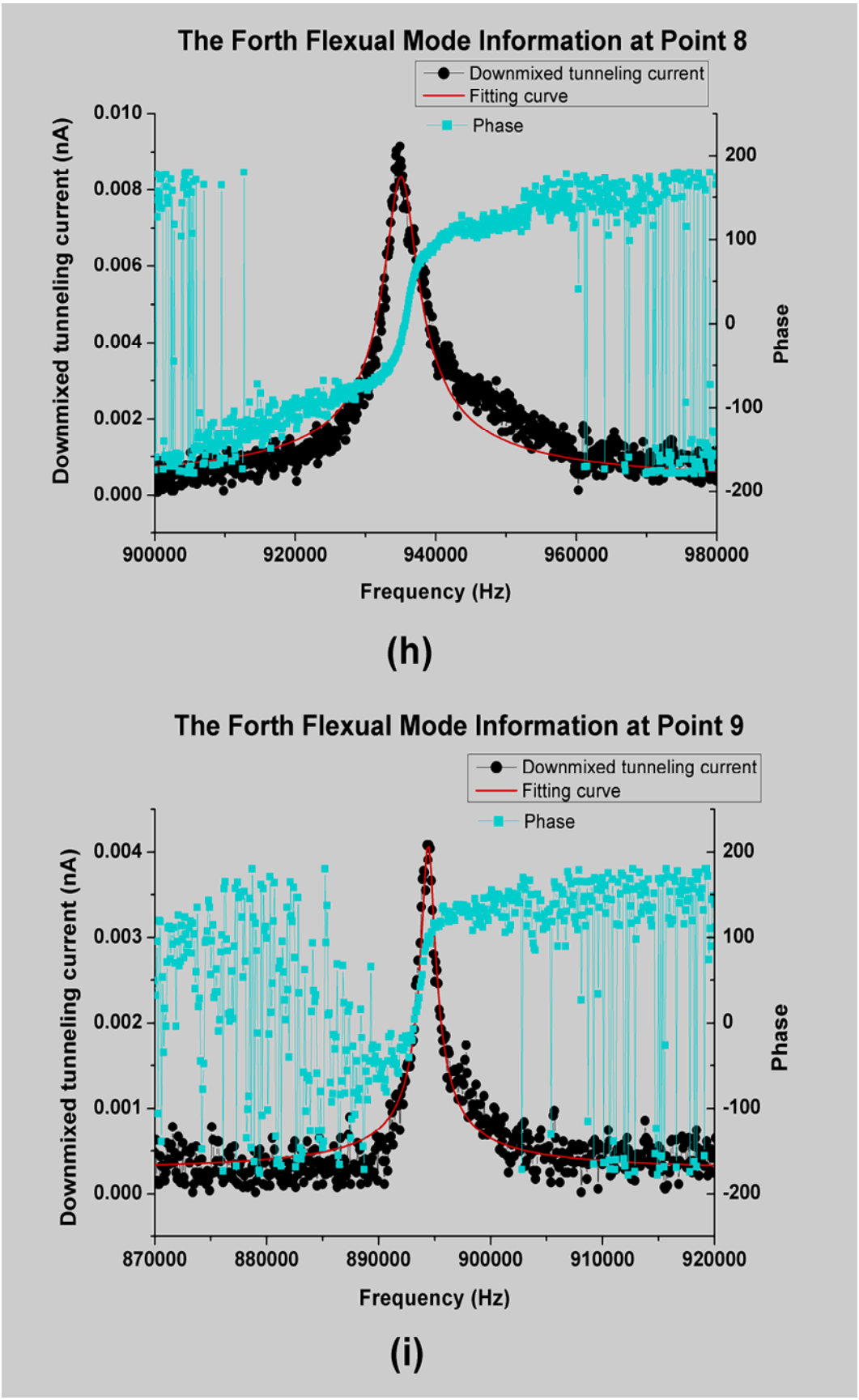
The Forth Flexual Mode Information at Point 8
Downmixed tunneling current
Fitting curve
Phase
Downmixed tunneling current (nA)
Phase
Frequency (Hz)
0.010
0.008
0.006
0.004
0.002
0.000
200
100
0
-100
-200
900000
920000
940000
960000
980000
(h)
The Forth Flexual Mode Information at Point 9
Downmixed tunneling current
Fitting curve
Phase
Downmixed tunneling current (nA)
Phase
Frequency (Hz)
0.004
0.003
0.002
0.001
0.000
200
100
0
-100
-200
870000
880000
890000
900000
910000
920000
(i)

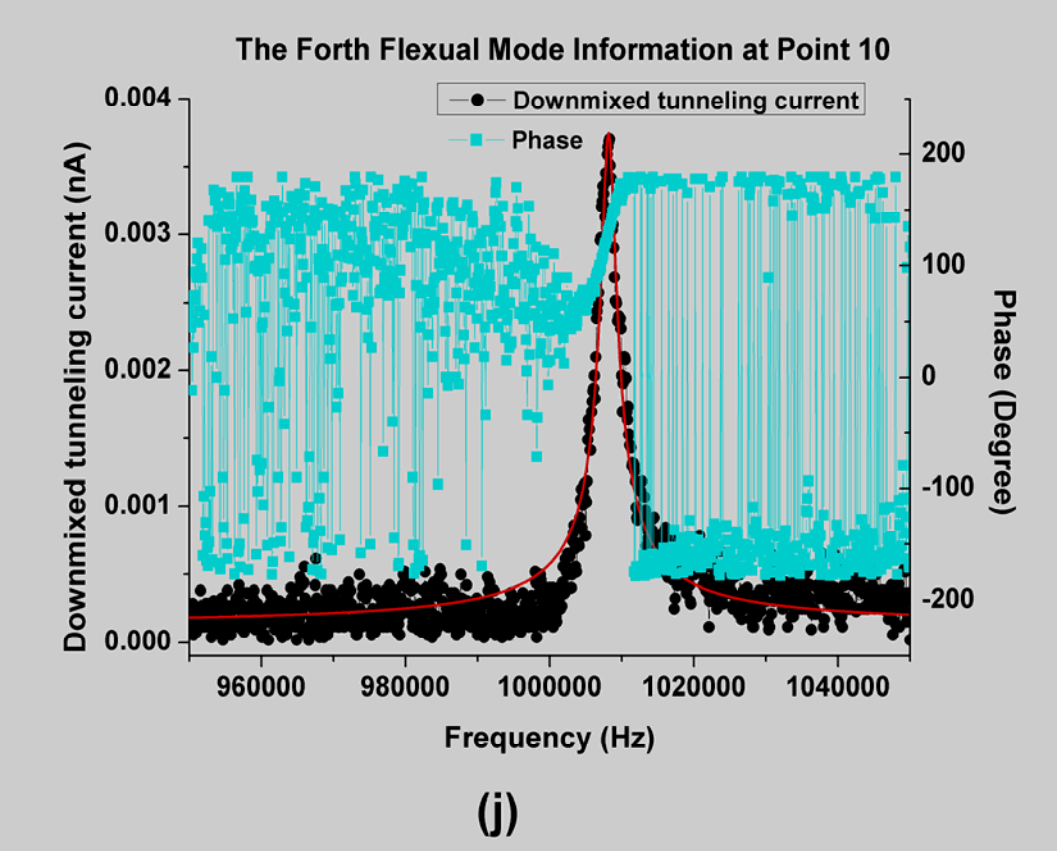

Figure D.1. The detail resonance frequency and phase shift information for different measuring points